UNIVERSITÀ DEGLI STUDI DI PADOVA

DIPARTIMENTO DI SCIENZE CHIMICHE

CORSO DI LAUREA MAGISTRALE IN

SCIENZA DEI MATERIALI

TESI DI LAUREA MAGISTRALE

Ni-based bifunctional electrocatalysts for green hydrogen production coupled with urea oxidation

RELATORE: PROF. LAURA CALVILLO

CONTRORELATORE: PROF. DENIS BADOCCO

LAUREANDO: SAMUELE ZAMBONIN

Anno accademico: 2023/2024

INDEX

ABSTRACT

The increasing population and the global warming are motivating the transition from fossil fuel-based energy supply chain to a renewable sources-based one. Hydrogen production plays a major role in technologies for renewable energy. Urea oxidation reaction (UOR) has garnered significant attention in recent years as a promising and sustainable clean-energy technology. Urea-containing wastewater poses severe threats to the environment and human health. Numerous studies hence focus on developing UOR as a viable process for simultaneously remediating wastewater and produce hydrogen. Moreover, UOR, which has a thermodynamic potential of 0.37 V (Vs reversible hydrogen electrode, RHE), shows great promise in replacing the energy-intensive oxygen evolution reaction (OER, 1.23 Vs RHE). Since UOR entails a complex intermediate adsorption/desorption process, many studies are devoted to designing cost-effective and efficient catalysts. Notably, Nickel-based materials have demonstrated significant potential for the UOR process. In this thesis work, nickel hydroxide has been chosen as catalyst with the objective of preparing it from Ni-containing wastewater in the future in collaboration with Circular Materials s.r.l. In this thesis, however, the materials have been synthetized in the laboratory to better control their properties and be able to extract more consistent conclusions. Manganese (1.55) and molybdenum (2.16) have been selected as doping elements, considering their different electronegativity respect to nickel (1.91), and their effect on the UOR performance has been studied. Manganese is less expensive and more ecofriendly than the commonly used cobalt (1.88). Iron (1.83) is even cheaper than Mn but it was not selected since it is known that improves the OER but not the UOR. Molybdenum was selected for its high electronegativity since it was found that, in metal fluoride, the strong electronegativity of F makes the metal in the electron deficiency state, which can promote the high valence state of metal species and, therefore, promote urea oxidation. This materials were characterized with techniques such as, transmission electron microscopy (TEM), X-ray diffraction (XRD), X-ray absorption (XAS) and X-ray photoelectron spectroscopy (XPS). They have been tested as UOR catalysts in alkaline solution. Nickel phosphide-based catalysts have been also obtained from the phosphorization of the nickel-based hydroxide materials. The nickel phosphide-based catalysts have been characterized using the same techniques previously mentioned. These materials have been then tested as HER and UOR catalysts. In general for all the materials, the presence of the second metal increased the activity. In UOR and OER measurements, Nickel phosphide-based samples reached higher current densities than the corresponding nickel hydroxide-based materials. For the nickel-hydroxide based-materials, the samples containing molybdenum showed a better performance during UOR than the ones containing manganese. While for the nickel-phosphide based materials it was the opposite. The foreign element did not have any effects on the activity towards the HER for the NiP-based samples. More negative on set values and low current densities were obtained.

CHAPTER 1

INTRODUCTION

1.1 – current situation of energy economy

The global energy landscape is at a critical juncture, marked by a confluence of challenges that demand urgent attention and decisive action. As societies navigate the complexities of population growth, urbanization, and economic development, the sustainability of current energy systems comes under scrutiny. Perhaps the most pressing challenge facing the energy economy is the threat of climate change[1]. The relentless combustion of fossil fuels releases greenhouse gases into the atmosphere, leading to rising temperatures, extreme weather events, and disruptions to ecosystems. The need to mitigate climate change requires a rapid transition away from carbon-intensive energy sources towards low-carbon alternatives, alongside efforts to enhance energy efficiency and conservation measures[2,3]. As the world's population continues to expand, surpassing 8 billion and projected to reach nearly 10 billion by 2060, the energy demand increase and the strain on finite fossil fuel resources intensifies. Figure 1.1 reports that the use of fossil fuels did not decrease even if the production of renewable energy such as solar, wind and hydropower increased in the last years.[4]

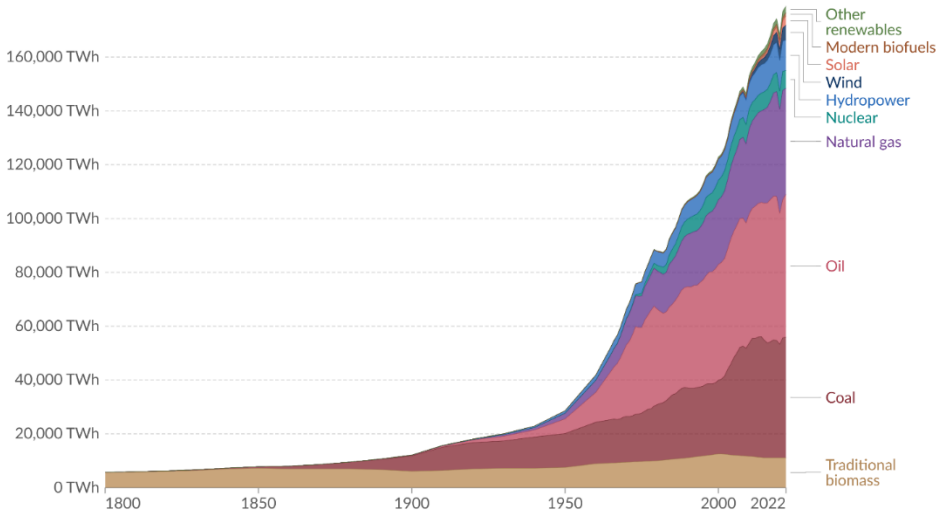

Figure 1.1 global primary energy consumption, energy consumption is measured in terawatts per hour. Reprinted from [1].

Figure 1.2 shows how the CO_2 production from fossil fuels actually increased even after the introduction of renewable energy in the energy economy[1]. Land use change is a process by which human activities transform the natural landscape, these emissions result from human activities that alter land cover, such as deforestation, afforestation, and changes in land management practices. From figure 1.3 is possible to understand from which sectors come all the greenhouse gas emissions responsible for global warming, the two main sectors are “Electricity and heat” and “transport”[1]. The demand from both this sectors is rapidly increasing due to the population growth, if the reduction of harmful gasses from the first sector can be achieved by increasing the use of renewable source of energy[5]. For the transportation sector the solution is

to replace standard fuel such as gasoline and diesel with more green alternatives such as biofuels (solar fuel) and hydrogen[6].

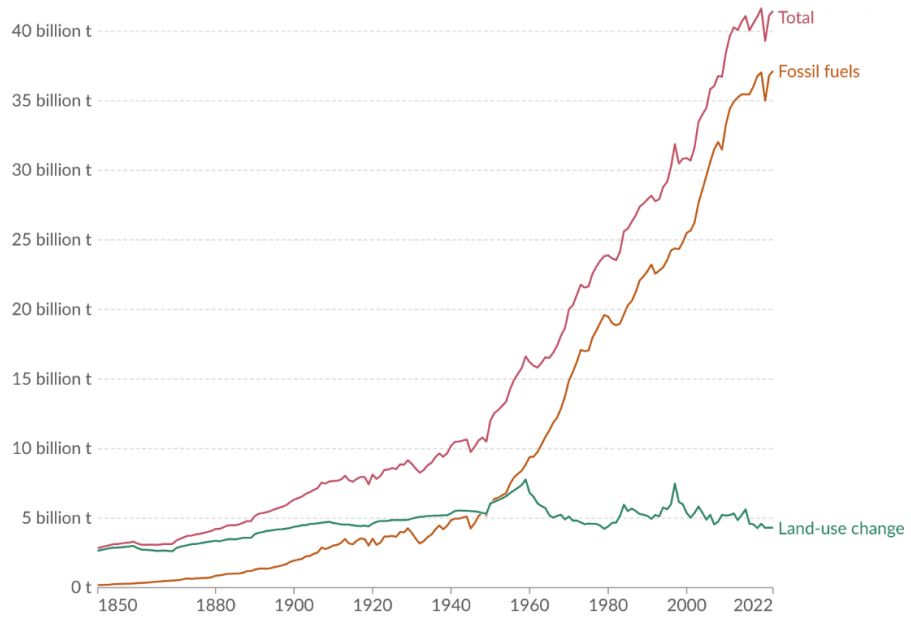

Figure 1.2 CO_2 production (in tons) over the last years from fossil fuels use and land-use change. reprinted from [1]

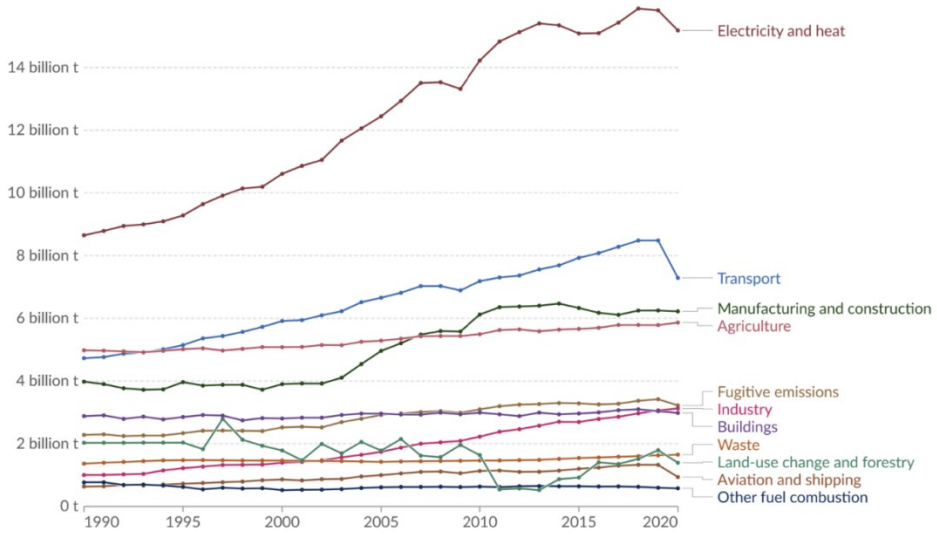

Figure 1.3 greenhouse gas emissions (measured in tons of carbon dioxide-equivalents[a]) over the last 30 years from different fields. Reprinted from [1].

Addressing the dual challenges of high energy demand and increasing CO_2 production requires a comprehensive strategy that integrates technological innovation, policy intervention, and behavioral change. Accelerating the transition to renewable energy sources such as solar, wind, hydroelectric, and geothermal power is crucial for reducing CO_2 emissions associated with electricity generation[7]. However, one of the primary challenges impeding the widespread adoption of renewables is their inherent intermittency[5]. Unlike conventional fossil fuel-based power generation, which provides a consistent and controllable energy output, renewable energy generation fluctuates with weather patterns, time of day, and other factors. Energy storage technologies such as batteries play a crucial role in mitigating intermittence by storing excess renewable energy during periods of high generation and releasing it when needed[8]. Implementing batteries to store excess renewable energy presents several challenges, making it costly and difficult to achieve widespread

adoption. A solution to this problem could be the use of hydrogen as a clean energy carrier, it holds potential for both storing excess renewable energy and serving as a fuel[9]. Hydrogen storage systems can be more easily scaled up compared to batteries, while battery storage systems may face constraints related to the availability of raw materials and manufacturing capacity, hydrogen storage can be expanded by adding additional tanks or infrastructure[10,11]. This scalability makes hydrogen a flexible option for accommodating large amount of energy storage systems as renewable energies become more prevalent. One of the most promising applications of hydrogen is in transportation, particularly in fuel cell vehicles, in this device hydrogen is combined with oxygen from the air to produce electricity, which then powers an electric motor to propel the vehicle, the only byproduct of this process is water vapor[12–15]. While hydrogen offers many advantages it also comes with several drawbacks, mainly due to the high cost to produce green hydrogen, energy losses and safety issues[16,17]. Hydrogen, the most abundant element in the universe, has long been hailed as a potential game-changer in addressing the world's energy challenges. As humanity struggles with the need to transition to sustainable energy sources to mitigate climate change and reduce reliance on finite fossil fuels, hydrogen emerges as a promising solution. Its versatility, abundance, and clean-burning properties offer a multitude of opportunities to revolutionize various sectors and reshape the global energy landscape[12,14].

1.2 – Hydrogen production

Unlocking the full potential of hydrogen as a sustainable energy source requires addressing key challenges associated with its production, particularly the need to minimize carbon dioxide emissions and enhance efficiency[18]. There are several methods for producing hydrogen, each with its own advantages, limitations, and environmental considerations. In figure 1.5 are shown different categories of hydrogen (divided by color).

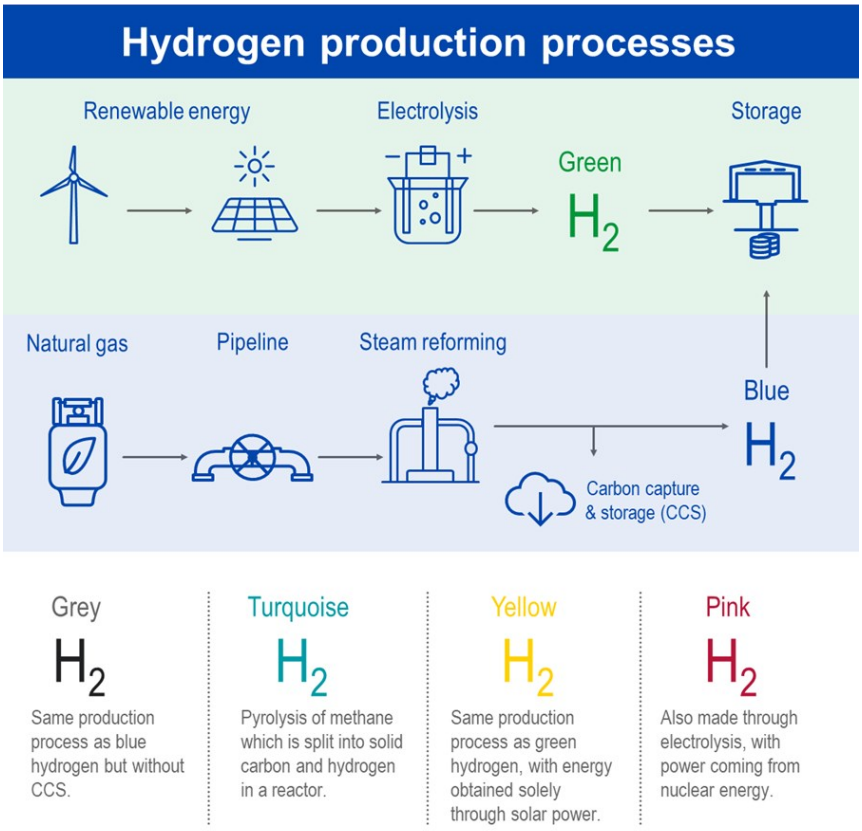

Figure 1.2 categories of hydrogen produced in different ways, divided by color. Reprinted from [32].

1.2.1 steam methane reforming (SMR)

SMR is currently the most widely used method for industrial-scale hydrogen production, accounting for the majority of global hydrogen output[19]. In this process, natural gas (primarily methane) reacts with steam at high temperatures (700-1100°C) in the presence of a catalyst to produce hydrogen and carbon monoxide.

$$CH_4 + H_2O \rightarrow CO + 3H_2$$

After steam reforming, the produced CO gas undergoes a water-gas shift reaction to further increase the hydrogen yield and reduce the concentration of CO, a byproduct of steam reforming. This reaction occurs at lower temperatures (around 200-400°C)[19] :

$$CO(g) + H_2O(g) \rightleftharpoons CO_2(g) + H_2(g)$$

This reaction converts CO into CO_2 while producing additional hydrogen gas.

The product gas from the water-gas shift reaction contains carbon dioxide (CO_2), which must be separated to obtain pure hydrogen. Various methods, such as pressure swing adsorption (PSA)[20] or membrane separation[21], are employed for CO_2 removal. The remaining gas mixture, primarily consisting of hydrogen, is further purified to remove any remaining impurities such as CO, CO_2, and methane. This purification step ensures the production of high-purity hydrogen suitable for various applications. SMR is highly efficient and cost-effective for large-scale hydrogen production, primarily due to the abundance of natural gas feedstock and the well-established infrastructure for natural gas processing and distribution[22]. However, SMR is associated with significant carbon dioxide emissions due to the use of fossil fuels as feedstocks, making SMR a significant source of greenhouse gas emissions unless coupled with carbon capture and storage (CCS) technology[23].

1.2.2 Water splitting

Water splitting is a process that enables the production of hydrogen by direct water decomposition in its elements[24]. The energy required to cleave H—O—H bonds can be supplied by different power sources: electrical (current)[25], thermal (heat)[26], or light[27]. Electrochemical water splitting is driven by passing the electrical current through the water, where conversion of the electrical energy to chemical energy takes place at the electrode solution interface through charge transfer reactions in a device called electrolyser[28] (figure 1.6). Water splitting is processed via two half-cell reaction; water reduction (cathode) and water oxidation (anode).

Hydrogen evolution reaction (HER), the reduction of protons at the cathode:

$$2H^+ + 2e^- \rightarrow H_2$$

And oxygen evolution reaction (OER):

$$2H_2O \rightarrow O_2 + 4H^+ + 4e^-$$

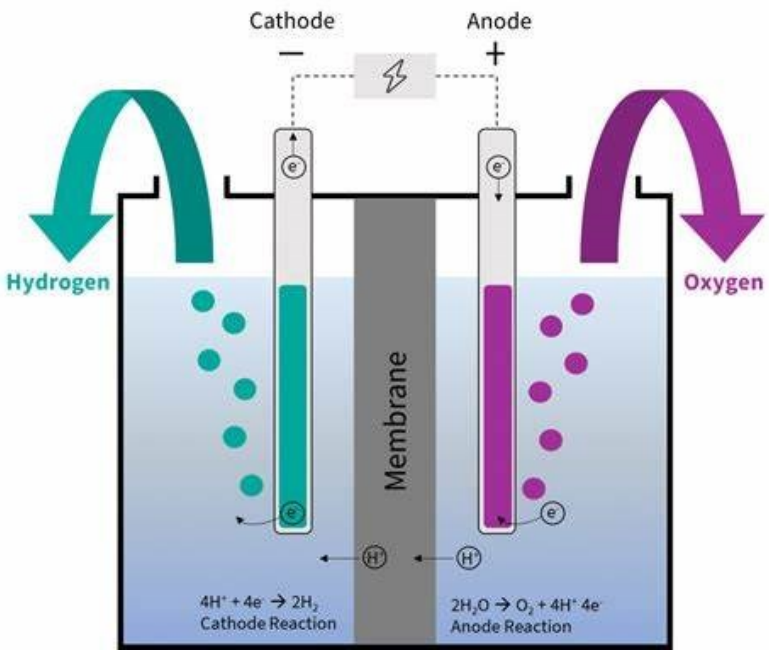

Figure 1.6 electrolyser scheme reprinted from [47].

World widely, hydrogen produced by this method accounts for about 4%[29], this is due to the fact that hydrogen can be produced less expensively from fossil fuels. The high costs of hydrogen produced through water splitting is mainly due to the fact that the decomposition of water into hydrogen and oxygen at standard temperature and pressure is not favorable in thermodynamic terms[25]. Furthermore water is very stable and a bad conductor, to increase its conductivity electrolytes are used, some examples are: sulfuric acid, potassium hydroxide and potassium phosphate buffer making the medium acidic, basic and neutral, this influences the ionic species present in solution that takes part to the reaction.

In acidic medium the ionic species is the H^+ ion[30]:

$$\text{Cathode: } 4H^+ + 4e^- \rightarrow 2H_2, E^\circ = 0.0V$$

$$\text{Anode: } 2H_2O \rightarrow O_2 + 4H^+ + 4e^-, E^\circ = +1.23V$$

$$\text{Global reaction: } 2H_2O \rightarrow O_2 + 4H^+ + 4e^-, \Delta E^\circ = 1.23V$$

In basic medium the ionic species is hydroxide ion OH^-[30]:

$$\text{Cathode: } 4H_2O + 4e^- \rightarrow 2H_2 + 4OH^-, E^\circ = -0.828V$$

$$\text{Anode: } 4OH^- \rightarrow O_2 + 2H_2O + 4e^-, E^\circ = +0.401V$$

$$\text{Global reaction: } 2H_2O \rightarrow O_2 + 4H^+ + 4e^-, \Delta E^\circ = 1.23V$$

In neutral medium both of the species are present in solution but their concentration is very low for this reason the reaction start from neutral water[30].

$$\text{Cathode: } 4H_2O + 4e^- \rightarrow 2H_2 + 4OH^-, E^\circ = -0.413V$$

$$\text{Anode: } 2H_2O \rightarrow O_2 + 4H^+ + 4e^-, E^\circ = +0.817V$$

$$\text{Global reaction: } 2H_2O \rightarrow O_2 + 4H^+ + 4e^-, \Delta E^\circ = 1.23V$$

Different pH values have different effects on the efficiency of the half-reactions, for the HER an acidic medium is the best condition for maximum efficiency but, under these conditions, the only materials capable of catalyzing the OER reaction are oxides of precious metals[31]. Meanwhile the efficiency of OER is maximized in alkaline medium but, on the other hand, there are no H^+ ions readily available at the cathode at high pH[32]. Furthermore, water splitting occurs at high cell potential (1.8-2.0V) for commercial electrolysers, about 0.55 to 0.7V higher than the theoretical value (1.23V)[26]. This extra potential is needed to overcome the energy barrier of the reaction system and is called overpotential. Overpotential is due to many factors such as the contact and solution resistance, the distance between the electrodes, conductivity of the electrodes. This means that to carry out the process of water splitting a potential higher than the thermodynamic potential is needed, a decrease of overpotential can be reached by using highly active electrocatalysts.

1.2.3 Types of electrolysers

Water electrolysers can be classified in to three types based on their electrolyte, operating conditions and ionic agents (OH^-, H^+ and O^{2-})[33]. The three kinds of electrolysers are: PEM water electrolyser, solid oxide electrolyser (SOE) and alkaline water electrolyser (AWE).

PEM electrolyser

PEM electrolysis has been known for over sixty years and was developed by General electric, where a solid sulfonate polystyrene membrane is used as the electrolyte. The proton exchange membrane acts as both the gas separator and the electrolyte. Only deionized water is injected into the cell without any electrolytic additives. There are a variety of advantages of PEM electrolysis, low gas permeability, wide operating temperatures (20-80°C), easy handling and maintenance[33]. However, the popular electrocatalysts for PEM electrolysis are precious metals (Pt, Ir, Ru), the exorbitant cost of these precious metal makes PEM electrolysis a relatively high investment.

Solid oxide electrolyser (SOE).

SOE has received an enormous amount of attention because of its high efficiency and environmental friendliness, the needed electrical power could be provided by sustainable energy sources[34]. However, SOE works at high temperatures (500–850°C) and pressure, water is in the form of steam during the SOE process. The most commonly used electrolyte material is yttria-stabilized zirconia, the conventional high-temperature oxygen-ion conductor[33]. However, the high temperatures result in the fast deterioration of catalytic performance, and achieving the long-term operation of SOE is a challenge[34]. Meanwhile, the produced hydrogen can form a mixture with steam and needs an additional procedure to acquire high purity hydrogen.

Alkaline water electrolyser (AWE).

Alkaline electrolysis highlights among other technologies since it is the one with greater maturity and the larger commercial outreach[35]. The system is constituted by a pair of electrodes immersed in an alkaline solution, usually potassium hydroxide (KOH) at a concentration of 25 to 30%, and separated by a diaphragm. At the cathode water is split to form H_2 and releasing hydroxide anions which pass through the diaphragm and recombine at the anode to form O_2, as described in the previous paragraph. In recent decades, advances have been made in this type of electrolysers called as advanced alkaline electrolysers. The most important points of development are[35]:

- Zero-gap configuration. It consists of minimizing the distance between electrodes to reduce ohmic losses
- New materials for the diaphragm. Previously made of asbestos, the use of inorganic membranes is investigated. Some are based on antimony polyacid impregnated with polymers[35], on porous composite composed of polysulfonate matrix and ZrO_2 (Zifron)[36], or on polyphenol sulfide (Ryton)[35].
- Temperature increase. The temperature is increased to promote electrolytic conductivity and improve reaction kinetics at the electrodes.
- Electrocatalytic materials. Such materials are developed to reduce overpotentials at the electrodes.

1.3 – HER AND OER

1.3.1 – HER

The hydrogen evolution reaction is an electrochemical process that, in acidic medium, involves the reduction of hydronium ions (H_3O^+) to gaseous hydrogen. From a thermodynamic point of view, this multi-step electrode reaction should occur at the potential of the reference hydrogen electrode (RHE). The first step of this reaction is the reduction of a proton on an active site of the catalyst surface (Volmer step), followed by the evolution of molecular H_2, either through a second proton/electron transfer (Heyrovsky step) or through the combination of two adsorbed protons (Tafel step)[37] :

$$\text{(Volmer) } H_3O^+ + e^- + A \rightarrow H_{ads} + H_2O$$

$$\text{(Heyrovsky) } H_{ads} + H_3O^+ + e^- \rightarrow H_2 + H_2O$$

$$\text{(Tafel) } 2H_{ads} \rightarrow H_2$$

Where *A* describes an active site on the electrode, ready to adsorb an ion, meanwhile with H_{ads} describes an adsorbed ion.

In alkaline/neutral conditions, the Volmer and Heyrovsky steps involve the hydroxide ion while the Tafel step remains unchanged[37]:

$$\text{(Volmer) } H_2O + e^- + A \rightarrow H_{ads} + OH^-$$

$$\text{(Heyrovsky) } H_{ads} + H_2O + e^- \rightarrow H_2 + OH^-$$

The difference between the acidic conditions and the alkaline/neutral conditions is that in alkaline/neutral conditions the H_{ads} intermediates are formed by dissociation of H_2O (fgure 1.7). The strength of the bond between hydrogen ions and the catalyst is universally significant for the HER kinetics of electrocatalysts. According to Sabatier's principle, ideally, the formed bonds on the electrocatalysts should be neither too weak nor too strong to facilitate the formation of the intermediates and the release of H_2

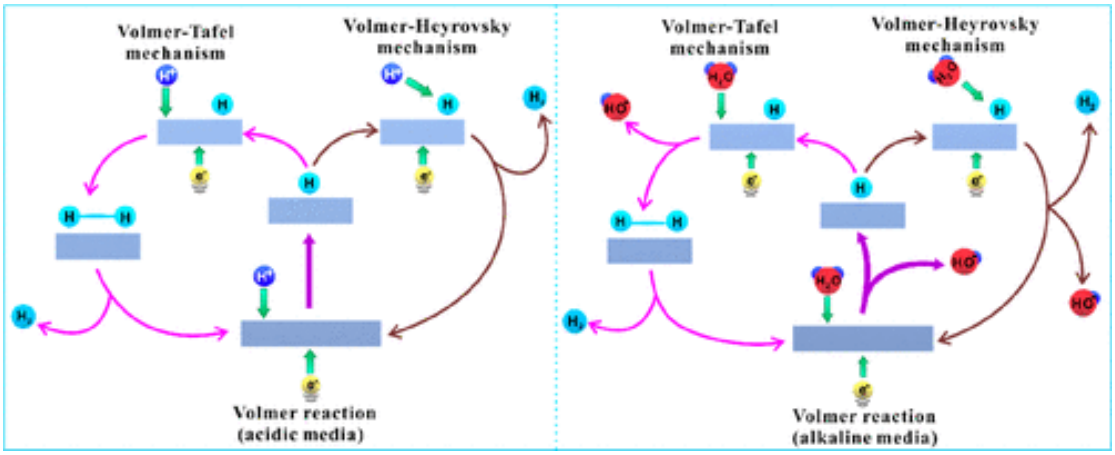

Figure 1.3 graphic representation of the mechanism of HER on the surface of an electrode in acidic (left) and alkaline (right) medium. Reprinted from [52].

1.3.2 – OER

The oxygen evolution reaction is often regarded as the main bottleneck in water splitting due to its slow kinetics, which limits the efficiency of the energy conversion[38]. The widely accepted OER mechanism consists of four-electron transfer steps in both acidic and alkaline media. The OER is highly pH-sensitive under acidic conditions, water molecules (H_2O) are oxidized, $H^+ + e^-$ pairs and oxygen molecules (O_2) are released. In contrast, under alkaline conditions, hydroxyl groups (OH^-) are oxidized to H_2O and O_2 with concomitant release of e^-.

Considering the four-electron reaction mechanism for OER under acidic conditions, the overall water oxidation reaction is[38]:

$$2H_2O \rightarrow O_2 + 4H^+ + 4e^-$$

The reaction is generally believed to proceed in four steps:

$$H_2O + \mathrm{A} \rightarrow OH_{ads} + H^+ + e^-$$

$$OH_{ads} \rightarrow O_{ads} + H^+ + e^-$$

$$H_2O + O_{ads} \rightarrow OOH_{ads} + H^+ + e^-$$

$$OOH_{ads} \rightarrow \mathrm{A} + O_2 + H^+ + e^-$$

Where "A" represents the active site of the catalyst, OOH_{ads}, O_{ads}, OH_{ads} represent the species adsorbed on the active site.

Unlike under acidic conditions, the overall water oxidation reaction under alkaline conditions is[38]:

$$4OH^- \rightarrow O_2 + 2H_2O + 4e^-$$

This reaction is usually assumed to proceed in four elementary steps:

$$\mathrm{A} + OH^- \rightarrow OH_{ads} + e^-$$

$$OH_{ads} + OH^- \rightarrow O_{ads} + H_2O + e^-$$

$$O_{ads} + OH^- \rightarrow OOH_{ads} + e^-$$

$$OOH_{ads} + OH^- \rightarrow A + O_2 + H_2O + e^-$$

Both in acidic and alkaline medium the OER involves multiple elementary steps, including the adsorption of water molecules onto the electrode surface, the formation of intermediate species, the transfer of electrons to these intermediates, and the release of oxygen gas. The major difference is that in alkaline medium hydroxide ions are readily available to be adsorbed. The OER standard potential is 1.23 V at pH=0 but the operating potentials required to reach current densities practical interests are higher, typically 2.0 V[39]. Water splitting can be promoted by using an alternative anodic reaction to replace OER. Organic/inorganic small-molecule electro-oxidation reactions (EORs) at the anode have attracted increasing attention, because the advantages of low thermodynamic potential[40]. Varius alcohols are applied in electrochemical oxidation because of their low toxicity and the potential of carbon-neutral transformation. For example methanol has advantages of low cost, high activity, high water solubility, abundance and high-density hydrogen (12.6 wt%)[40].

1.3.3 – Catalysts for HER and OER

According to the Sabatier principle, like mentioned before, the interaction between catalysts and reactive intermediates should be appropriate. If the interaction is too weak, too few intermediates bind to the surface of the catalyst, slowing down the reaction, while if the interaction is too strong, the reaction products fail to dissociate and cease the reaction by blocking the active sites[41]. From the physical chemistry perspective, both the H_{ads} adsorption and H_2 desorption can be evaluated by measuring the $\Delta G_{H_{ads}}$ for the HER reaction process. The Sabatier principle dictates that under the ideal conditions $\Delta G_{H_{ads}}$ should be zero with the highest exchange current (j_0). The exchange current is the total current flowing across the interface when the potential is equal to the reversible or equilibrium potential of the reaction. In general, higher the j_0, better the activity[41]. The volcano plot describe the trend of j_0 with $\Delta G_{H_{ads}}$ figure 1.8.

According to the Nerst equation, the Nerst potential of HER referenced to the normal hydrogen electrode is zero under standard conditions. However, the practical HER processes require a greater applied potential to overcome the kinetic barriers resulting from some adverse issues, such as high activation energy and poor energy efficiency. The difference between Nerst potential and the required potential to drive HER is the corresponding overpotential(η), like mentioned before. Usually the value of overpotential needed to obtain a current density of $10\,\frac{mA}{cm^2}$ (η_{10}) is used to compare the activities of different catalysts toward the HER, a smaller η_{10} suggests a higher activity[42].

As illustrated in the volcano plot in figure 1.8 the platinum group metals (PGMs, including Pt, Pd, Ru, Ir and Rh) located close to the apex of the volcano curve demonstrate excellent catalytic performance toward HER, compared with other metals. Pt is the most efficient electrocatalyst for HER with “quasi-zero” onset overpotential. As the Sabatier principle explains, the moderate M—H bond strength indicates the optimized adsorption and desorption of hydrogen at the surface of Pt which lead to the high catalytic efficiency. Although the precious-metal based electrocatalyst have demonstrated splendid activities toward HER, their scarcity and high costs impede their practical applications on a large scale. Hence, to drive the costs down its imperative to produce non-noble-metal catalyst[43]. Low cost catalysts are mainly transition metal based, some examples are: transition metal oxides (TMOs), transition metal nitrides (TMNs), transition metal carbides (TMCs) and transition metal phosphides (TMPs) [43].

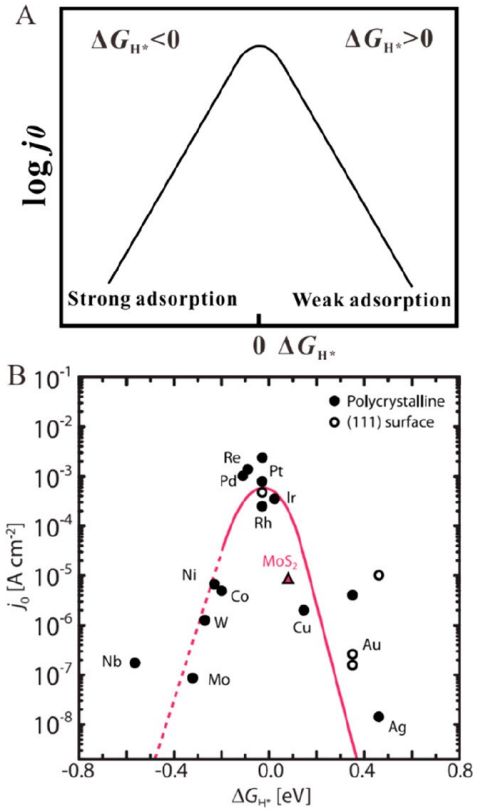

Figure 4 relationship between j_0 and $\Delta G_{H_{ads}}$. reprinted from [43].

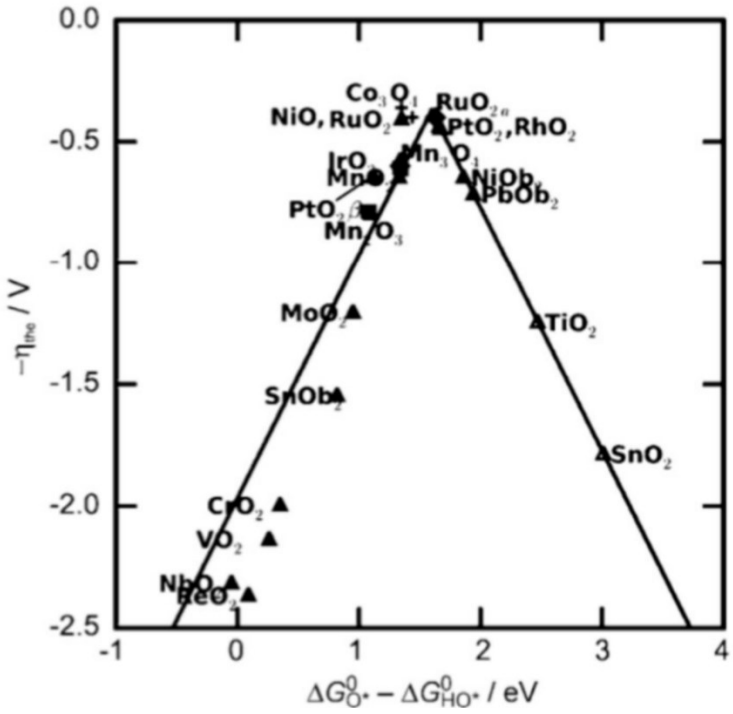

Figure 1.9 volcano plot for the OER reprinted from [39].

Nobel metals, their alloys and oxides as well as their composites are the most studied catalyst for the OER due to their excellent performance, this is demonstrated also by their position on top of the volcano plot in figure 1.9[39]. It is experimentally proved that iridium (Ir) and ruthenium (Ru) materials are more active towards OER compared to Platinum (Pt) and palladium (Pd)[44]. Ir and Ru are considered as the state-of-the-art OER electrocatalysts[44]. Transition metal oxides are an example of possible substitutes of noble metals as OER

catalysts, they are interesting because of their low-cost and good corrosion resistance. Especially, they are excellent candidates for OER due to their multivalent oxidant states[45]. The OER activities of these materials are highly dependent on the morphology, composition, oxidation state, the 3d electron number of the transition metal ions and other factors[46].

1.4 – UOR

To reduce the cost of hydrogen production it is important to use catalysts that are both active, so less energy is needed, but also cheap because the large scale production of electrolysers with platinum catalyst it is not sustainable[47]. In the last paragraph it was mentioned that for both HER and OER is possible to use transition metal based catalysts that are far cheaper than the noble metals ones. This does not change the fact that the oxygen evolution reaction undergoes complex and slow $4e^-$ transfer processes, resulting in a decrease in overall efficiency of electrical-water splitting. Urea oxidation reaction (UOR) received much interest in recent years because of smaller thermodynamic potential (0.37 V Vs RHE) than that of OER (1.23 V Vs RHE)[48]. Urea is also present in wastewater streams, particularly in urban and agricultural runoff. Urea oxidation can be integrated into wastewater treatment processes to remove urea from water sources, preventing eutrophication and harmful algal blooms[48]. Thus, it seems that electrochemical treatment of urea-containing wastewaters or urea-assisted water splitting is a more economically feasible way to produce hydrogen[49,50]. In addition, urea is cheap, abundant, relatively safe, and easy to storage and transport, and can be directly used in fuel cells to replace conventional hydrogen at the anode[51,52]. Swapping the OER with the UOR can help decrease both cost of hydrogen production and pollution. However, due to the complicated six-electron transfer process depicted in equation (1), UOR suffers from sluggish kinetics, and high overpotential is always required to overcome the reaction barriers, leading to more energy consumption[53,54]. Thus, highly active, stable and affordable UOR catalysts are indispensable for widespread applications or these urea-related technologies in the future. Figure 1.10 shows how the substitution of the OER with the UOR can be extremely beneficial for the production of hydrogen. Using the same material as catalyst the potential at which a current density of 50 mA/cm^2 is reduced by almost 0.6 V.

$$6OH^- + (NH_2)_2CO \rightarrow 5H_2O + N_2 + CO_2 + 6e^- \quad (1)$$

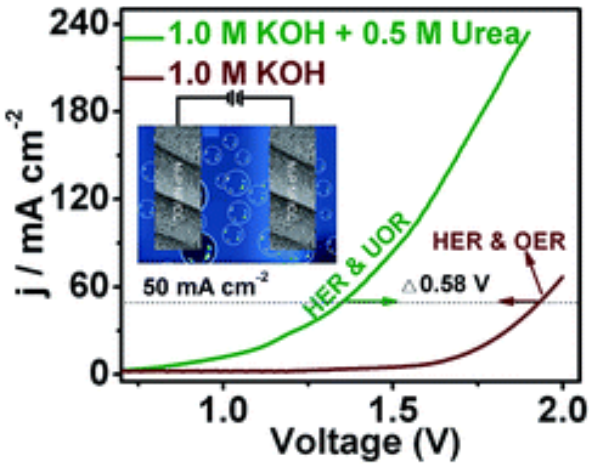

Figure 1.10 LSV curves of a Ni_2P-based catalyst in 1M KOH (red curve) and in 1M KOH + 0.5M urea (green). In presence of urea a geometric current density of 50 mA/cm^2 is reached at a potential 580 mV lower than in absence of urea. Reprinted from [51].

Urea can be oxidized in acidic, neutral or alkaline electrolytes. For acidic UOR, few electrolysers can survive in an acidic environment under high overpotentials for a long time, which is quite similar to the problem faced by acidic OER[55,56]. Besides the stability problem of UOR catalysts, the acidic environment leads to generation of acidic fog, which will corrode the reaction cell and contaminate the generated hydrogen[55]. Since NaCl is one of the main components in real urine, urea oxidation in neutral NaCl medium was also investigated before[57]. However Cl_2 is produced which is harmful for the environment and human beings. Moreover, the production of H^+ during neutral UOR indicates that only noble metal-based catalysts can possibly survive long-time operation. Therefore, compared to acidic or neutral UOR, alkaline UOR is more promising. For alkaline UOR, owing to the intrinsic higher activities, Ni-based catalysts have been more widely investigated among all transition metal-based catalysts. In fact, earlier research studies in biocatalysis demonstrate that urease, which contains two Ni(II) ions with a bridging hydroxide group as active sites, can efficiently catalyze the hydrolysis of urea to produce carbon dioxide and ammonia[58]. Though there are some differences between biocatalysis and electrocatalysis, it possibly explains why Ni-based catalysts can accelerate the electrocatalytic urea oxidation process. For Ni-based catalysts generally the on-set potential of the UOR is quite close to the potential where NiOOH is generated, suggesting that NiOOH is probably the active site for the UOR[59]. Different studies were conducted to clarify the mechanism of UOR catalyzed by Ni-based materials[60–63]. Therefore, it is generally accepted that the electroactive species of Ni-based catalysts for the UOR in alkaline electrolyte is NiOOH, and the UOR on Ni-based electrodes follows an electrochemical oxidation-chemical oxidation mechanism. In detailed, Ni-based catalysts first undergo an electrochemical oxidation process to generate NiOOH species on the surfaces, then the as-generated NiOOH chemically catalyzes the oxidation of urea to produce N_2 and CO_2, and NiOOH is reduced to Ni oxide/hydroxide simultaneously.

Electrochemical oxidation:

$$Ni(OH)_2 + OH^- \rightarrow NiOOH + H_2O + e^-$$

Chemical oxidation:

$$CO(NH_2)_2 + 6NiOOH + H_2O \rightarrow N_2 + CO_2 + 6Ni(OH)_2$$

To have a better understanding of the UOR, Botte et al. used the density functional theory (DFT) method to investigate the exact process of urea oxidation on NiOOH[64]. The DFT results show that urea molecules are first absorbed on NiOOH through bridging coordination. As illustrated in figure 1.11, one O atom from NiOOH is linked to the C atom of the urea molecule. The detailed reaction pathway for urea dissociation on NiOOH in an alkaline environment was proposed as:

$^*CO(NH_2)_2 \rightarrow {}^*CO(NH_2{\cdot}NH) \rightarrow {}^*CO(NH_2{\cdot}N) \rightarrow {}^* CO(NH{\cdot}N) \rightarrow^* CO(N_2) \rightarrow^*CO(OH) \rightarrow^*COO$

The rate-determining step for the UOR is the desorption of the *COO intermediate form the NiOOH surface.

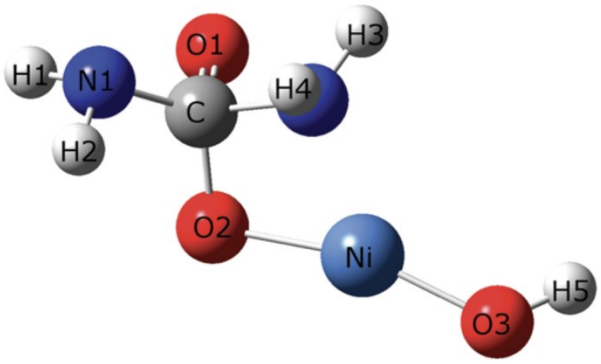

Figure 1.11 Optimized structure for urea adsorption on NiOOH. Reprinted from [67].

1.4.1 UOR catalysts

Nickel-based catalysts are the most widely investigated electrode materials for UOR, and they have been reported to efficiently oxide urea in alkaline solutions. However, other types of catalysts have been studied. Botte and coworkers studied UOR on Pt, Rh, Ir and intermetallic PtIr, all of which were deposited on Ti foil[48]. It was found that the electrocatalytic activity of these materials towards UOR was inferior of pure nickel. Later, King and Botte synthesized intermetallic mixtures of noble metals with Ni, including PtNi, PtIRNi, RuNi, and RhNi and examined them as catalysts for the UOR[65]. All the aforementioned materials showed current densities that were greater than ones reached by pure nickel at the same potentials. RhNi was the most active exhibiting a current density of 80 mA/cm^2 at 0.7 V Vs Hg/HgO, against the 28 mA/cm^2 of pure nickel. From these studies it is clear that nickel-based materials are both cheaper and more active than noble-metal based catalysts. Other types of catalysts that have been studied include Spinel and Perovskite Catalysts. Spinel-type binary metal oxides of the form AB_2O_4 (A,B = Co, Mn, Fe etc.) have attracted considerable attention as functional materials, due to their rich redox chemistry, low cost, high electronic conductivities and relevance to a wide range of energy storage applications[48]. An example of Spinel catalyst used for the UOR is $NiCo_2O_4$[69]. The activity of the Spinel was compared with that of Co_2O_4, and the former showed a higher anodic current density of 136 mA/cm^2 at 0.7 Vs Hg/HgO, whereas the latter gave only 65 mA/cm^2 in the same conditions. While perovskite catalysts like $NiMoO_4$ reach high current densities but underwent surface restructuring upon extended potential cycling[66]. NiOH-based materials are the benchmark for UOR catalysts, they were one of the first materials used for this application but are still one of the best performers[48]. Wang et al. reported UOR on exfoliated $Ni(OH)_2$ nanosheets and found this material to be more active than bulk-$Ni(OH)_2$, exhibiting a current density of 154 mA/cm^2, which is about 170 times higher than the bulk $Ni(OH)_2$[67]. This activity was attributed to the higher surface area of the exfoliated material. Other than increasing the surface area there are other methods to increase the activity of $Ni(OH)_2$, for example introducing foreign atoms in the structure. Zhu et al. reported metallic β-$Ni(OH)_2$ nanosheets as a superior catalyst for UOR, compared with pristine $Ni(OH)_2$[68]. The authors produced this metallic material by incorporating sulfur into $Ni(OH)_2$ in the presence of H_2S. They demonstrated a roughly 20-fold increase in the peak UOR current relative to that of pristine $Ni(OH)_2$. The incorporation of sulfur into $Ni(OH)_2$ leads to synergistic effects, thereby increasing the number of active sites and improving electron transport. A part from Ni oxides and hydroxides, heavier chalcogenides of Ni have recently generated significant interest as catalysts for the UOR, and this can be attributed to their low cost and improved electrochemical performance[69–72]. Khalafallah et al. described the one-pot hydrothermal synthesis of a NiCo selenide, and demonstrated its use as an advanced electrode for UOR[69]. Thus, cobalt substitution promotes Ni oxidation and decreases the overpotential. In a very recent report by another group,

Liu et al. introduced Ni_2P nanoflakes as high-performance UOR catalysts[73]. This nanoflakes were synthesized through phosphorization of β-$Ni(OH)_2$, and exhibited a UOR current density of 95 mA/cm^2 at 1.60 V Vs RHE in 1M KOH and 0.5M urea. Their activity comparable with the current state-of-the-art UOR catalysts, including β-$Ni(OH)_2$ itself. The authors link the activity of the Ni_2P nanoflakes to phosphate ions that are generated in situ at their surface, and promote the conversion of inactive Ni_2P into the catalytically active NiOOH.

1.5 Thesis objectives

Many of the catalysts described in Section 1.4.1 are based on nonprecious metals, and most of these systems involve nickel in various chemical and structural forms. In this work, nickel hydroxide has been chosen as the benchmark material. $Ni(OH)_2$ will be modified by introducing a second metal in the structure (manganese or molybdenum). Seven total samples have been obtained: pure nickel hydroxide, three samples with different Mn content (3, 5 and 8 at%) and three samples with different Mo content (8, 20 and 30 at%). These samples have been studied as UOR catalysts. The main objective is to understand if the presence of the foreign elements can increase the UOR activity and which of the two elements is the best choice. Nickel phosphide-based materials have been obtained from the phosphorization of the nickel hydroxide-based materials. These samples have been tested as UOR and HER catalysts. The objectives are to understand if the phosphorization can increase the activity towards the different reactions and if the presence of the foreign atoms influences the behavior of these materials.

Bibliography

1. Morris, J. F., Reilly, J. M. & Chen, Y.-H. H. Advanced technologies in energy-economy models for climate change assessment. *Energy Economics* **80**, 476–490 (2019).
2. Haines, A. Health Effects of Climate Change. *JAMA* **291**, 99 (2004).
3. Konisky, D. M., Hughes, L. & Kaylor, C. H. Extreme weather events and climate change concern. *Climatic Change* **134**, 533–547 (2016).
4. Cleland, J. World Population Growth; Past, Present and Future. *Environ Resource Econ* **55**, 543–554 (2013).
5. Sayed, E. *et al.* Renewable Energy and Energy Storage Systems. *Energies* **16**, 1415 (2023).
6. Soeder, D. *Energy Futures: The Story of Fossil Fuel, Greenhouse Gas, and Climate Change*. (Springer International Publishing, Cham, 2022). doi:10.1007/978-3-031-15381-5.
7. Arent, D. J., Wise, A. & Gelman, R. The status and prospects of renewable energy for combating global warming. *Energy Economics* **33**, 584–593 (2011).
8. Ould Amrouche, S., Rekioua, D., Rekioua, T. & Bacha, S. Overview of energy storage in renewable energy systems. *International Journal of Hydrogen Energy* **41**, 20914–20927 (2016).
9. Ehret, O. & Bonhoff, K. Hydrogen as a fuel and energy storage: Success factors for the German Energiewende. *International Journal of Hydrogen Energy* **40**, 5526–5533 (2015).
10. Tarhan, C. & Çil, M. A. A study on hydrogen, the clean energy of the future: Hydrogen storage methods. *Journal of Energy Storage* **40**, 102676 (2021).
11. Ni, M. An Overview of Hydrogen Storage Technologies. **24**, (2006).
12. Edwards, P. P., Kuznetsov, V. L., David, W. I. F. & Brandon, N. P. Hydrogen and fuel cells: Towards a sustainable energy future. *Energy Policy* **36**, 4356–4362 (2008).
13. Jain, I. P. Hydrogen the fuel for 21st century. *International Journal of Hydrogen Energy* **34**, 7368–7378 (2009).
14. Fan, L., Tu, Z. & Chan, S. H. Recent development of hydrogen and fuel cell technologies: A review. *Energy Reports* **7**, 8421–8446 (2021).
15. Crabtree, G. W. & Dresselhaus, M. S. The Hydrogen Fuel Alternative. *MRS Bull.* **33**, 421–428 (2008).
16. Najjar, Y. S. H. Hydrogen safety: The road toward green technology. *International Journal of Hydrogen Energy* **38**, 10716–10728 (2013).
17. Yang, F. *et al.* Review on hydrogen safety issues: Incident statistics, hydrogen diffusion, and detonation process. *International Journal of Hydrogen Energy* **46**, 31467–31488 (2021).
18. Ishaq, H., Dincer, I. & Crawford, C. A review on hydrogen production and utilization: Challenges and opportunities. *International Journal of Hydrogen Energy* **47**, 26238–26264 (2022).
19. Barelli, L., Bidini, G., Gallorini, F. & Servili, S. Hydrogen production through sorption-enhanced steam methane reforming and membrane technology: A review. *Energy* **33**, 554–570 (2008).
20. Song, C., Liu, Q., Ji, N., Kansha, Y. & Tsutsumi, A. Optimization of steam methane reforming coupled with pressure swing adsorption hydrogen production process by heat integration. *Applied Energy* **154**, 392–401 (2015).
21. Li, A., Lim, C. J. & Grace, J. R. Staged-separation membrane reactor for steam methane reforming. *Chemical Engineering Journal* **138**, 452–459 (2008).
22. Brockmeier, N. F. Model Description.
23. Navas-Anguita, Z., García-Gusano, D., Dufour, J. & Iribarren, D. Revisiting the role of steam methane reforming with CO2 capture and storage for long-term hydrogen production. *Science of The Total Environment* **771**, 145432 (2021).
24. Tee, S. Y. *et al.* Recent Progress in Energy-Driven Water Splitting. *Advanced Science* **4**, 1600337 (2017).
25. Ifkovits, Z. P., Evans, J. M., Meier, M. C., Papadantonakis, K. M. & Lewis, N. S. Decoupled electrochemical water-splitting systems: a review and perspective. *Energy Environ. Sci.* **14**, 4740–4759 (2021).
26. Safari, F. & Dincer, I. A review and comparative evaluation of thermochemical water splitting cycles for hydrogen production. *Energy Conversion and Management* **205**, 112182 (2020).
27. Ahmad, H., Kamarudin, S. K., Minggu, L. J. & Kassim, M. Hydrogen from photo-catalytic water splitting process: A review. *Renewable and Sustainable Energy Reviews* **43**, 599–610 (2015).

28. Chen, L. *et al.* Comprehensive Understanding of the Electrocatalytic Mechanism for Co/Fe/Cu Doped Ni(OH) $_2$ on Urea Oxidation Reactions: Theory and Experiment. *ACS Sustainable Chem. Eng.* **12**, 10466–10474 (2024).
29. Das, D., Khanna, N. & Veziroğlu, N. Recent developments in biological hydrogen production processes. *CI&CEQ* **14**, 57–67 (2008).
30. Raveendran, A., Chandran, M. & Dhanusuraman, R. A comprehensive review on the electrochemical parameters and recent material development of electrochemical water splitting electrocatalysts. *RSC Adv.* **13**, 3843–3876 (2023).
31. Peng, Y. *et al.* Recent Advances Regarding Precious Metal-Based Electrocatalysts for Acidic Water Splitting. *Nanomaterials* **12**, 2618 (2022).
32. Yu, J., Le, T. A., Tran, N. Q. & Lee, H. Earth-Abundant Transition-Metal-Based Bifunctional Electrocatalysts for Overall Water Splitting in Alkaline Media. *Chemistry A European J* **26**, 6423–6436 (2020).
33. Shiva Kumar, S. & Himabindu, V. Hydrogen production by PEM water electrolysis – A review. *Materials Science for Energy Technologies* **2**, 442–454 (2019).
34. Wolf, S. E. *et al.* Solid oxide electrolysis cells – current material development and industrial application. *J. Mater. Chem. A* **11**, 17977–18028 (2023).
35. David, M., Ocampo-Martínez, C. & Sánchez-Peña, R. Advances in alkaline water electrolyzers: A review. *Journal of Energy Storage* **23**, 392–403 (2019).
36. Vermeiren, P., Adriansens, W., Moreels, J. P. & Leysen, R. EVALUATION OF THE ZIRFON@j SEPARATOR FOR USE IN ALKALINE WATER ELECTROLYSIS AND Ni-H, BATTERIES.
37. Ferriday, T. B., Middleton, P. H. & Kolhe, M. L. Review of the Hydrogen Evolution Reaction—A Basic Approach. *Energies* **14**, 8535 (2021).
38. Tahir, M. *et al.* Electrocatalytic oxygen evolution reaction for energy conversion and storage: A comprehensive review. *Nano Energy* **37**, 136–157 (2017).
39. Plevová, M., Hnát, J. & Bouzek, K. Electrocatalysts for the oxygen evolution reaction in alkaline and neutral media. A comparative review. *Journal of Power Sources* **507**, 230072 (2021).
40. Liu, X. *et al.* Electrochemical Hydrogen Generation by Oxygen Evolution Reaction-Alternative Anodic Oxidation Reactions. *Adv Energy and Sustain Res* **3**, 2200005 (2022).
41. Ooka, H., Huang, J. & Exner, K. S. The Sabatier Principle in Electrocatalysis: Basics, Limitations, and Extensions. *Front. Energy Res.* **9**, 654460 (2021).
42. Lasia, A. Mechanism and kinetics of the hydrogen evolution reaction. *International Journal of Hydrogen Energy* **44**, 19484–19518 (2019).
43. Li, D. Y. *et al.* Highly active non-noble electrocatalyst from Co2P/Ni2P nanohybrids for pH-universal hydrogen evolution reaction. *Materials Today Physics* **16**, 100314 (2021).
44. Kim, J. S., Kim, B., Kim, H. & Kang, K. Recent Progress on Multimetal Oxide Catalysts for the Oxygen Evolution Reaction. *Advanced Energy Materials* **8**, 1702774 (2018).
45. Lu, F., Zhou, M., Zhou, Y. & Zeng, X. First-Row Transition Metal Based Catalysts for the Oxygen Evolution Reaction under Alkaline Conditions: Basic Principles and Recent Advances. *Small* **13**, 1701931 (2017).
46. Feng, Y. *et al.* Role of transition metals in catalyst designs for oxygen evolution reaction: A comprehensive review. *International Journal of Hydrogen Energy* **47**, 17946–17970 (2022).
47. Yu, Z. *et al.* Clean and Affordable Hydrogen Fuel from Alkaline Water Splitting: Past, Recent Progress, and Future Prospects. *Advanced Materials* **33**, 2007100 (2021).
48. Singh, R. K., Rajavelu, K., Montag, M. & Schechter, A. Advances in Catalytic Electrooxidation of Urea: A Review. *Energy Tech* **9**, 2100017 (2021).
49. Zhang, J.-Y. *et al.* Energy-saving hydrogen production coupling urea oxidation over a bifunctional nickel-molybdenum nanotube array. *Nano Energy* **60**, 894–902 (2019).
50. Wang, Q. *et al.* A synergetic effect between photogenerated carriers and photothermally enhanced electrochemical urea-assisted hydrogen generation on the Ni-NiO/Nickel Foam catalyst. *Mater. Adv.* **2**, 2104–2111 (2021).

51. Lan, R. & Tao, S. Preparation of nano-sized nickel as anode catalyst for direct urea and urine fuel cells. *Journal of Power Sources* **196**, 5021–5026 (2011).
52. Xu, W., Wu, Z. & Tao, S. Urea-Based Fuel Cells and Electrocatalysts for Urea Oxidation. *Energy Tech* **4**, 1329–1337 (2016).
53. Hao, P. *et al.* Morphology and electronic structure modulation induced by fluorine doping in nickel-based heterostructures for robust bifunctional electrocatalysis. *Nanoscale* **10**, 20384–20392 (2018).
54. Liu, X. *et al.* Complete Reconstruction of Hydrate Pre-Catalysts for Ultrastable Water Electrolysis in Industrial-Concentration Alkali Media. *Cell Reports Physical Science* **1**, 100241 (2020).
55. Pan, Y., Abazari, R., Wu, Y., Gao, J. & Zhang, Q. Advances in metal–organic frameworks and their derivatives for diverse electrocatalytic applications. *Electrochemistry Communications* **126**, 107024 (2021).
56. Zhu, D., Wang, L., Qiao, M. & Liu, J. Phosphate ion functionalized CoP nanowire arrays for efficient alkaline hydrogen evolution. *Chem. Commun.* **56**, 7159–7162 (2020).
57. Simka, W., Piotrowski, J. & Nawrat, G. Influence of anode material on electrochemical decomposition of urea. *Electrochimica Acta* **52**, 5696–5703 (2007).
58. Barrios, A. M. & Lippard, S. J. Interaction of Urea with a Hydroxide-Bridged Dinuclear Nickel Center: An Alternative Model for the Mechanism of Urease. *J. Am. Chem. Soc.* **122**, 9172–9177 (2000).
59. Xu, W., Zhang, H., Li, G. & Wu, Z. Nickel-cobalt bimetallic anode catalysts for direct urea fuel cell. *Sci Rep* **4**, 5863 (2014).
60. Vedharathinam, V. & Botte, G. G. Direct evidence of the mechanism for the electro-oxidation of urea on Ni(OH)2 catalyst in alkaline medium. *Electrochimica Acta* **108**, 660–665 (2013).
61. Wang, D. & Botte, G. G. In Situ X-Ray Diffraction Study of Urea Electrolysis on Nickel Catalysts. *ECS Electrochemistry Letters* **3**, H29–H32 (2014).
62. Vedharathinam, V. & Botte, G. G. Understanding the electro-catalytic oxidation mechanism of urea on nickel electrodes in alkaline medium. *Electrochimica Acta* **81**, 292–300 (2012).
63. Xie, J. *et al.* Copper-incorporated hierarchical wire-on-sheet α-Ni(OH) $_2$ nanoarrays as robust trifunctional catalysts for synergistic hydrogen generation and urea oxidation. *J. Mater. Chem. A* **7**, 13577–13584 (2019).
64. Daramola, D. A., Singh, D. & Botte, G. G. Dissociation Rates of Urea in the Presence of NiOOH Catalyst: A DFT Analysis. *J. Phys. Chem. A* **114**, 11513–11521 (2010).
65. King, R. L. & Botte, G. G. Investigation of multi-metal catalysts for stable hydrogen production via urea electrolysis. *Journal of Power Sources* **196**, 9579–9584 (2011).
66. Tong, Y. *et al.* Oxygen Vacancies Confined in Nickel Molybdenum Oxide Porous Nanosheets for Promoted Electrocatalytic Urea Oxidation. *ACS Catal.* **8**, 1–7 (2018).
67. Wang, D., Yan, W. & Botte, G. G. Exfoliated nickel hydroxide nanosheets for urea electrolysis. *Electrochemistry Communications* **13**, 1135–1138 (2011).
68. Zhu, X. *et al.* Metallic Nickel Hydroxide Nanosheets Give Superior Electrocatalytic Oxidation of Urea for Fuel Cells. *Angew Chem Int Ed* **55**, 12465–12469 (2016).
69. Khalafallah, D., Ouyang, C., Zhi, M. & Hong, Z. Heterostructured Nickel-Cobalt Selenide Immobilized onto Porous Carbon Frameworks as an Advanced Anode Material for Urea Electrocatalysis. *ChemElectroChem* **6**, 5191–5202 (2019).
70. Khalafallah, D., Zou, Q., Zhi, M. & Hong, Z. Tailoring hierarchical yolk-shelled nickel cobalt sulfide hollow cages with carbon tuning for asymmetric supercapacitors and efficient urea electrocatalysis. *Electrochimica Acta* **350**, 136399 (2020).
71. Liu, Z., Zhang, C., Liu, H. & Feng, L. Efficient synergism of NiSe2 nanoparticle/NiO nanosheet for energy-relevant water and urea electrocatalysis. *Applied Catalysis B: Environmental* **276**, 119165 (2020).
72. Zhao, L., Chang, Y., Jia, M., Jia, J. & Wen, Z. Monodisperse Ni0·85Se nanocrystals on rGO for high-performance urea electrooxidation. *Journal of Alloys and Compounds* **852**, 156751 (2021).
73. Liu, H. *et al.* Ni $_2$ P nanoflakes for the high-performing urea oxidation reaction: linking active sites to a UOR mechanism. *Nanoscale* **13**, 1759–1769 (2021).

Chapter 2

Characterization techniques

The samples were characterized using X-ray diffraction (XRD), X-ray photoelectron spectroscopy (XPS), inductively coupled plasma spectroscopy (ICP), scanning electron microscopy (SEM) and X-ray absorption (XAS). In the next paragraphs these techniques will be briefly described.

2.1 X-ray diffraction (XRD)

X-ray diffraction is a non-destructive technique that determine a sample's composition or crystalline structure. This technique is based on sending X-rays through the sample. X-ray beams are chosen because their wavelength is similar to the spacing of the atoms in the sample (0.1-10 nm), the angle of diffraction will be affected by the spacing of the atoms in the sample, as opposed to using much larger wavelengths, which would be unaltered by the spacing between atoms[1].

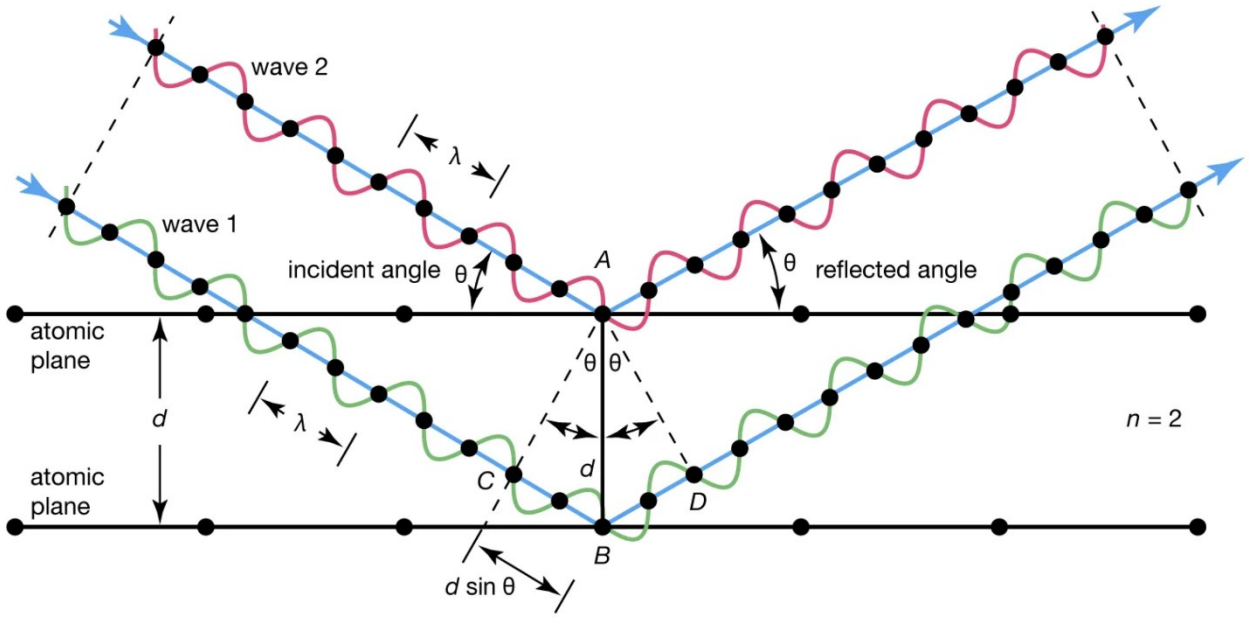

Figure 2.5 working principle of XRD. Reprinted from [1].

As shown in figure 2.1 the X-rays pass through the sample and they interact with the atoms in the structure and become scattered, these scattered waves, emitted in multiple directions, interfere with each other. The new angle of the beam after the interaction with the crystal plane is called "Theta angle" (θ). Some of this diffracted beams cancel each other out meanwhile in other cases constructive interference occurs[2]. Considering a monochromatic X-ray with wavelength "λ" incident on a crystal with an angle "θ" that gets reflected by interacting with crystal planes at a distance "d" one from another. The X-rays interacts with the sample at different depths and this produce a difference in phase between the diffracted rays. Only the in the case that the difference of path of the two waves is equal to an integer multiple of the wavelength constructive interference occurs[3].

This is described by the Bragg's Law[3]:

$$n\lambda = 2d \sin\theta$$

Knowing this correlation between the diffraction angle and atomic planes distance make it possible to obtain a diffractogram by performing a scanning changing the incidence angle while keeping constant the wavelength. The result of X-ray diffraction plots the intensity of the signal for different values of twice the incident angle (2θ), which in figure 2.1 represent the angle between the incident ray and the diffracted ray.

XRD is used for determining diffraction intensities and peak positions of a sample while Bragg's law is used for calculation corresponding interplanar spacing. Constituent phases can be identified by computerized searching and comparing the result with values stored in a database. What causes constructive interference in solids is the orderly arrangement of atomic structures. There is a strong correlation between periodicity and diffraction: lower diffraction angles are observed with longer periodicity and vice versa[4]. In the case of amorphous materials, due to the absence of periodicity, the XRD graph indicates the maximum average peak at a certain 2θ value while crystalline materials ideally present several narrow peaks at different 2θ values[4] (figure 2.2). Also from the width of the peaks is possible to extract information, in particular the width is inversely proportion to the crystal size. A thin peak corresponds to a bigger crystal meanwhile a broader peak means that there may be a smaller crystal, defect in the crystalline structure or that the sample might be amorphous[5].

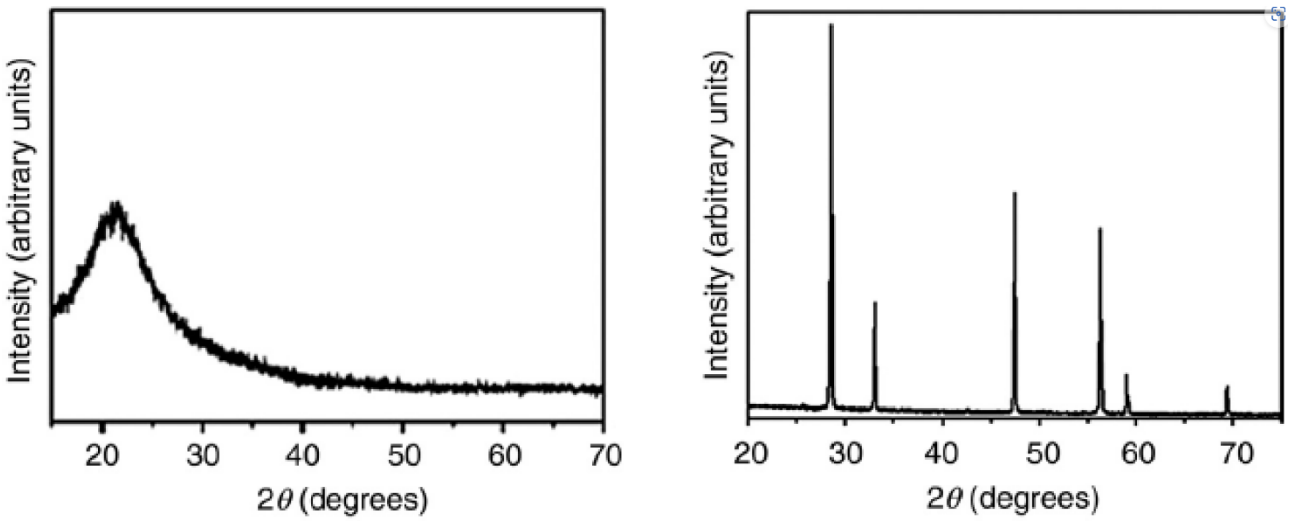

Figure 6.2 example of a XRD graph, amorphous material (on the left) and a crystalline material (on the right). Reprinted from [4]

The X-rays used during XRD analysis can be generated in different ways such as synchrotron and X-ray tubes, the latter option is the most common one for XRD instruments. X-rays are produced when highly energetic electrons interact with matter, converting some or all of their kinetic energy in electromagnetic radiation[6]. The X-ray tube contains an electron source, a vacuum environment, and a target electrode, an external power source provides high voltage to accelerate the electrons. An electrical potential difference is applied between the electrodes. The negative pole of the voltage is applied to the cathode, which is also the source of electrons (by thermionic effect), and the positive pole is applied to the anode, the target of electrons. Electrons are emitted then they are accelerated by the tube potential through the vacuum to hit the anode. When electrons interact with the anode their kinetic energy is converted to other form of energy, mainly heat, but the electrons that reach the proximity of an atomic nucleus are decelerated and photons are emitted. The energy lost by the electrons is determined by the distance from the positive charge, shorter distance translates to higher energy photons meanwhile longer distance to lower energy photons, a direct impact with the nucleus converts all the kinetic energy of the electron to an equivalent energy photon[7]. The X-rays generated by this

effect are called “Bremsstrahlung radiation”. In addition to the continuous bremsstrahlung x-ray spectrum, discrete x-ray energy peaks called “characteristic radiation” are present, with x-ray energies depending on the elemental composition of the anode and the applied X-ray tube voltage[7]. This photons are emitted when the kinetic energy of the incident electrons is higher than the binding energy of an electron in a target atom. An interaction can eject an electron creating a vacancy that can be filled by an outer shell electron with lower binding energy, and a photon with energy equal to the difference in binding energy between the two electrons of the atom is emitted. The wavelength of the characteristic radiation depends on the material used for the anode and on the potential applied because only if the energy of the incidents electrons exceed the binding energy of the electrons in the target this effect occurs. The most used materials are Copper, Molybdenum, Chromium and Cobalt, usually the K_α peak is chosen since is the most intense[7]. XRD can be used to analyze samples in the form of single crystals or powders. Most of powder diffractometers use Bragg-Brentano geometry, the incident angle between X-ray source and the sample is always half of the detector angle 2θ and they remain the same during the scanning.

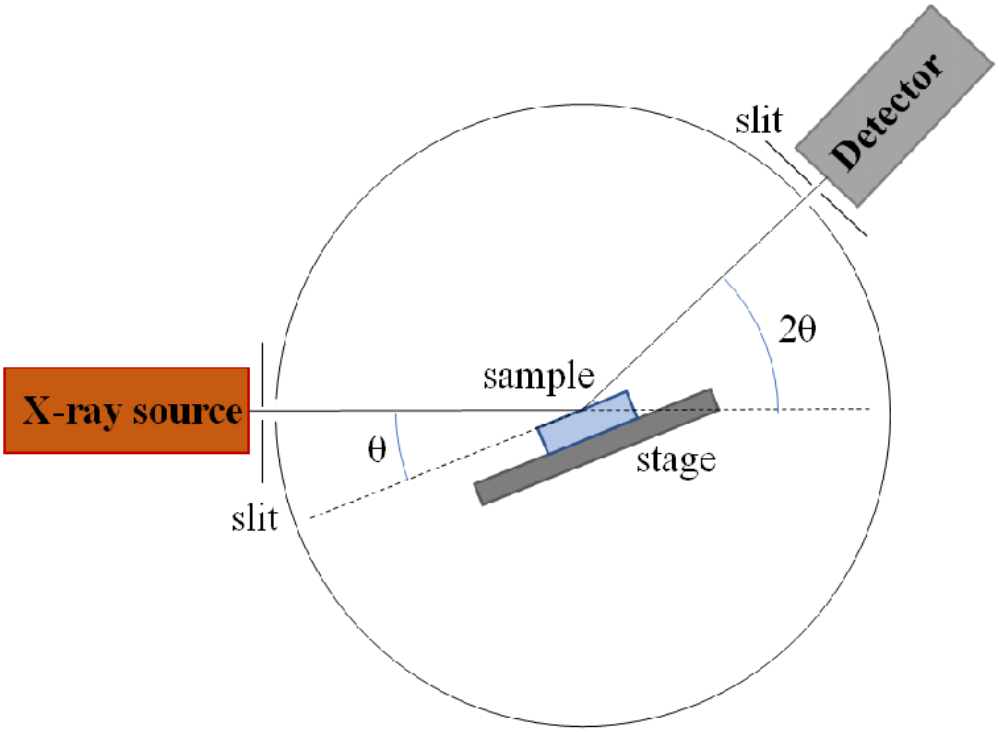

Figure 7 Bragg-Brentano geometry. Reprinted from [3].

In this work the XRD spectra were obtained using an “Aeris Mineral” from Panalytical in Bragg-Brentano geometry, operating with Cu K_α radiation (λ = 0.15406 nm) generated at 40 kV and 30 mA. All the measurements in this work were done on powders. The preparation of the sample was always the same and it simply consisted in taking a small amount of powder and carefully drop it in the sample holder in a way that all the empty space was filled and the surface was flat. To make sure that this characteristic the powder was pressed with the help of a spatula.

2.2 Scanning electron microscopy (SEM)

Scanning electron microscope (SEM) is one of the common methods for imaging the microstructure and morphology of the materials. Similar to how light microscopes utilize light for imaging, electron microscopes use electrons. SEMs have better resolution than light microscopes because electrons have a considerably smaller wavelength than light[8]. Scanning electron microscopes use an electron gun to emit electrons that are

focused into a beam with a size of around 5 nm. Figure 2.4 reports a scheme of a scanning electron mucroscope. Electrons are accelerated to energy values in the range of a few hundred eV to 50 KeV. As the electrons impact and penetrate the surface, different interaction occur that result in the emission of electrons and photons and scanning electron microscopy images are formed by collecting the released electrons on a cathode ray tube[8]. Different scanning electron microscope procedures are classified based on what is later detected. The principle images produced in SEM are of three types: secondary electron images, backscattered electron images and elemental X-ray maps. When electrons are accelerated they gain considerable amounts of kinetic energy. This energy is then converted in different forms when the electrons interact with the sample: secondary electrons (which are responsible for the production of SEM image), backscattered electrons (BSE), diffracted backscattered electrons (EBSD), photons (characteristic X-ray that are utilized for elemental analysis), visible light and heat[8]. The term "secondary electron" refers to an electron that has been emitted from one of the orbitals of the atom that was initially struck by the incoming electron if the energy of the emitted electron is less than 50 eV. Backscattered electrons are the high-energy incident electrons that are elastically scattered and essentially possess almost the same energy as the incident or main electrons. Samples are typically imaged using either secondary electrons or backscattered electrons, with the former being more useful for displaying sample morphology and topography and the latter being more useful for displaying compositional contrasts in multiphases samples[8]. SEM pictures are extremely sensitive to topographic differences due to the low energy of the secondary electrons. The higher the atomic number of the sample material, the higher the possibility that the sample will backscatter. Although while backscattering images can't be utilized for elemental identification, they can nonetheless produce valuable contrasts between areas of the specimen that differ greatly in atomic number, Z. All of this takes place in high vacuum ($< 10^{-4}\ pa$). The production of X-rays by accelerated electrons was discussed in the XRD paragraph.

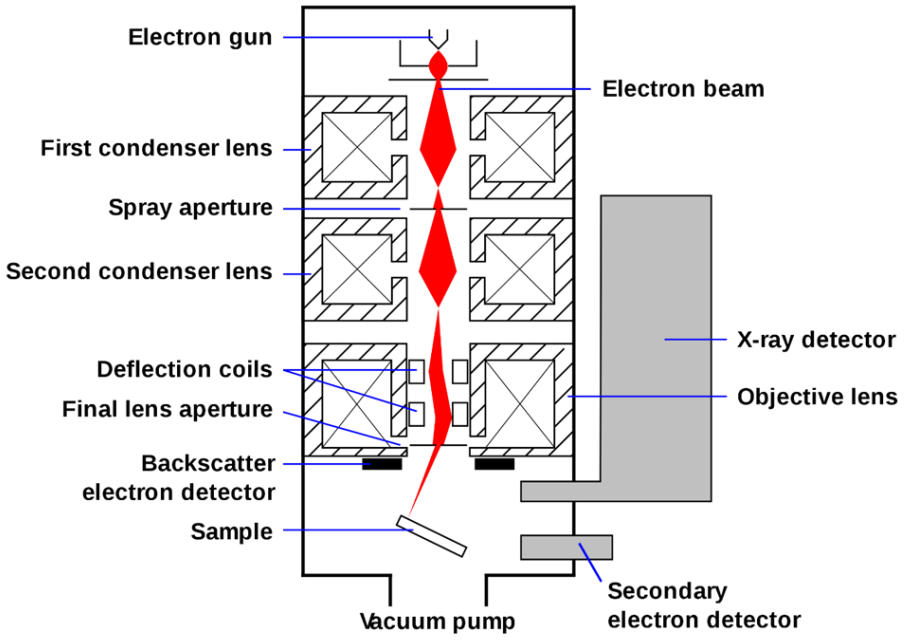

Figure 2.8 representation of the structure of a scanning electron microscope. Reprinted from [8].

The electron beam is released from an electron gun and focused by one or two condenser lenses to a diameter of around 0.4-5 nm. After being bent along the x and y axes by the electron column's deflection coils, the beam finally makes contact with the sample. Signals such as secondary electrons, back-scattered electrons, and distinctive X-rays are generated when the electron beam of a scanning electron microscope interacts with atoms at various depths within the sample. In the Scanning electron microscopy, a separate

detector is used to pick up each of these signals. Inelastic scattering of the beam electrons causes low-energy secondary electrons to be expelled from the valence or conduction bands of the sample's atoms. Electrons from the beam that are reflected through elastic scattering interactions with atoms in the sample are known as back-scattered electrons. When an electron in the inner shell is knocked out by the electron beam, a higher-energy electron can replace the void and release energy, causing the characteristic X-rays to be released. Energy-dispersive X-ray spectroscopy (EDX) measures the energy or wavelength of these X-rays to determine the amount and distribution of elements in the sample[9]. To capture Scanning electron microscopy images, the sample's surface must be electrically conductive, and it must also be grounded to prevent static electricity buildup. A conductive adhesive is used to attach samples to the specimen holder.

SEM image and EDX spectra were acquired with a Phenon Pharos from Thermo scientific. The powders were dropped on a strip of carbon tape that was attached to the sample holder and then pressurized nitrogen was used to disperse the powder on the tape. The sample was then inserted inside the chamber for the measurements.

2.3 X-ray photoelectron spectroscopy (XPS)

X-ray photoelectron spectroscopy (XPS) is a surface sensitive analytical technique, in which X-rays hit the surface of the sample and their kinetic energy is measured. The two main aspects that make it an interesting technique are its surface sensitivity and its ability to reveal chemical state information from the elements in the sample. Every element can be detected expect for hydrogen and helium. XPS is based on the photoelectric effect, according to which photons with enough energy that interact with atoms can ionize them and the kinetic energy of the emitted electrons is proportional to the energy of the photon. In XPS the sample is irradiate with X-rays with energies lower than 6 KeV (soft x-rays) and the kinetic energy of the emitted electrons is analysed[10]. When the photon interact with the atom all its energy is transferred to an electron. The energy of the photon (hv) is equal to the binding energy (BE) of the electron that describe how tightly it is bound to the atom, plus the kinetic energy (KE) of the emitted electron, plus the work function of the spectrometer (Φ_{spec}) which is a constant value[10] (figure 2.5).

$$hv = BE + KE + \Phi_{spec} \quad (1)$$

Once the kinetic energy of the electron is known the only unknown value is the binding energy: the energy of the photon is known because it's the characteristic radiation of the anode material, the work function of the spectrometer can be empirically determined. The mathematic expression can be rearranged to determine the binding energy of the emitted electrons. The photoelectrons peak are described by the element and orbital from which they were expelled. For example, considering the electrons in the orbital 1s of a carbon atom then the peak derived from this electron would be called "C 1s". Every electron that has a binding energy lower than that the photon energy can be seen from this technique. The binding energy of an electron depends on the element and it is independent of the photons energy so if the X-ray source changes the binding energy of the electrons remain the same meanwhile their kinetic energy will vary[10].

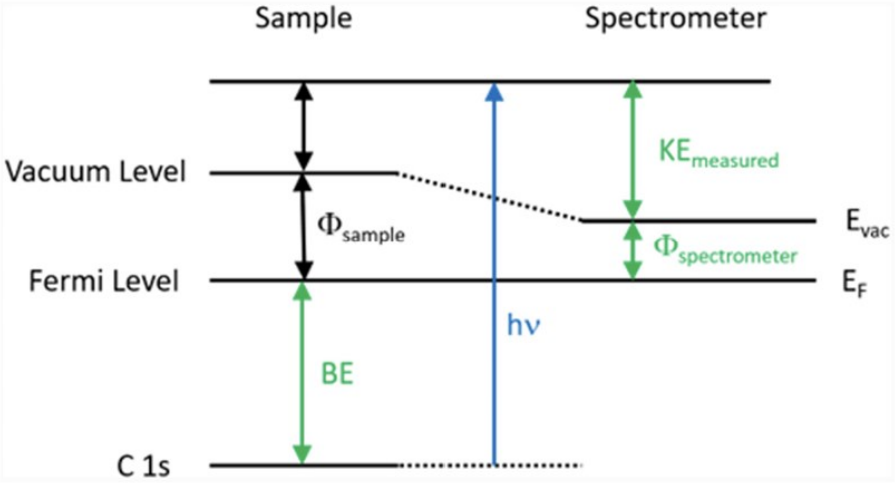

Figure 2.9 energy levels diagram describing the equation (1), hν is the energy of the photon, BE the binding energy, $KE_{measured}$ is the measured kinetic energy of the electron and $\Phi_{spectrometer}$ is the spectrometer work function. Reprinted from [10].

The emission of electrons due to the photoelectric effect leaves core "holes". In this situation the atom is in a excited ionized state that will relax by filling the hole with an electron from the valence orbital. This relaxation releases energy in one of two possible ways: x-ray fluorescence or the emission of an Auger electron (figure 2.6). X-ray fluorescence consists in the emission of a photon with energy equal to the difference in binding energy between the electron previously expelled by the x-ray beam and the electron in the valence orbital that replaces the emitted electron. Auger electrons are generated because the energy difference between the two electron described before it is not released in the form of a photon but it is transferred to an another electron of the atom that get ejected[11]. This electrons are detected by the detector. The notation of Auger peaks relies on the K, L, and M nomenclature for atomic orbitals. For example one of the aguer peaks for oxygen is denoted by KLL, which indicates that the first electron that was expelled from the x-ray beam was in the K orbital, the electron that filled the hole left from the emitted electron was from an L orbital and finally the auger electron ejected was from an L orbital[11]. The kinetic energy of the Auger electrons depends on the difference in binding energy of the atom orbitals so it is constant even if the energy of the incident photons change. Since the detector collects all the electrons emitted, auger electrons are treated like photoemitted electrons and for this reason a binding energy is calculated using equation (1). This binding energies depend on the energy of the incident photons, unlike in the case of photoemitted electrons, for this reason it's easy to identify auger peaks by changing the source because they will change position on the XPS spectrum. This is useful when spectral overlaps between Auger lines and photoelectron lines occur. Using a different x-ray source can separate those overlap.

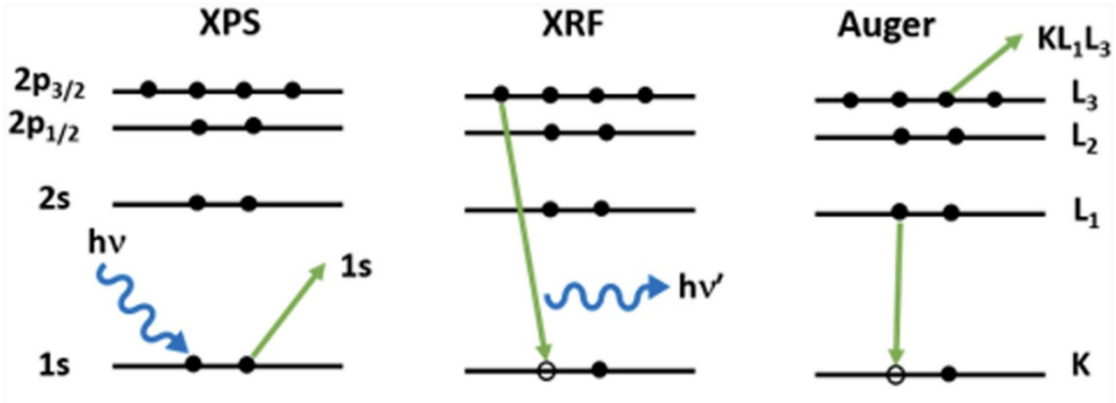

Figure 2.10 different process that result from X-ray irradiation of a surface: photoelectron emission (on the left), X-ray fluorescence (center) and emission of an Auger electron (on the right). Reprinted from [10].

An important characteristic of XPS is that it can determine the chemical environment of the atoms present in a sample. Factors like oxidation state of the element and nearest neighbors, affects the binding energy of the emitted electrons and so the position of the peaks. Considering a generic atom A, when its neighboring atoms become more electronegative they tend to attract more electron density towards them leaving the atom A with less electron density but the same positive charge in the nucleus meaning that now the effective positive charge experienced by the electrons is higher. It will be more difficult to extract the electrons of atom A and their binding energy will increase, if the X-ray source remain the same the kinetic energy will decrease and the peak will move towards higher binding energies[12]. Meanwhile for the atoms that increase their electron density by being more electronegative the opposite will occur, it will be easier to extract electrons and the peaks will move towards lower binding energies. For most transition metal the binding energy is mainly affected by their oxidation state. As described before if an atom loses electron density it will be more difficult to remove electrons and the BE will be higher. The binding energies will increase as the oxidation state increases.

All XPS lines except for the s orbital occur as doublets due to spin-orbit coupling. Usually the j quantum number is used to note this peaks. For example, the Nickel 2p doublet consists of the Ni $2p_{1/2}$ and the Ni $2p_{3/2}$ peaks figure 2.7. The intensity ratios of the peaks in a doublet are also defines by the j quantum numbers. The intensities are determined by 2j+1. For the 2p peaks the ratio of the intensity should be 2:1 for the Ni $2p_{3/2}$ and Ni $2p_{1/2}$ peaks[12]. Transition metals can exhibit an asymmetric peak shape with a tail on high binding energies. Metals have many unfilled states above the fermi level energy and valence electrons can be excited to this continuum of states. As a result a tail is seen.

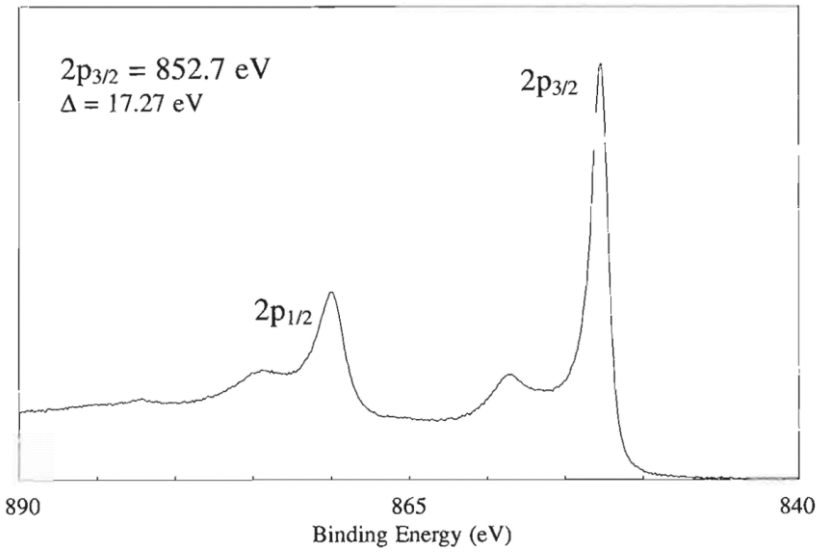

Figure 2.11 XPS region of metal nickel, reprinted from "Handbook of X-ray Photoelectorn Spectroscopy". Reprinted from [12].

XPS is a surface sensitive technique. The X-rays that irradiates the sample can penetrate up to few µm. The electrons generated by the X-photons will encounter many inelastic collisions and eventually they will lose all their kinetic energy and they will not escape the sample and reach the detector. The limiting factor for how deep in the sample this technique can reach it's the attenuation length (λ) of the photoelectron and not the penetration depth of the X-rays[10]. Photoelectron generated near the surface can incur in some inelastic collisions, they will lose energy but not enough to be trapped in the sample, so they will reach the detector with lower kinetic energy than expected. This electrons are responsible for the vertical step on the background signal after a large peak, this is visible also in figure 2.7. Only the electrons that exit the sample without inelastic collision contribute to the peak. The surface sensitivity of XPS is determined by how deep an electron can be generated and still escape without losing kinetic energy. The information depth for XPS is considered to be around 10 nm and it is defined as the maximum depth normal to the surface from which useful information is obtained. The attenuation length depend on the energy of the electron and the material through which it is traveling figure 2.8. The attenuation length is similar to the inelastic mean free path of the electrons (defined as the average distance an electron with a certain kinetic energy can travel before inelastically scattering), but the attenuation length also takes into account the effect of elastic scattering.

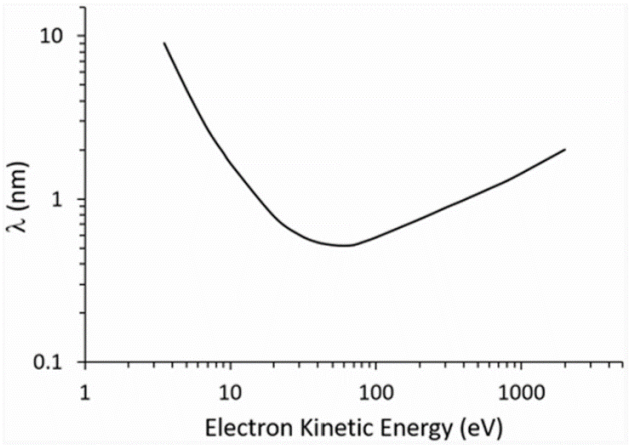

Figure 2.12 attenuation length shown as a function of electron kinetic energy. Reprinted from [11].

Insulating sample can charge during XPS measurements and this can cause peak shifting and distortions. The emission of photoelectrons and Auger electrons cause the sample to gain positive charge making more difficult to extract electrons and the binding energy of these electrons is increased causing the peak to shift towards higher BE[13]. In the case of conducting or semiconducting sample a contact is made with the sample holder and in this way the emitted electrons are replaced. Usually a charge neutralizer is used to eliminate this effect. Charge neutralizer are placed above the sample inside the vacuum chamber and they supply a flux of low energy electrons that hit the sample neutralizing the positive charge that is building up during the measurement. Usually to correct energy shift due to charging the 1s C peak is observed because every sample contains a small trace of carbon due to the fact that it was exposed to the atmosphere(adventitious carbon). The parameters of the charge neutralizer are varied until the peak of the carbon is on 285 eV and has the smallest width possible, then this parameters are kept for the rest of the easements for that sample.

The sample were prepared by depositing the powders on copper disks that were then attached to a copper sample holder using carbon tape. The copper disks were first cleaned by grinding them on sand papers of two different grit dimensions. After each grinding on the two type of paper the disks were sonicated inside a vial containing a mixture of water and isopropanol for around ten minute. At the beginning for the preparation of the samples it was chose the drop casting technique. The powders were dispersed in a mixture of isopropanol and water and then a small amount (around 2 µL) was dropped on the metal disk but during the measurements the sample charged a lot. To mitigate the charging a different deposition technique was used: the powder was directly deposited on the copper disk and pressed and distributed on the surface using a spatula, it was seen that this new technique slightly diminished the effect of charging and so it was used for every sample.

XPS measurements were acquired in a custom-made UHV system working at a pressure of $10^{-10}\ mbar$. The -ray source was a double anode (aluminum and magnesium), for the acquisition of the spectra it was used the K_α line of Mg (1253,6 eV), the acquisition system consists of an electron analyzer with five channeltrons (EA 125 Omicron). Single spectra were acquired using 0.1 eV steps, 0.25 s collection time, and 20 eV pass energy.

2.4 X-ray absorption spectroscopy (XAS)

X-ray absorption spectroscopy (XAS) (figure 2.9), which measures the X-ray absorption coefficient of a material as a function of energy, is a X-ray technique used for the determination of local geometric and/or electronic structure of matter. Its unique sensitivity to local structure, as compared to XRD, can be utilized for the study of various amorphous solids and liquid systems, including nanomaterials[14].

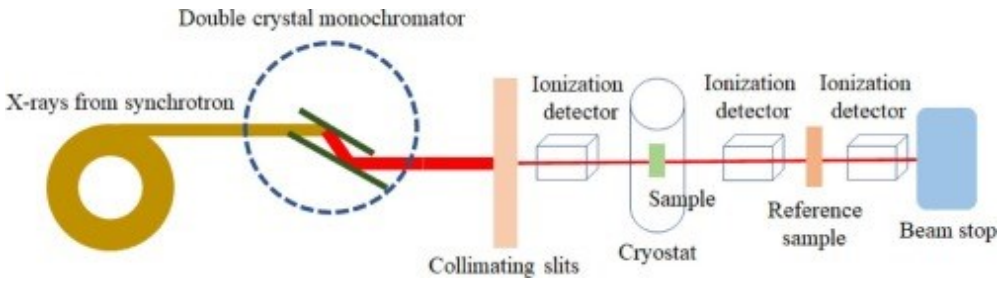

Figure 2.13 Schematic diagram of X-ray absorption spectroscopy (XAS). Reprinted from [14].

When the incident X-ray energy is high enough to excite core electron to the unoccupied sate, X-ray is strongly absorbed leading to a sharp increase in the spectrum, which is called absorption edge. Figure 2.10 represents the raw results from the absorption of a V_2O_5 powder around the Vanadium edge[15]. There is a global decrease

of absorption upon increasing energy. It corresponds to one property of X-rays which penetrate easier the matter if they have higher energy. There is an abrupt increase of absorption below 5500 eV. It corresponds to the main absorption K edge of vanadium, tabulated at 5465 eV (case 3 figure 2.10). The small peak before the main edge is called the pre-edge peak (case 2 figure 2.10) It corresponds to the transfer of the photoelectron into the first empty discrete electronic states, just above the Fermi level. It is not always observed in the XAS spectra. In few tens of eV after the edge jump, successive sharp peaks can be identified. The pre-edge peak, the main edge, and these sharp structures close to the edge are nominated X-ray absorption near edge structure (XANES). Finally, roughly 50 eV above the main edge, there is a continuous decrease of absorption containing oscillations, generally less intense that the structures of the XANES part, but very significant (case 4 in figure 2.10). These oscillations which are found in a typically 50–1000 eV range after the edge are called extended X-ray absorption fine structure (EXAFS).

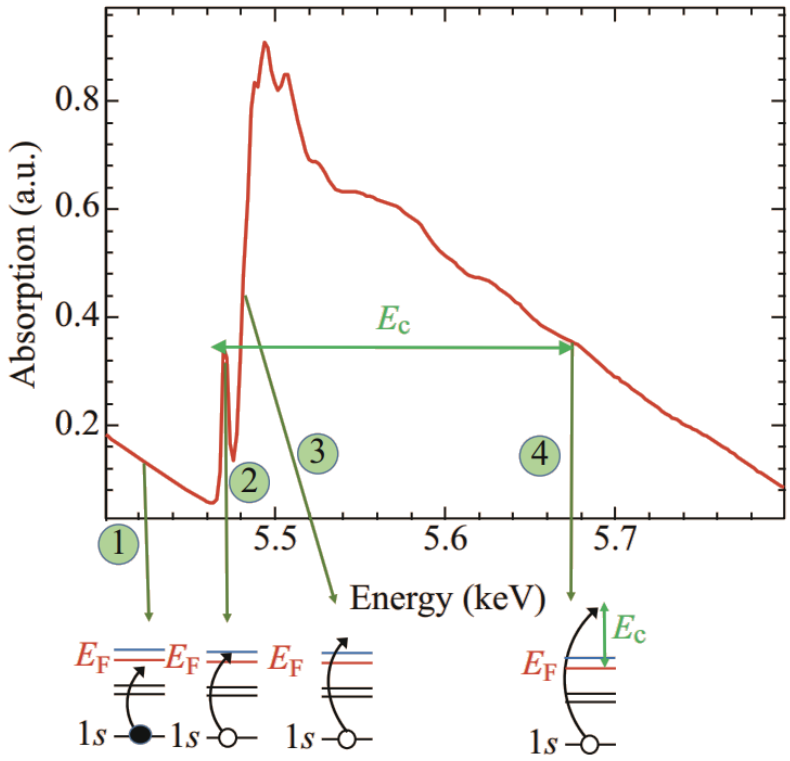

Figure 2.14 Raw vanadium edge XAS spectrum of a V_2O_5 powder. Before the edge (case 1), the electron has not gained enough energy to be extracted, there is no absorption, except by other elements or lower energy core electrons. When the first empty discrete electronic states can be reached (case 2), just above the Fermi level, absorption is possible giving an absorption peak before the main edge. Case 3 corresponds to a continuum of empty states, with the occurrence of the main absorption edge. If the energy is significantly higher than EF, the photoelectron is extracted with a kinetic energy E_c (case4). Reprinted from [15].

Close to the edge, the ejected photoelectron has a kinetic energy of few electron-volts. The mean free path can reach 1000 Å for a kinetic energy of 1 eV, and is still 50 Å for 8 eV (figure 2.8). Such lengths correspond to several interatomic distances, and the photoelectron is able to probe a large electronic cloud, which can be seen as the electronic structure of the compound. In such a long travel, the photoelectron may interact elastically with many atoms in a so-called "multiple diffusion process"[15]. The mean free path is minimum for a kinetic energy around 50 eV, and is about 5 Å. For a kinetic energy between 10 and 1000 eV, the mean free path remains around 10 Å, that is, four interatomic distances, or less. This means that in EXAFS part of the spectra the photoelectron goes out the excited atom which backscatters it to the origin atom. Only atoms at less than 5 A can be probed by the photoelectron. Therefore, EXAFS can give information only on the close environment of excited atoms[15].

2.4.1 XANES

The part of an XAS spectrum some tens of electron volts around the main absorption edge is made of several features (figure 2.10). It largely depends on the empty states of the electronic structure, which reflects itself the chemical composition and structural arrangement or molecular shape of the compound studied. The first characteristic of a XANES spectrum is the position of the main edge. Even if its tabulated, its energy may vary by some electron volts depending on the electronic population and atomic structure. The reduction of a chemical element induces a lower energy of the edge. The energy change of the edge with the oxidation state can be explained by the screening effect of electron clouds. Upon reduction the electron density increases and, by the screen effect reduces the attraction between the nucleus and 1s electron. A simple data analysis of absorption K edges allows to precisely determine the oxidation state of the absorbing element and possibly have information about its structural environment. Most of the time, it is performed by comparison with appropriate reference compounds, which is not always possible. Another major feature of the XANES spectrum is the pre-peak intensity. For the transition elements, the first empty atomic levels or orbitals are the unoccupied d states. Following the dipole selection rule, an electron transition from the 1s level to these d levels is forbidden. Nevertheless, d orbitals are a mixture between the d levels of transition element and p orbitals of ligands and adjacent transition elements. They have a more or less p contribution, depending on the environment geometry, and more precisely its Centro-symmetric character. If the absorbing atom is in a centrosymmetric environment the pre-edge peak will be absent or very small. On the other hand, if there is no center of symmetry, the pre-edge peak may be intense. As a conclusion on XANES, it can be a unique tool to obtain important information on matter. Due to its chemical element sensitivity, it may give a combination of elements to characterize the oxidation state for each constituting element. Moreover, XANES may give valuable information about the symmetry of the close environment of the absorbing atom.

2.4.2 EXAFS

Consider now the part of the XAS spectra in the approximate range of 30–1000 eV above the edge. It gives structural information which cannot be generally obtained by any other technique[15]. This is due to the short mean free path of the photoelectron which is considered as probing the environment of absorbing atom. At the end of the process, the absorbing atom has recovered its initial state with an electron filling the core hole by various ways. There are different ways to explain the EXAFS oscillations, some being based on complex theories. When the photoelectron is going out of the absorbing atom, following X-ray absorption, the associated wave is backscattered by any atom close enough from the absorbing one (figure 2.11). If the absorbing and backscattering atoms are separated by a well-defined and stable interatomic distance, we consider that the emitted and backscattered waves will combine in a rather simple way.

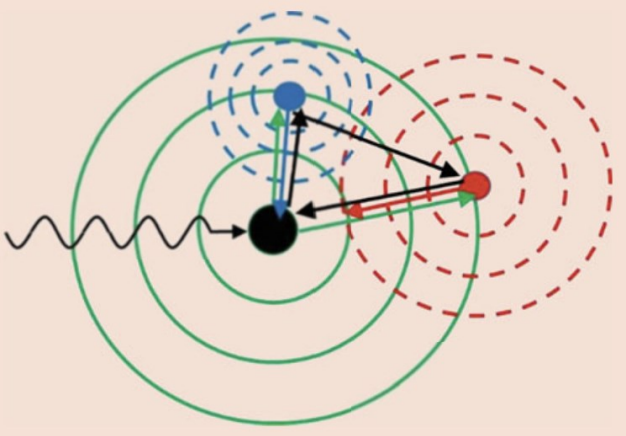

Figure 2.15 Schematic representation of the combination of the waves associated to ejected (green) and backscattered (red and blue) photoelectrons in a simple diffusion process. Black arrows represent a possible multiple diffusion process with three paths. Reprinted from [15].

In order to extract only, but all, significant oscillations above the edge, there is first a removing of the continuous decreasing background before the edge, and then a mathematical modeling of the background after the edge. The obtained EXAFS experimental signal is generally the superimposition of several different sinus functions. A direct modeling of such a signal contains too many variables and is often impossible. Therefore the following step is to apply a Fourier transform to EXAFS data. This mathematical treatment transform the data from the reciprocal space into the real space with distances expressed in Å. A series of peaks is obtained which represent a radial distribution function (RDF) of the backscattering atoms around the absorbing atom. RDF is interesting in two points. First, it is a direct representation of the interatomic distances and a simple comparison with RDF's of reference compounds give a good estimate of the true distances. At the same time, the intensities of RDF peaks are related to the coordination numbers which can be roughly estimated.

XAS measurements were recorded on beamline B18 at Diamond Light Source (UK) with ring energy of 3 GeV and a current of 300 mA. The monochromator used was Si(311) crystals operating in Quick EXAFS (QEXAFS) mode. Pellets of $Ni(OH)_2$, 8Mn-$Ni(OH)_2$ and 8Mo-$Ni(OH)_2$, and the oxides used as references, were measured in transmission mode at the Ni K (8333 eV), Mn K (6539 eV), and Mo K (20000 eV) absorption edges at 298 K using a 36-element Ge detector. The corresponding metal foils were measured simultaneously. Calibration of the monochromator was carried out using the foil previously to the measurements. The acquired data were processed using the Athena program.

2.5 Electrochemical characterization

The electrochemical characterization of all the samples was carried out in a three-electrode electrochemical cell. A mercury-mercury oxide electrode (MOE) was used as reference electrode, while a graphite rod was used as counter electrode. The electrolyte solution used was a 1M KOH solution (pH=14). To avoid contamination of any kind, the set up was always washed with milli-q water before each measurement and after the measure was done the cell and counter electrodes were sonicated in a sulfuric acid solution and then in water. Before the measurements, nitrogen gas was bubbled inside the cell to obtain an inert atmosphere, and during the measurement the nitrogen gas was kept flowing. Measurements were done without magnetic agitation and at room temperature. The working electrode was obtained by drop-casting 7µL of an ink on a glassy carbon electrode (3mm diameter). The glassy carbon electrodes were always cleaned with a polishing kit, first by using a polishing paste of 1µm and then, after sonicating the electrode in water

and isopropanol, it was used a ¼ µm polishing paste. The catalyst inks were prepared by adding 2mg of hydroxide in 1mL of solution (60% isopropanol and 40% water) and 11,44 µL of 20% Nafion solution. Finally, the ink was sonicated for 30 minutes. The main problem with the ink was that the powder did not disperse very well. This problem was attributed to the large dimension of the particles. For this reason, samples were grinded by ball milling. Ball milling is a technique that consists in centrifugating a jar containing small balls and the powder, the balls move inside the jar and crush the powder into smaller particles. In this case the jar and the balls were made of alumina and for each sample a rotation speed of 360 rpm for 30 minutes were used. Different solvents and different ratios were studied to obtained the best dispersion. Using the 5% Mn doped hydroxide, 6 different inks were prepared: isopropanol/water 80:20, 60:40, 40:60 and ethanol/water 80:20, 60:40, 40:60. These six different inks were used to coat six different glassy carbons by drop-casting and then they were analyzed with an optical microscope to find out which composition gave the best results. For some of the solution, It was possible to see the precipitated solid at the bottom of the vial and this was an undesired result because this meant that the solution was less concentrated than desired. This was not the case for some of the ratios such as 60:40 isopropanol/water, 80:20 isopropanol/water and 60:40 ethanol/water. Most of the deposition resulted in the formation of a "coffee ring" meaning that most of the material deposited on the sides meanwhile in the center there was only a small fraction. The only ink composition that showed an homogenous deposition on the glassy carbon was the 60:40 isopropanol/water and, for this reason, it was chosen as the composition for all the depositions.

All the samples were used as catalysts for the UOR reaction. After 20 minutes of degassing with nitrogen, the catalysts were activated by performing 200 cycles at 200mV/s from 0V to 0.8V Vs MOE. For all the different materials, a stable CV was obtained after 200 cycles. After the activation, 0.991 g of urea were added in 50 mL of 1M KOH solution to obtain a concentration of 0.33M, which is the concentration of urea in urine. The current was corrected for the solution ohmic drop for every measurement.

The nickel phosphides samples were also used as hydrogen evolution reaction catalysts. In this case, after 20 minutes of continuous nitrogen flow, catalysts were activate by performing 200 cycles from 0 V to -0.6 V Vs RHE. After the activation, LSVs measurements were taken in 1M KOH solution.

2.5.1 Electrochemical surface area (ECSA)

All the current values were normalized. Different techniques can be used to obtain the electroactive area of the electrode. The geometric area of the electrode it is easy to calculate since it is known that the diameter of the glassy carbon is 3 mm so the exposed area is 0,0707 cm^2. This value can be used for the normalization of the current but it does not consider the fact that every deposition is different and the real exposed area could be different even for two different deposition of the same sample. Since the current values of different sample are divided by the same number (geometric area), it is difficult to assess the activity of the different materials because higher currents may just be due to a higher active area and not to the intrinsic characteristics of that material. Knowing the ECSA (electrochemical active surface area) will allow for a more accurate performance comparison between different materials[16]. For some materials, it can be straightforward. For example, platinum where the active area can be obtained by measuring the charge associated to one monolayer of hydrogen desorption in a CV[17]. Due to the complexity of nickel electrochemistry, assumptions and estimations are needed when trying to estimate the active surface area[16]. McCr et al.[18] used a method based on electrochemical double layer to calculate the ECSA. CVs at different scan rates were run in a potential range in which no Faradic process occurred. This range was typically 100 mV potential window centered at the open-circuit potential of the system. All the current measured is

assumed to be due to the double-layer charging. The double layer capacitance was obtained from the slope of the charging current vs the scan rate. The ECSA is obtained by dividing the double layer capacitance by a specific capacitance value of 40 µF cm^{-2}. In this work, this method was carried out by running a series of CVs at different scan rates (5, 10, 20, 50, 100, 200, 300, 400 mVs^{-1}) in a range of $\pm$ 50 mV around the OCP. With the data, it was possible to calculate the charging current I_c of the electrodes at each scan rates.

$$I_c(A) = (I_{anodic} - I_{cathodic})_{OCP}$$

It was then possible to obtain a double layer capacitance value C_{dl}, by calculating the slope of the graph obtained by plotting the charging current vs. scan rate. Finally the ECSA was calculated by dividing the C_{dl} by the specific charge density (40 µF cm^{-2}). In table 2.1, the values of ECSA obtained with this method are reported, and in figure 2.12, the CVs at different scan rates mentioned before are shown.

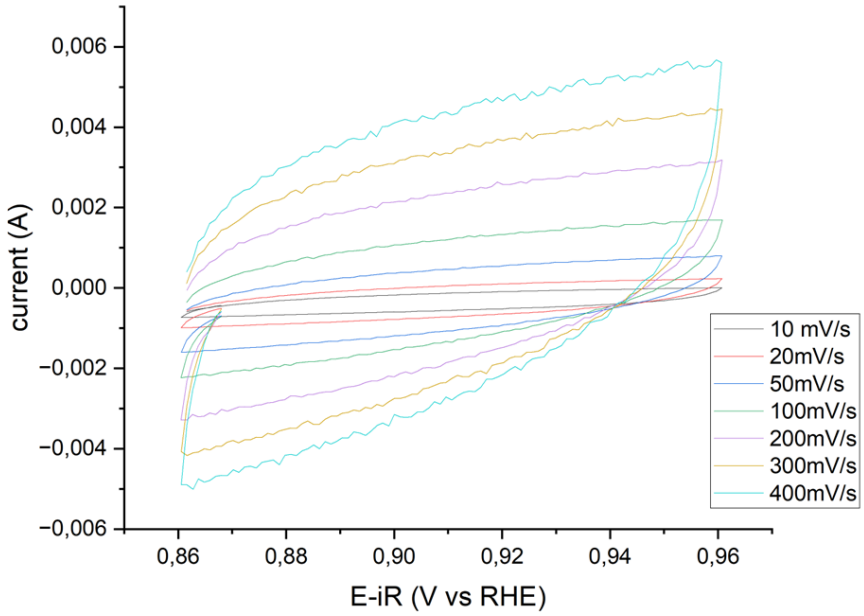

Figure 2.12 CVs at different scan rate, for sample 4

Table 2.1 ECSA values of all the samples obtained with the double layer method

sample	ECSA (cm^2)
$Ni(OH)_2$	0.29
3Mn-$Ni(OH)_2$	0.38
5Mn-$Ni(OH)_2$	0.27
8Mn-$Ni(OH)_2$	0.42
8Mo-$Ni(OH)_2$	0.32
20Mo-$Ni(OH)_2$	0.30
30Mo-$Ni(OH)_2$	0.28

As expected, all the ECSA values far exceed the geometric area of the electrode, since the latter does not consider that the deposited material can have a peculiar morphology that can expose more surface. Since the main active species for UOR are the high valence state of Ni species, a more accurate approach for the ECSA calculation can be done by evaluating the redox peak of the Ni species[19]. This method consists of integrating

the NiOOH reduction peak (figure 2.13). For every sample, before introducing the urea in the electrolyte, a CV from 0 to 0,75 V Vs MOE was run. For the ECSA calculation the following formula was used:

$$ECSA = \frac{Q}{0{,}257}$$

Where Q is the charge corresponding to the reduction peak Ni(III)/Ni(II)[20]. 0,257 mC was the charge associated with the formation of the monolayer of nickel (II)

$$Q = \frac{S}{\nu}$$

In which S is the peak area and ν is the scan rate. The scan rate was 0,02 V/s for every sample and the peak was integrated over a 400 mV window: from 0,54 to 0,14 V Vs MOE (1,45 to 1,05 V Vs RHE).

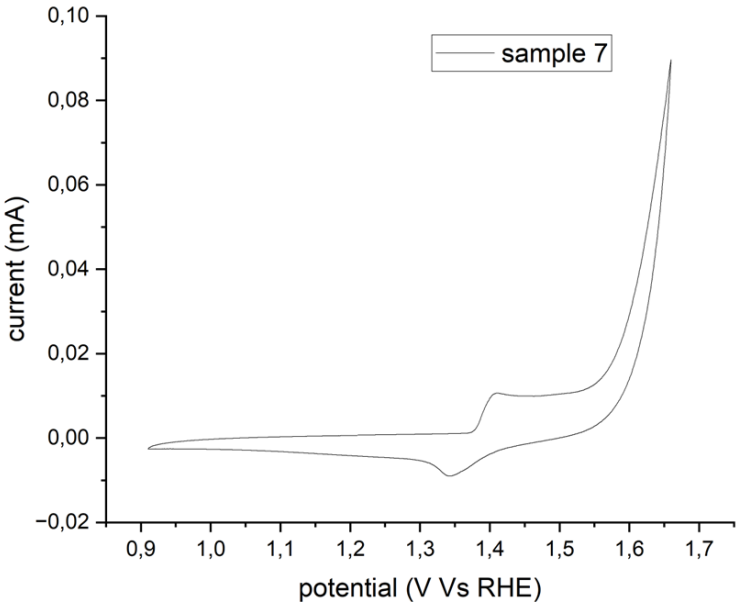

Figure 2.13 CV without urea in 1M KOH with sample 7 as catalyst

For the calculation of the current density, the value obtained by the second method was used because, as mentioned before, this value is strongly correlated to the quantity of active nickel sites that are the sites where urea oxidation occurs. The values reported in table 2.2 are significatively different than the values calculated with the capacitance method, this is due to the fact that with the reduction peak method only the surface occupied by the real active sites (the high valence state of Ni species) is considered.

Table 2.2 ECSA values of all the samples obtained with the reduction peak method

sample	ECSA (cm^2)	sample	ECSA (cm^2)
$Ni(OH)_2$	1.74	NiP	0.87
3Mn-$Ni(OH)_2$	1.35	3Mn-NiP	1.21
5Mn-$Ni(OH)_2$	1.39	5Mn-NiP	0.57
8Mn-$Ni(OH)_2$	0.48	8Mn-NiP	0.34
8Mo-$Ni(OH)_2$	1.11	8Mo-NiP	0.98
20Mo-$Ni(OH)_2$	1.23	20Mo-NiP	0.35
30Mo-$Ni(OH)_2$	0.32	30Mo-NiP	1.13

2.6 Setup for the nickel phosphides synthesis

The synthesis were done using a tubular oven (figure 2.14) in which the nickel hydroxides samples and the phosphorus precursor were inserted. The phosphorus precursor decomposes in phosphine, which is the agent that reacts with the hydroxides. Phosphine is dangerous and may cause respiratory irritation and compromise cardiac functions. The oven is connected to a tube system that pumps nitrogen gas inside that acts as a gas carrier. The apparatus was realized in order to detect eventual leaks in the system thanks to the presence of a mass flow controller that can be used to regulate the flow of the gas and three valves in different points of the system, one before the oven, one after the first bubbler, and one after the second bubbler. First, the sample was put inside the oven in the center and the precursor at around 7 cm from the center. Before the start of each synthesis the gas was let to flow inside the oven and then each valve was closed one by one and it was verified that the mass flow controller registered a decrease in gas flow if the value was constant it meant that there was a leak that let the gas flow. After it was made sure that no leaks were present the nitrogen gas was let to flow inside the tube at 500 Standard Cubic centimeters per Minutes (SCCM) for around ten minutes to make sure that no oxygen was left inside the apparatus and that only nitrogen was present. The temperature of the oven was set at 300°C. this is the temperature at the center of the oven, meanwhile the temperature decreases going away from the center. Having no means to accurately measure the temperature at different distances from the center, some tests were done using only the precursor at different distances and it was found that at around seven centimeters from the center all of the precursor reacted and turned red so this distance was kept.

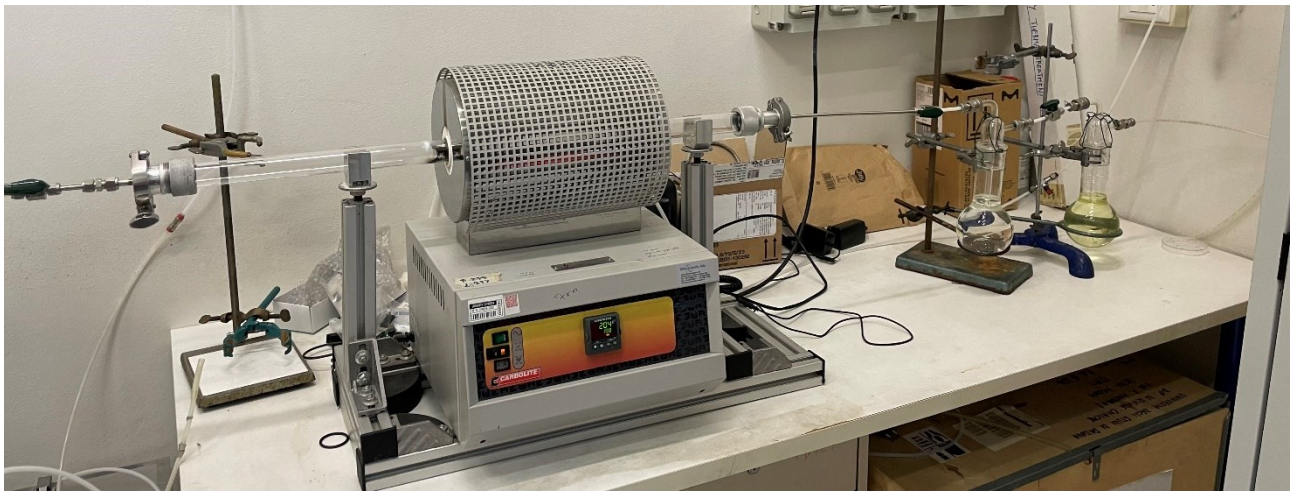

Figure 2.14 Oven set-up used for the synthesis of the nickel-phosphide based samples.

Bibliography

1. Ameh, E. S. A review of basic crystallography and x-ray diffraction applications. *Int J Adv Manuf Technol* **105**, 3289–3302 (2019).
2. Quinn, P. S. & Benzonelli, A. XRD and Materials Analysis. in *The Encyclopedia of Archaeological Sciences* (ed. López Varela, S. L.) 1–5 (Wiley, 2018). doi:10.1002/9781119188230.saseas0619.
3. Kacher, J., Landon, C., Adams, B. L. & Fullwood, D. Bragg's Law diffraction simulations for electron backscatter diffraction analysis. *Ultramicroscopy* **109**, 1148–1156 (2009).
4. Ali, A., Chiang, Y. W. & Santos, R. M. X-ray Diffraction Techniques for Mineral Characterization: A Review for Engineers of the Fundamentals, Applications, and Research Directions. *Minerals* **12**, 205 (2022).
5. Fatimah, S., Ragadhita, R., Husaeni, D. F. A. & Nandiyanto, A. B. D. How to Calculate Crystallite Size from X-Ray Diffraction (XRD) using Scherrer Method. *ASEAN J. Sci. Eng.* **2**, 65–76 (2021).
6. Whittig, L. D. & Allardice, W. R. X-Ray Diffraction Techniques. in *SSSA Book Series* (ed. Klute, A.) 331–362 (Soil Science Society of America, American Society of Agronomy, Madison, WI, USA, 2018). doi:10.2136/sssabookser5.1.2ed.c12.
7. Anburajan, M. & Sharma, J. K. "Overview of X-Ray Tube Technology". in *Biomedical Engineering and its Applications in Healthcare* (ed. Paul, S.) 519–547 (Springer Singapore, Singapore, 2019). doi:10.1007/978-981-13-3705-5_21.
8. Mohammed, A. & Abdullah, A. SCANNING ELECTRON MICROSCOPY (SEM): A REVIEW.
9. Cardell, C. & Guerra, I. An overview of emerging hyphenated SEM-EDX and Raman spectroscopy systems: Applications in life, environmental and materials sciences. *TrAC Trends in Analytical Chemistry* **77**, 156–166 (2016).
10. Krishna, D. N. G. & Philip, J. Review on surface-characterization applications of X-ray photoelectron spectroscopy (XPS): Recent developments and challenges. *Applied Surface Science Advances* **12**, 100332 (2022).
11. Kassis, A. I. The Amazing World of Auger Electrons. *International Journal of Radiation Biology* **80**, 789–803 (2004).
12. Grosvenor, A. P., Biesinger, M. C., Smart, R. St. C. & McIntyre, N. S. New interpretations of XPS spectra of nickel metal and oxides. *Surface Science* **600**, 1771–1779 (2006).
13. Cazaux, J. About the charge compensation of insulating samples in XPS. *Journal of Electron Spectroscopy and Related Phenomena* **113**, 15–33 (2000).
14. Sarker, S. D. & Nahar, L. Characterization of nanoparticles. in *Advances in Nanotechnology-Based Drug Delivery Systems* 45–82 (Elsevier, 2022). doi:10.1016/B978-0-323-88450-1.00011-9.
15. Ouvrard, G. & Jobic, S. X-Ray Absorption Spectroscopy (XAS). in *Springer Handbook of Inorganic Photochemistry* (eds. Bahnemann, D. & Patrocinio, A. O. T.) 273–302 (Springer International Publishing, Cham, 2022). doi:10.1007/978-3-030-63713-2_11.
16. Cossar, E., Houache, M. S. E., Zhang, Z. & Baranova, E. A. Comparison of electrochemical active surface area methods for various nickel nanostructures. *Journal of Electroanalytical Chemistry* **870**, 114246 (2020).
17. Ntais, S. *et al.* Promotion of Ammonia Electrooxidation on Pt nanoparticles by Nickel Oxide Support. *Electrochimica Acta* **222**, 1455–1463 (2016).
18. McCrory, C. C. L., Jung, S., Peters, J. C. & Jaramillo, T. F. Benchmarking Heterogeneous Electrocatalysts for the Oxygen Evolution Reaction. *J. Am. Chem. Soc.* **135**, 16977–16987 (2013).
19. Hall, D. S., Lockwood, D. J., Bock, C. & MacDougall, B. R. Nickel hydroxides and related materials: a review of their structures, synthesis and properties. *Proc. R. Soc. A.* **471**, 20140792 (2015).
20. Yang, D. *et al.* Nanostructured Ni_2 P-C as an Efficient Catalyst for Urea Electrooxidation. *ChemElectroChem* **5**, 659–664 (2018).

CHAPTER 3

Synthesis and characterization of nickel hydroxide-based catalysts for the urea oxidation reaction

3.1 Introduction

The urea-assisted water splitting comprises the oxidation of urea (UOR) at the anode side and the hydrogen evolution reaction (HER) at the cathode one.[1,2] Compared to HER, UOR faces the hindrance of slow reaction kinetics because of the $6e^-$ transfer process. For this reason, highly efficient catalysts are needed.[3] Noble metal catalysts, such as Pt or Ru, are valid options but, as mentioned in Chapter 1, they are expensive and rare. On the other hand, transition metal-based electrocatalysts are economically more convenient and show good activity for UOR. In particular, Ni-based catalysts, such as nickel oxides, hydroxides, chalcogenides, etc. are the most interesting ones[4–6] due to their earth abundance, high stability in the strong alkaline media, and the facile active phase formation resulting from the multivalent oxidation states.[7] Botte and coworkers found that the noble metal-based catalysts, such as Pt, Rh, Ir and intermetallic PtIr, have a lower electrocatalytic activity toward UOR, respect to Ni-based materials.[8] Spinel-type binary metal oxides and perovskites are other two candidates as UOR catalysts thanks to their rich redox chemistry, high electronic conductivities and low cost.[9,10] For this class of materials, it was reported that the best performing catalysts contain elements such as lanthanum, which is a rare-earth element,[11] making it much more expensive than nickel oxides or nickel hydroxides-based materials. Incorporation of trace elements into the raw catalyst presents an alternative and effective strategy for enhancing the catalytic properties of UOR catalyts. This enhancement is achieved through the tailoring of the nickel electronic structure, which is modified by the introduction of metal or non-metal elements. The resultant strong interactions between the dopant and active sites result in a synergistic effect that could optimize the adsorption and desorption energy of the intermediates. Consequently, this optimization boosts the charge transfer process and intrinsic catalytic activity toward the oxidation reaction. It is noteworthy that the electronegativity of different doping elements also affects the electronic state of the electrocatalysts.[12] Doping should influence the catalytic performance by the electronic effect, due to the change of the chemical environment. This effect consists in an electron density shift and electronic structure reconfiguration that occurs in heterogenous materials such as alloys, central atom and ligand, and components with different electronegativity.[13] Doping can also introduce defects that can disturb the routine arrangement of the crystal lattice and results in the redistribution of atoms and electrons.[14] In cobalt-doped nickel hydroxide, it was found that the charge density distribution around Ni atoms was disturbed by increasing the Co concentration, and more charge accumulation was aligned with Ni-OH bond.[15] The presence of Co in the system altered the electronic state of Ni 3d.

Molybdenum doping was investigated since this element is more electronegative than nickel, while manganese-doping was investigated since this element is less electronegative than nickel. In the literature, there are several works[16–18] in which the molybdenum content in the samples is much higher than standard doping values. For this reason, and also to understand if the higher amount of foreign atoms could have a

different effect on the performance of the catalysts, it was chosen to synthesize samples with high molybdenum content. In this way, seven different catalysts were synthesized, which are listed in table 3.1: pure nickel hydroxide, three manganese-modified nickel hydroxide with different concentrations (3 at.%, 5 at.%, and 8 at.% Mn), and three molybdenum-modified nickel hydroxide with different concentrations (7 at.%, 20 at.%, and 30 at.% Mo).

Table 3.1 List and nomenclature of the different $Ni(OH)_2$-based materials synthesized.

Name	Dopant	Nominal at.% M content (M=Mn,Mo)
$Ni(OH)_2$	---	---
3Mn-$Ni(OH)_2$	Mn	3
5Mn-$Ni(OH)_2$	Mn	5
8Mn-$Ni(OH)_2$	Mn	8
8Mo-$Ni(OH)_2$	Mo	8
20Mo-$Ni(OH)_2$	Mo	20
30Mo-$Ni(OH)_2$	Mo	30

3.2 Synthesis

The synthesis of the nickel hydroxide samples was done in collaboration with the company Circular Materials S.r.l. (https://circularmaterials.it), which is specialized in retrieving metals from waste waters. The final goal of the project, in which this thesis work is inserted, is the obtention of $Ni(OH)_2$-based materials from wastewater containing nickel. By obtaining the catalytic material in this way it would be possible to obtain a cheap catalyst without the need to extract nickel from mines and, at the same time, purify polluted water. However, in this work, the synthesis was carried out in the laboratory starting from commercial nickel, molybdenum and manganese precursors. The patented synthesis system used is based on the mixing of the waste waters (in this case a solution containing the metal precursors) with supercritical water (T> 374°C and P > 221 bar) in a mixer, where the instant precipitation process takes place: the metals in solution behave like in an a-polar medium and nucleation sites start to form that then grow until they become nano- and microparticles, figure 3.1. The extreme reduction of the dielectric constant of water in supercritical conditions (from 77 to 2) is what drives the precipitation of metals in form of fine powder. The type of material (oxide, hydroxide or metal) obtained depends on the pH that can be easily tuned by modifying the concentration of the NaOH solution added inside the mixer. First, some tests were run to identify the best nickel precursor and the best conditions (temperature and pH). It was found that between nickel acetate $Ni(CH_3CO_2)_2$ and nickel nitrate $Ni(NO_3)_2$, the former granted the best yield. For every test, 0.5L of a 0.3M precursor solution was prepared and then, the temperature was changed by modifying the hot water flow. The three temperature values were: 230°C, 270°C and 330°C. The middle value (270°C) was the one that granted the best yield meanwhile the pH did not affect much the results. The pH was measured after the treatment by using a benchtop pH-meter. To change the pH, the concentration of the NaOH solution added in the mixer was changed. It was found that a 1M solution (pH=13) gave the best results. After these tests, it was decided to use the same conditions also for the synthesis of the doped hydroxides. Manganese acetate ($Mn(CH_3CO_2)_2$) and sodium molybdate (Na_2MoO_4) were used as manganese and molybdenum precursors, respectively. As an example, the synthesis of the 3 at.% Mn-doped nickel hydroxide is described. 0.5 L of a 0.3M nickel acetate

solution (0.15 mol) was prepared. Then, 1.10 g (0.0045 mol) of manganese acetate were added. After the synthesis, a solution containing nickel hydroxide and some traces of metal ions that did not precipitate is obtained. Therefore, this solution was centrifuged to obtain the final material and eliminate the supernatant liquid. The slime was dried in an oven at 105°C overnight and, finally, the solid grains were crushed into a fine powder. The same process was repeated for the synthesis of molybdenum-modified hydroxides but it was noticed that the yield was reduced and most of the molybdenum ions were still in the supernatant liquid. This was obvious because the liquid was colored meanwhile for the other synthesis the liquid was colorless. XRF measurements confirmed that the concentration of molybdenum in the supernatant liquid was very similar to the concentration in the precursor solution. To solve this problem, the pH was reduced by decreasing the concentration of the NaOH solution from 1M to 0.4M (final solution pH=8). The success of the synthesis using the new pH was confirmed by XRF. The synthesis conditions of the seven samples are reported in Table 3.2.

Table 3.2 different parameters used in the synthesis of the six doped samples.

sample	Nickel acetate (g)	Dopant precursor (manganese acetate/ sodium molybdate) (g)	NaOH concentration (M)	Temperature (°C)	Time (minutes)
3Mn-$Ni(OH)_2$	37.3	1.1	1	270	20
5Mn-$Ni(OH)_2$	37.3	1.8	1	270	20
8Mn-$Ni(OH)_2$	37.3	2.9	1	270	20
8Mo-$Ni(OH)_2$	37.3	2.9	0.4	270	20
20Mo-$Ni(OH)_2$	37.3	7.3	0.4	270	20
30Mo-$Ni(OH)_2$	37.3	10.9	0.4	270	20

As mentioned above, the EDX and XRF measurements were fundamental to determine the pH conditions in the synthesis of the molybdenum-modified samples to get all, or at least most of, the molybdenum ions to precipitate together with the nickel ions.

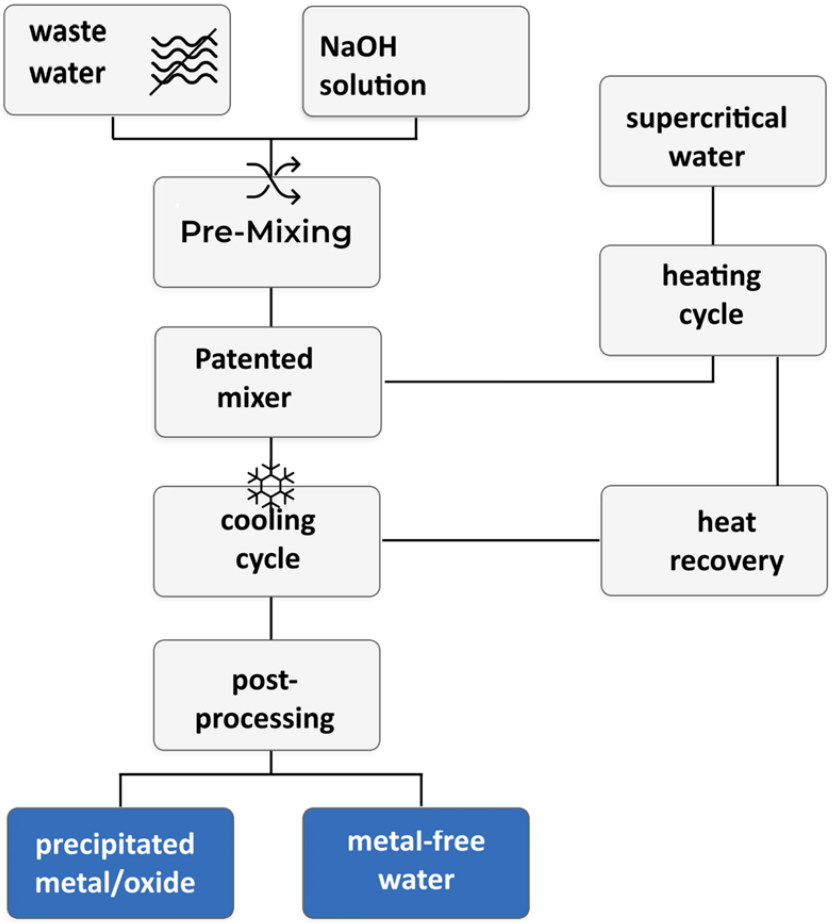

Figure 3.1 schematic representation of the system used for the synthesis of hydroxides. Reprinted from https://circularmaterials.it

3.3 Physico-chemical characterization

The synthetized hydroxides were characterized by using X-ray diffraction (XRD), X-ray photoelectron spectroscopy (XPS), inductively coupled plasma spectroscopy (ICP), scanning electron microscopy (SEM) and X-ray adsorption (XAS). These techniques as well as the measurements conditions were described in Chapter 2.

3.3.1 Mn-doped hydroxides

The morphology of the synthetized hydroxides was investigated by scanning electron microscopy (SEM). The images reported in Figure 3.2. evidence the presence of particles with a wide range of dimensions and with no specific shape. The particles went from hundreds of nanometers to hundreds of micrometers. Most of the particles were around tens of micrometers but in every sample at least a big particle with dimensions over 100 micrometers was found. To evaluate the elemental composition of the particles, and to verify the absence of contaminants, EDX analysis was performed.

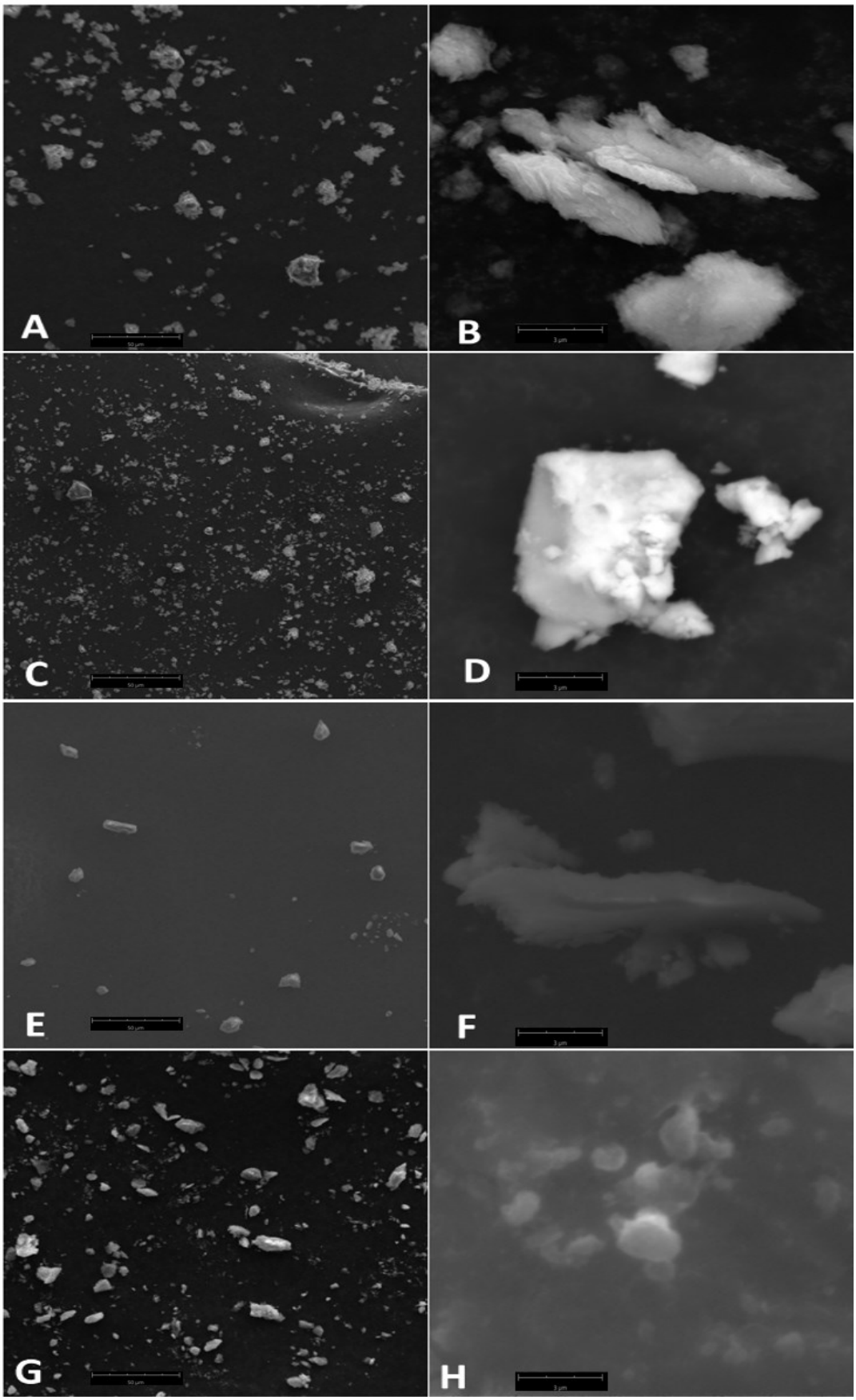

Figure 3.2 SEM images of $Ni(OH)_2$ (A and B), 3Mn-$Ni(OH)_2$ (C and D), 5Mn-$Ni(OH)_2$ (E and F), and 8Mn-$Ni(OH)_2$ (G and H). the scale bar of the left images is 50 µm, while the one of the right images is 3 µm.

The synthesis route described above allows to produce large quantities of material in a short time. Starting from the precursor's quantities reported in Table 3.2, around 10 g of catalyst were obtained in about 20 min. Therefore, compared to more traditional techniques like hydrothermal synthesis, this one is cost effective (it is possible to start from wastewater), and it can be scaled up to obtain a large scale production. The main problem of this technique is visible in figure 3.2: it is difficult to obtain small particles and control the morphology, as can be done with other different techniques like the hydrothermal synthesis.[19,20] This problem is mainly due to the high quantity of material precipitated and the speed of the process. In our case, high temperature and pressure are reached like in the hydrothermal route, but there is a much higher precursor content and the process is much faster. Usually, in the hydrothermal synthesis, the process can last more than 24 hours and a few mg of material are obtained, while with the Circular Materials' technique the synthesis last around 20 minutes and tens of grams of material are obtained. During this quick synthesis, nucleation sites start to form and grow but, since this happens in the span of some minutes, it is impossible to control the particle dimension and, for this reason, a wide range of dimensions is obtained.

The presence of manganese in the precursor solution did not affect the morphology of the particles. Also in this case, the samples did not have a specific morphology, and a wide range of dimensions was obtained.

EDX measurements were done to determine the composition of the samples and the metals ratio. These measurements were fundamental to find out the best conditions for the synthesis of modified hydroxides. The measurements were taken from different spots of the sample: at least three images were taken for every sample and from them at least three spots were measured by EDX.

Table 3.3 atomic concentration of Ni, O and Mn obtained from EDX measurements. The Mn:Ni ratio is also reported.

Sample	Ni (at.%)	O (at.%)	Mn (at.%)	Atomic Mn:Ni ratio[a]	Atomic Mn:Ni ratio [b]
$Ni(OH)_2$	20.6	79.4	/	/	/
3Mn-$Ni(OH)_2$	18.4	81.1	0.5	2.9	2.7
5Mn-$Ni(OH)_2$	17.5	81.7	0.8	4.3	4.4
8Mn-$Ni(OH)_2$	16.2	82.6	1.2	7.5	8.1

a: values obtained by EDX measurements.
b: values obtained by ICP measurements

Table 3.3 reports the atomic composition obtained by EDX measurements as well as the Mn:Ni ratio. No contaminations were found. In some cases, the EDX showed the presence of carbon, which is attributed to the fact that the samples were deposited on carbon tape and also that they were exposed to the atmosphere. Thanks to ICP measurements it was possible to obtain a more accurate value of the dopant concentration in the sample, since the accuracy of this teacnique is much higher than the one of the EDX. The value obtained describe the total amount of manganese in the sample so even the manganese atoms that were not incorporated into the $Ni(OH)_2$ structure are counted in this measurement. The values obtianed from ICP are very close to the nominal value. In the case of the 8Mn-$Ni(OH)_2$ sample, the experimental value is slightly higher than the nominal one, suggesting that not all the nickel precipitated from the solution leaving an excess of manganese.

The powders were analyzed by X-ray diffraction to determine the different phases present in the sample. There are two known pseudopolymorphs of $Ni(OH)_2$, denoted as α- and β-$Ni(OH)_2$.[21] The β-phase material occurs naturally as the mineral theophrastite and it has trigonal symmetry (Figure 3.3). The α-$Ni(OH)_2$ ·

xH_2O polymorph of nickel hydroxide consists of layers of β-$Ni(OH)_2$ oriented parallel to the crystallographic ab-plane, intercalated by water molecules (Figure 3.4).[22]

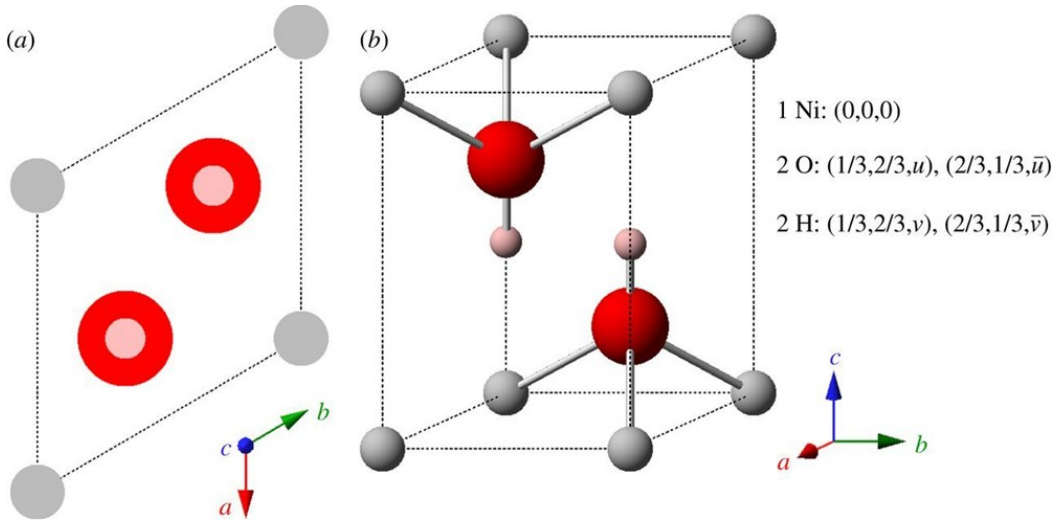

Figure 3.3 The crystal structure of β-$Ni(OH)_2$ represented by (a) unit cell projection and (b) ball-and-stick unit cell. Reprinted from citation 16

The intercalated water molecules do not occupy fixed sites, but rather they have some freedom to rotate and translate within the ab-plane. Water acts as an "amorphous glue" that holds together the $Ni(OH)_2$ layers.[23] As a result, adjacent layers have little, or not, tendency to orient relatively to one another. This random layer orientation motif is known as a "turbostratic" structure.[21] In addition to the two fundamental phases of nickel hydroxide, there are several possible types of structural disorder, including the incorporation of foreign ions, variable hydration and crystal defects including stacking faults.[24] The effects of structural disorder can have very important practical consequences. For example, well crystallized β-$Ni(OH)_2$ has lower electrochemical activity than disordered β-$Ni(OH)_2$ materials.[25]

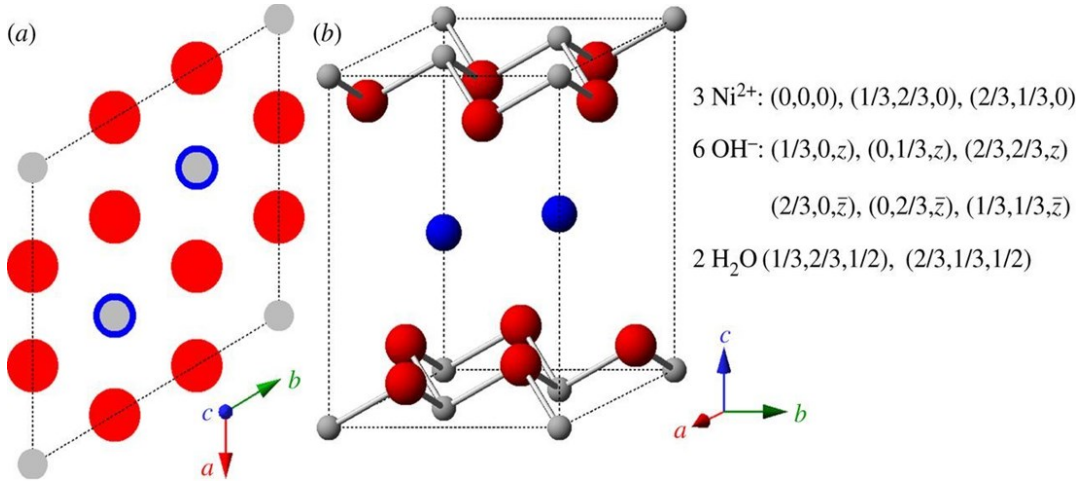

Figure 3.4 The idealized crystal structure of α-$Ni(OH)_2 \cdot xH_2O$ rapreseted by (a) unit cell projection and (b) ball-and-stick unit cell. Reprinted from citation 16

Stacking faults, which are common in layered double hydroxides, may be understood by examining the unit cell of β-$Ni(OH)_2$. There is strong ionic bonding between Ni^{2+}, O^{2-} and H^+ ions within each $Ni(OH)_2$ sheet, whereas the interactions between adjacent layers are relatively weak.[23] Therefore, $Ni(OH)_2$ materials consist of several "stacked" layers. Stacking faults cause selective line broadening in XRD patterns, because the

disorder is only along the direction of the crystallographic c-axis.[26] To identify which of the two phases was present in the samples, the XRD spectra were confronted with data from a database by using the software Highscore plus. The main peaks for the α and β phases are reported in table 3.4 .

Table 3.4 X-ray diffraction parameters of α-$Ni(OH)_2$ and β-$Ni(OH)_2$. Values obtained from high score plus software.

α-phase		β-phase	
Miller indices (hkl)	2θ (°)	Miller indices (hkl)	2θ (°)
(001)	12.8	(001)	19.3
(100)	22.3	(100)	33.1
(002)	25.8	(101)	38.6
(110)	39.2	(012)	52.1
(111)	41.4	(110)	59.1
(200)	45.6	(111)	62.8
(004)	53.1	(200)	69.4
(210)	61.6	(103)	70.4
(301)	72.5	(201)	72.8

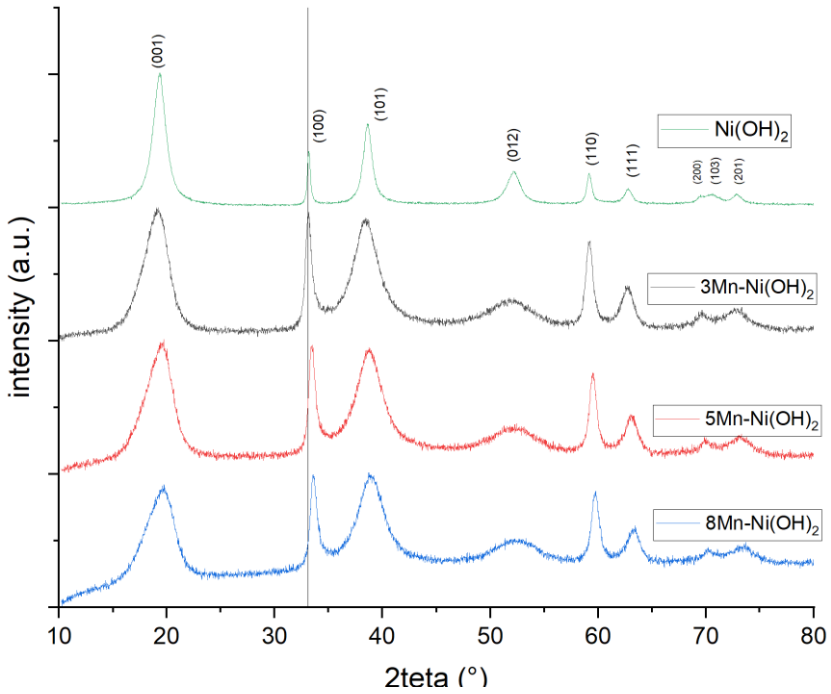

Figure 3.5 XRD patterns of the Mn-doped $Ni(OH)_2$ samples and $Ni(OH)_2$, all the data were normalized respect the peak (001).

The XRD patterns of the four samples are depicted in figure 3.5**.** All the peaks of the β phase reported in table 3.4 are present in figure 3.5, and no peaks related to the α-phase or separated Mn phases were present. This indicates that β-phase hydroxides were formed by this synthesis and that manganese was introduced in the $Ni(OH)_2$ structure. The decrease in intensity of the peaks for the doped samples implies their lower crystallinity.[27] The incorporation of Mn into the hydroxide structure was also confirmed by the shift of the diffraction peaks. Figure 3.6 shows the (100) peak in detail to describe this effect. The shift of the peak toward higher angles with the amount of Mn is observed, which indicates a contraction of the hydroxide structure.

This result is expected since the ionic radius of Mn (0.46 Å) is smaller than that of Ni (0.69 Å) and, therefore, the substitution of a Ni ion by a Mn one results in a contraction that is more evident when the amount of Mn increases.[28] The widening of the peak is also observed in Figure 3.6, and could be associated to a decrease of the crystallite size with the addition of Mn.[28] The crystallite size was calculated using the Scherrer formula and the values are reported in table 3.5. It can be seen that the crystallites get smaller with the amount of manganese and that there is a significant difference between the non-doped and the doped samples from 10.4 nm for the pristine hydroxide to 4.8 nm for the one with the highest amount of Mn.

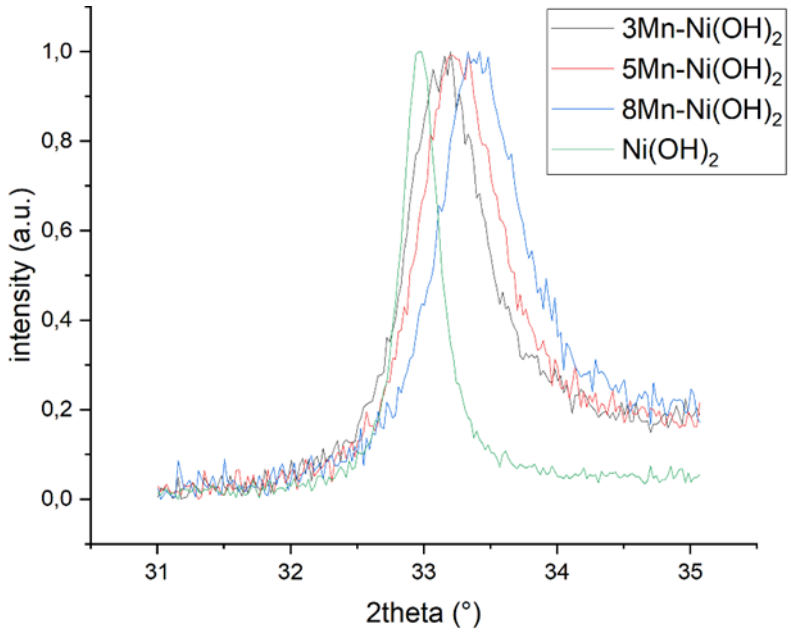

Figure 3.6 Detail of the (100) peak of the four different samples .

Table 3.5 Dimension of the crystallites calculated by using the Scherrer equation.

Sample	Crystallite dimension (nm)
$Ni(OH)_2$	10.4
3Mn-$Ni(OH)_2$	5.6
5Mn-$Ni(OH)_2$	5.5
8Mn-$Ni(OH)_2$	4.8

Figure 3.7 shows the X-ray absorption near-edge structure (XANES) data, and the corresponding Fourier-transform extended X-ray absorption fine structure (FT-EXAFS) spectra both at the Ni K and Mn K absorption edges. The Ni K XAS spectra of the $Ni(OH)_2$ and 8Mn-$Ni(OH)_2$ samples prepared in this thesis are very similar to that of the $Ni(OH)_2$ standard used as reference, confirming the structure of the sample. The main difference observed when comparing the XANES region of the sample with and without Mn is that the intensity of the white line (peak at around 8350 eV) increases after the addition of Mn. This indicates a change in the density states of Ni. In particular, the higher intensity is related to the fact that Ni has more unoccupied density of states. This result is quite unexpected, since a charge transfer from Mn (1.55) to Ni (1.91) was expected. The analysis of the XANES region indicates that the oxidation state of nickel is +2, as expected (Figure 3.10a). The FT-EXAFS spectra of the $Ni(OH)_2$-based materials show an intense peak at 1.6 Å, assigned to Ni-O interactions, and a peak at 2.76 Å related to Ni-Ni/Mn bonds. In the case of the sample with Mn, a slight shift of the second

peak towards lower values (2.73 Å) is observed (Figure 3.10b), which agrees with the lattice contraction deducted from XRD. This effect is also in agreement with results reported in the literature, where a shortening of the Ni-M bonds was observed after addition of Mn[29]. The analysis of the Mn K XANES region suggests that the oxidation state of Mn is +3.17 (see inset in Fig. 3.10c). In the literature, it has already been reported that Mn^{+3} ions substitute Ni^{+2} ions when $Ni(OH)_2$ is doped with Mn[29,30]. This results in an excess of positive charge in the $Ni(OH)_2$ layers, which results in the intercalation of anions in the interlayers[29] The Mn K FT-EXAFS shows a peak at 1.44 Å, related to Mn-O bonds, and another one at 2.79 Å, attributed to Mn-metal interactions[30].

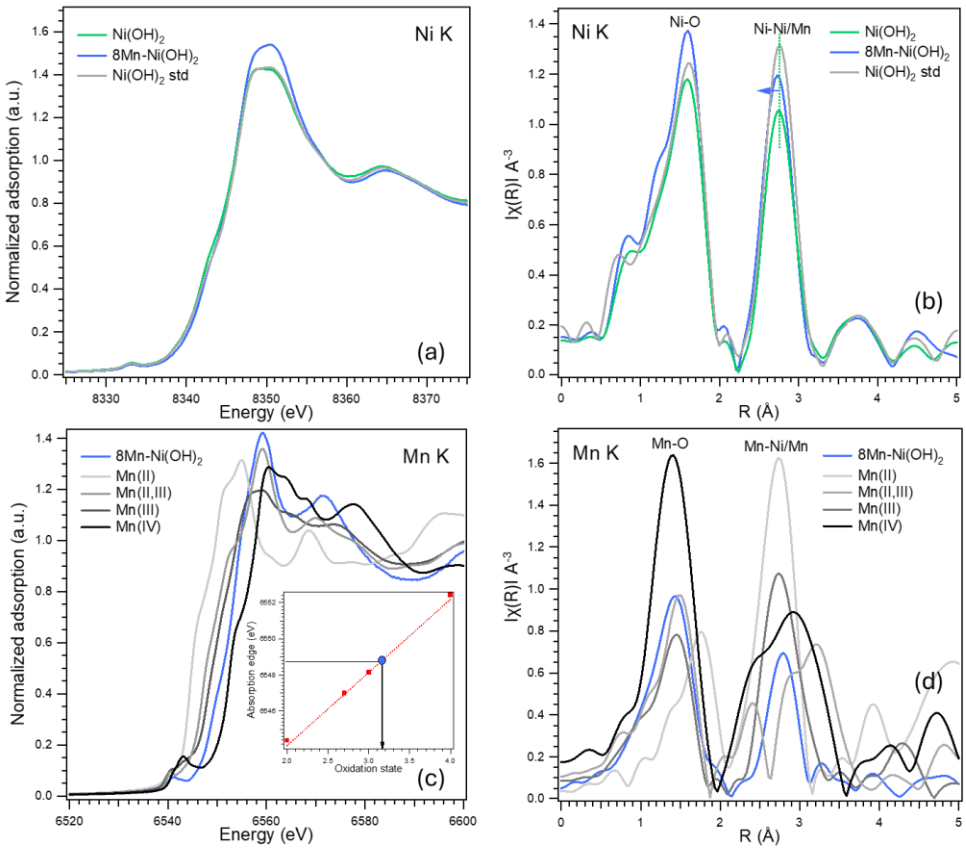

Figure 3.7 XANES (a,c) and corresponding FT-EXAFS (b, d) spectra at the Ni K (a, b) and Mn K (c, d) edges for Ni(OH)2 and 8Mn-Ni(OH)2. The references used for the determination of the Ni and Mn oxidation state are also shown.

The samples were also analyzed by X-ray photoelectron emission (XPS) to identify the oxidation state of the species and the composition at the surface. In particular, the O 1s, Ni 2p and Mn 2p regions were acquired.

Figure 3.8 shows the Ni $2p_{3/2}$ region for the four samples. As can be seen, all the samples present the same Ni 2p spectrum, which is characteristic of $Ni(OH)_2$.[31,32] To further confirm the only presence of Ni as $Ni(OH)_2$, the spectra were deconvoluted using seven different peaks attributed to nickel hydroxide (Figure 3.7). [31,32] Usually, the fit of the transition metals 2p regions is very challenging due to the complexity of their 2p spectra resulting from peak asymmetries, complex multiplet splitting, shake-up and plasmon loss structure, and uncertain, overlapping binding energies.[27] However, it was possible to get a good fit by using only one component, confirming the XRD results. For this reason, no other components such as nickel oxide were included in the analysis, even if it could be present at the surface of the particles due to interaction with the air.

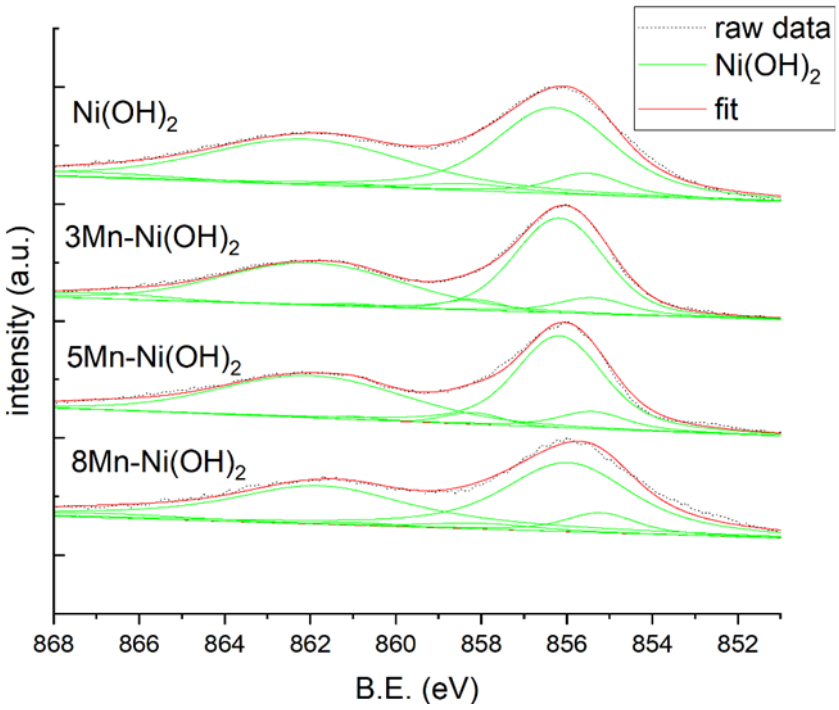

Figure 3.8 Normalized Ni $2p_{3/2}$ XPS region, and separation into chemically shifted components, of the $Ni(OH)_2$ and Mn-doped samples.

Figure 3.9 reports the O 1s region of 3Mn-$Ni(OH)_2$ as an example, since all the spectra were the same. A single peak centered at 531.6 eV was obtained in all cases, which is characteristic of hydroxides.[32] In addition, the presence of manganese was confirmed by XPS. As expected, the intensity of the Mn 2p region increased with the increase of doping concentration in the material. This region was also separated into chemically shifted components to determine the Mn oxidation states. However, it should be noticed that the spectra for the samples with the lowest amount of Mn are quite noisy and the Ni Auger peak overlaps with the Mn 2p region[33], therefore, the error in the fitting could be significant. For this reason, only the Mn 2p spectrum of the 8Mn-$Ni(OH)_2$ samples was analyzed. Results show that only Mn^{4+} is present at the surface of the particles, which could be the result of the oxidation of the Mn atoms in contact with air. In other works describing nickel hydroxides doped with manganese it was found the presence of this oxidation state and Mn^{3+}.[29,34,35] The presence of Mn^{4+} at the surface could explain the Mn oxidation state determined from XAS that was slightly higher than +3.

Finally the XPS measurements were used to determinate the surface composition of the modified samples. Table 3.6 reports the values obtained from XPS measurements, they are very close to the nominal values and to the values obtained by ICP and EDX measurements. This indicates that the Mn content is the same in the bulk of the material and on the surface.

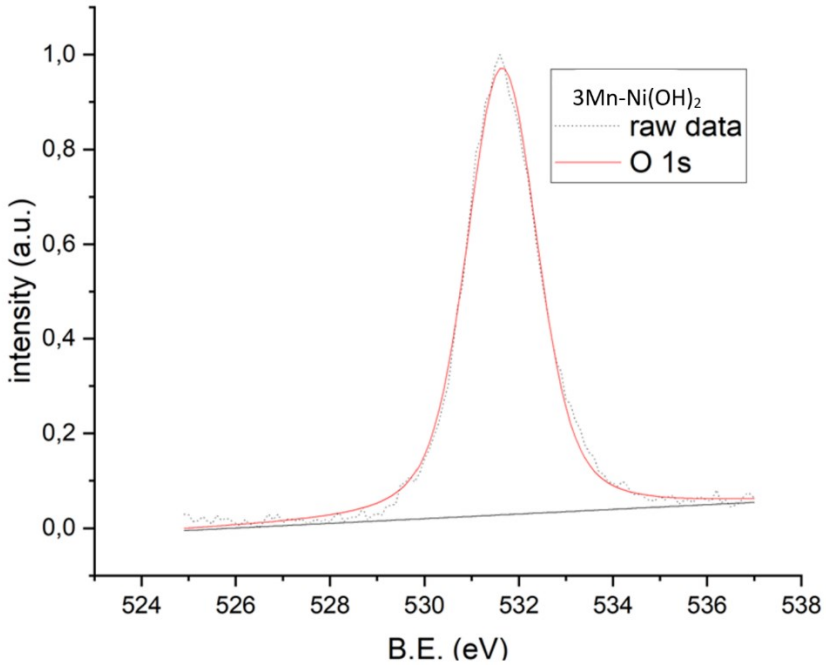

Figure 3.9 O 1s XPS spectrum of 3Mn-Ni(OH)$_2$. The raw data were fitted with a single peak at around 531.6 eV using characteristics of [23].

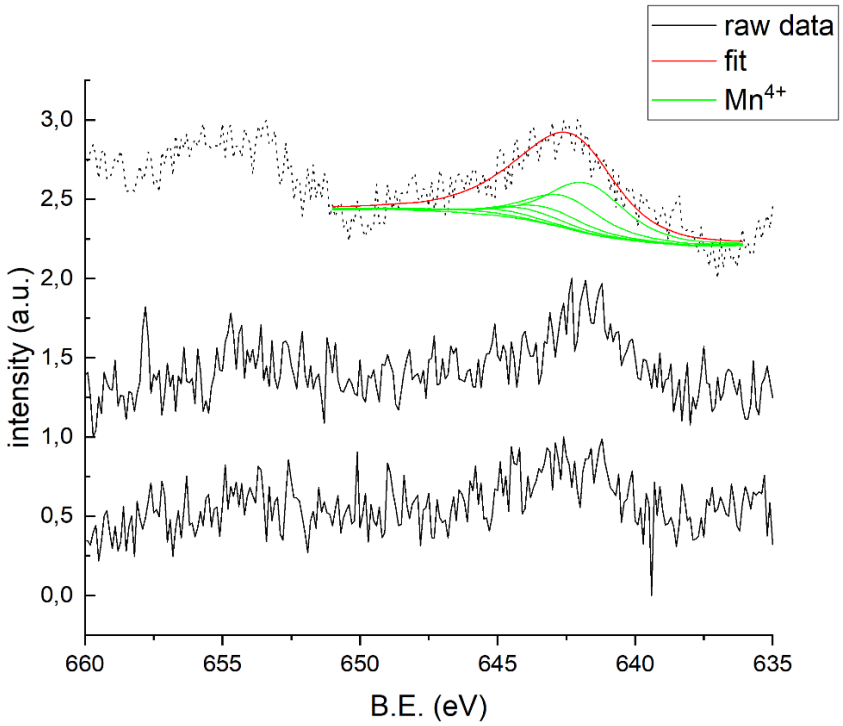

Figure 3.10 Mn 2p XPS region of the three Mn-doped samples. In green are represented the peaks associate with Mn^{4+}

Table 3.6 atomic Mn:Ni ratio obtained from the XPS measurements

sample	Atomic Mo:Ni ratio (%)
3Mn-Ni(OH)$_2$	3.0
5Mn-Ni(OH)$_2$	4.9
8Mn-Ni(OH)$_2$	7.8

3.3.2 Mo-doped hydroxides

The morphology of the synthetized Mo-modified hydroxides was also investigated by scanning electron microscopy (SEM). As it was observed for the Mn-doped hydroxides, also for these materials the SEM images evidence the presence of particles with a wide range of dimensions and with no defined shape (Figure 3.11), which can again be attributed to the synthesis technique utilized to obtain these materials. The particles went from hundreds of nanometers to hundreds of micrometers. Most of the particles were around tens of micrometers but in every sample at least a big particle with dimensions over 100 micrometers was found. The presence of Mo did not influence the morphology of the sample. Comparing with the Mn-based materials, it can be concluded that the addition of a second metal does not affect the morphology of the particles when this synthesis technique is used. No differences are present between the samples modified with different metals, both in the case of the Mo- and Mn-modified hydroxides a wide range of dimensions is present.

To evaluate the elemental composition of the particles and to verify the absence of contaminants, EDX analysis was performed. In this case, EDX was very useful to determine that Mo did not precipitate at pH=13 and it was necessary to decrease it to get the desired Mo concentration. This was later confirmed by XRF measurements of the supernatant liquid. EDX results are reported in Table 3.7. It can be seen that, also in this case, the experimental values are very close to the nominal ones. For the Mo-modified hydroxides, it was not possible to perform ICP measurements so, only the Mo/Ni ratio obtained from EDX is reported.

Table3.7 atomic concentration of Ni, O and Mo obtained from EDX measurements. The metals ratio is also reported.

Sample	Ni (at.%)	O (at.%)	Mo (at.%)	Atomic Mo:Ni ratio
$Ni(OH)_2$	20.6	79.4	/	/
8Mo-$Ni(OH)_2$	19.1	79.5	1.4	7.2
20Mo-$Ni(OH)_2$	21.0	74.9	4.0	19.3
30Mo-$Ni(OH)_2$	11.5	84.8	3.7	31.8

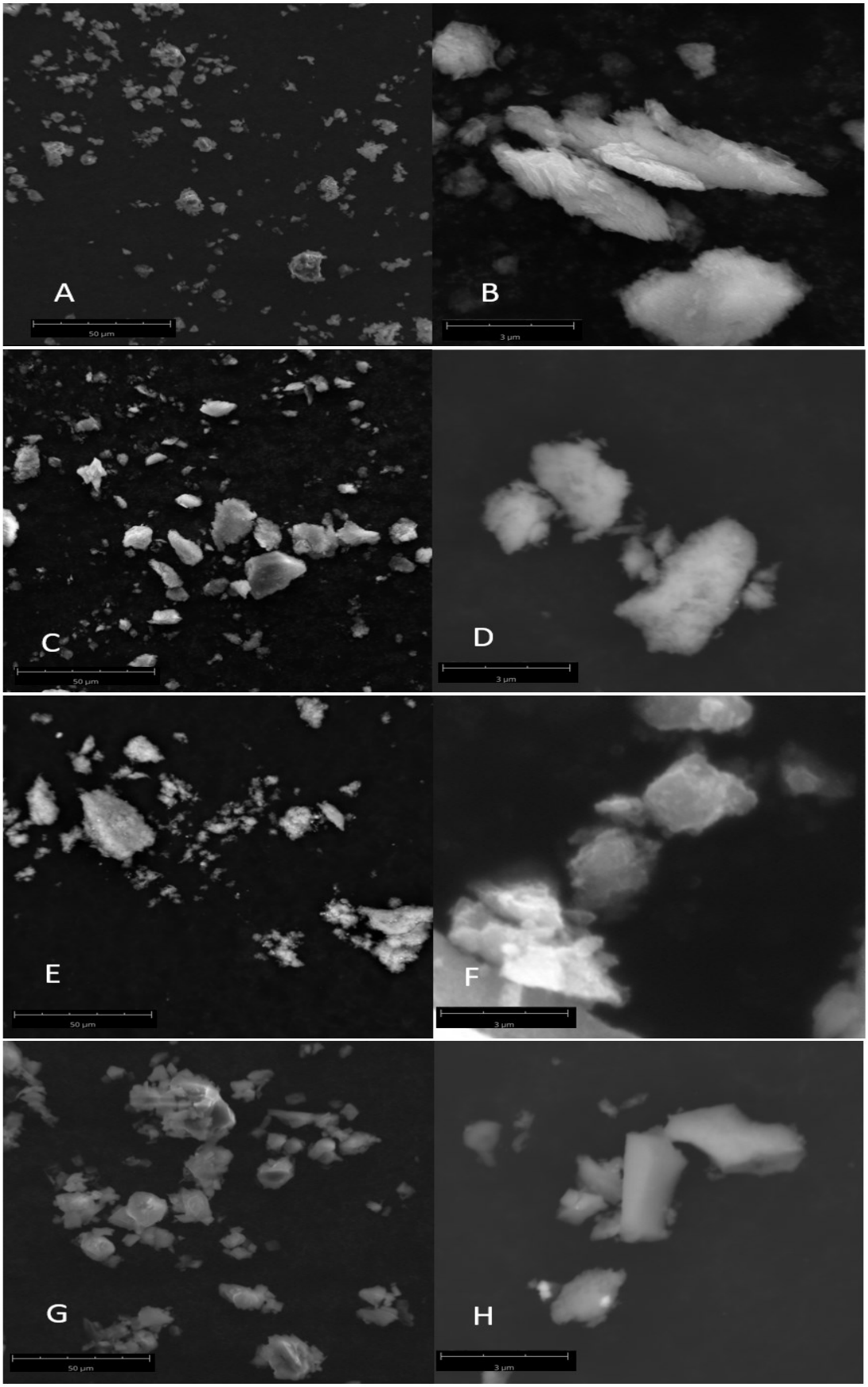

Figure 3.11 SEM images of $Ni(OH)_2$ (A and B), 8Mo-$Ni(OH)_2$ (C and D), 20Mo-$Ni(OH)_2$ (E and F), and 30Mo-$Ni(OH)_2$ (G and H). The scale bar of the left images is 50 µm, while the one of the right images is 3 µm.

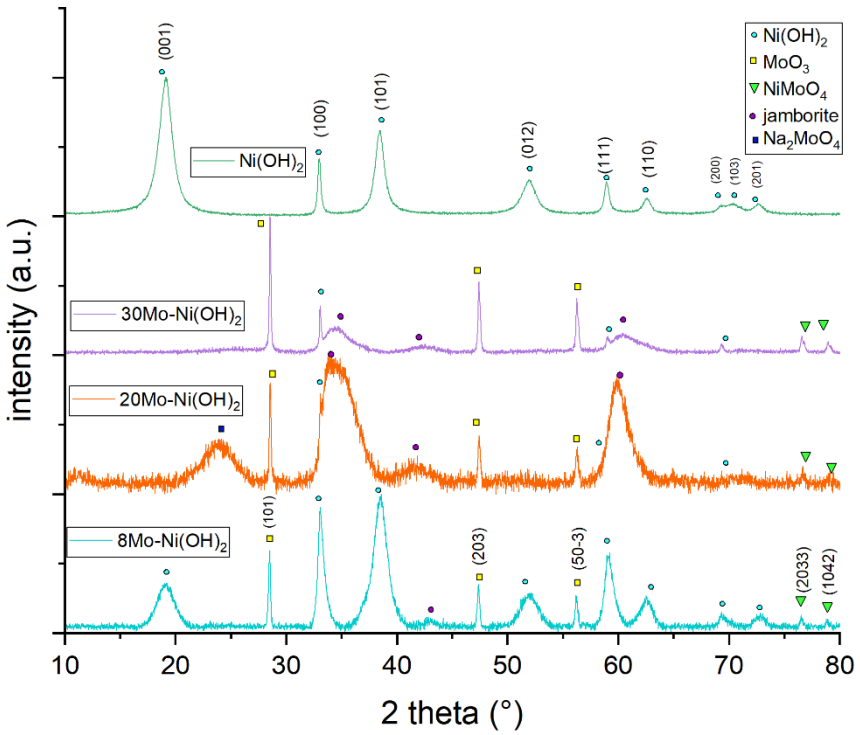

Figure 3.116 XRD patterns of the Mo-modified hydroxides. Different symbols were used to identify the peaks associated with different phases present in the sample. In the case of "jamborite" and "NaMoO" the peaks visible in the spectra are due to the presence of more than one peak in the same region, to keep the graph clean only one symbol was used.

The powders were analyzed by X-ray diffraction to determine the different phases present in the sample. In figure 3.12**,** the XRD patterns of the Mo-modified hydroxides are reported. In this case, multiple phases were present in the samples, since additional peaks to those reported in table 3.4 for β-$Ni(OH)_2$ were observed. The intensity of the additional peaks increases with the amount of Mo, therefore, they can clearly be associated to separated Mo phases. The sample with the lowest amount of Mo, 8Mo-$Ni(OH)_2$, presents all the peaks associated with the β-phase of nickel hydroxide. In addition, it shows peaks at 28.49°, 47.41°, and 55.92° associated to the (101), (203) and (50-3) diffraction peaks of $MoO_3 \cdot 0.5H_2O$ (PDF 37-0519), respectively, as well as the peaks at 76.91° and 78.63° associated to the (2033) and (1042) diffraction peaks of $NiMoO_4$ (PDF 86-0362). For the samples with higher amount of Mo, the intensity of the peaks related to $Ni(OH)_2$ decreases while the one of the peaks related to Mo phases increases. This means that not all the molybdenum was incorporated into the hydroxide structure and some precipitated in the form of oxides. In the 20Mo-$^{Ni}(OH)_2$ and 30Mo-$Ni(OH)_2$ patterns, there are also present other three wide peaks identified with a purple circle at around 35°, 42°, and 60°. Using high score plus it was possible to attribute them to nickel oxide hydroxide, also known as jamborite ($Ni_5O(OH)_9$ PDF 27-0340). The width and asymmetry of the peaks could be due to the overlap of multiple peaks. For example, the peak at around 35° for sample 20Mo-$Ni(OH)_2$ could contain three peaks at 33.88°, 34.58°, and 35.82°, characteristic of this phase. 20Mo-$Ni(OH)_2$ shows an additional peak at around 24°, only observed in this sample, that can be related to sodium molybdate hydrate (22.93°, 24.28°, 24.77°, PDF 88-1266), which is the molybdenum precursor used during the synthesis. This would mean that part of the precursor did not dissolve, and it was still present at the end of the process. For the molybdenum-based samples, the shift of the XRD peaks related to nickel hydroxide was not observed, as expected since the ionic radius of Ni (0.69 A) and Mo (0.65 A) is very similar. This makes more difficult to

confirm that Mo was introduced into the $Ni(OH)_2$ structure, also because different Mo phases were identify by XRD. It must be highlighted that the amount of Mo was higher than in the case of Mn.

XAS measurements were also performed to determine the oxidation state of molybdenum and to get information about the structure of the samples. Figure 3.13 reports the XANES data and the corresponding FT-EXAFS spectra both at the Ni K and Mo K absorption edges. Also in this case, The Ni K XAS spectra of 8Mo-$Ni(OH)_2$ is very similar to that of $Ni(OH)_2$, confirming the structure of the sample and the XRD results. The intensity of the white line (peak at around 8350 eV) after the addition of Mo, however, increases, which indicates a change in the density states of Ni. In particular, the higher intensity is related to the fact that Ni has more unoccupied density of states. This could be attributed to the charge transfer from Ni (1.91) to Mo (2.16) that has a higher electronegativity. The analysis of the XANES region indicates that the oxidation state of nickel is +2, as expected (Figure 3.13a). The FT-EXAFS spectra of the $Ni(OH)_2$-based materials show an intense peak at 1.6 Å, assigned to Ni-O bonds, and a peak at 2.76 Å related to Ni-Ni/Mo bonds. In the case of the sample with Mo, a slight shift of the second peak towards lower values (2.73 Å) is observed (Figure 3.13b). The set of peaks located at distances beyond 3 Å for $Ni(OH)_2$ indicate a well-ordered local environment of nickel atoms. After the introduction of Mo, this ordering decreases, which could demonstrate the introduction of part of the Mo into the $Ni(OH)_2$ structure.

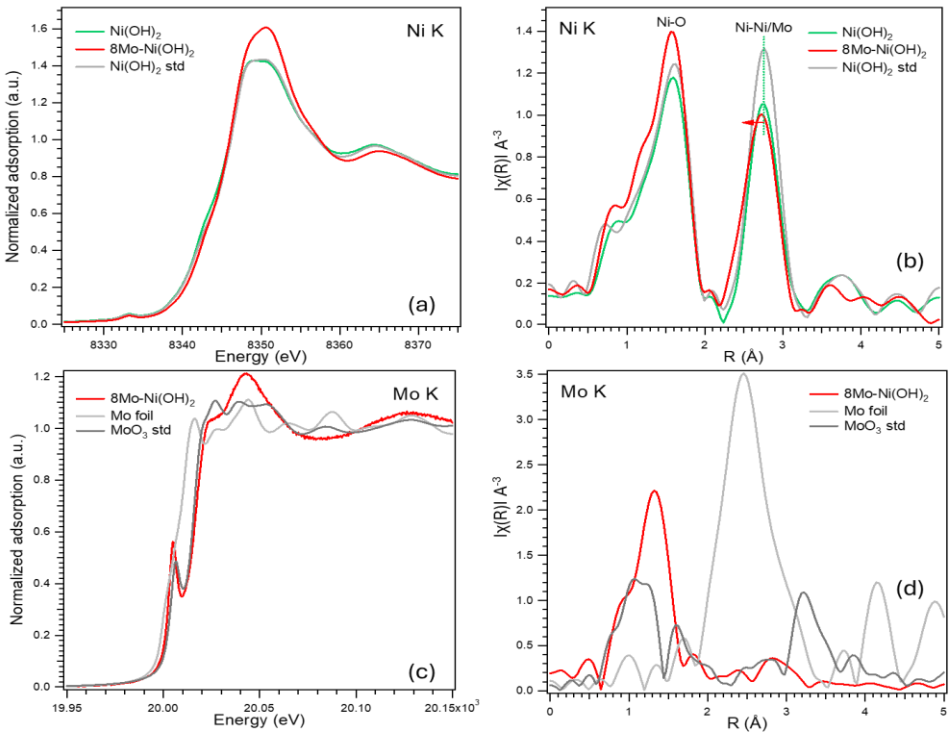

Figure 3.13 XANES (a,c) and corresponding FT-EXAFS (b, d) spectra at the Ni K (a, b) and Mo K (c, d) edges for Ni(OH)2 and 8Mo-$Ni(OH)_2$. The references used for the determination of the Ni and Mo oxidation state are also shown.

The analysis of the Mo K XANES region suggests that the oxidation state of Mo is close to +6 (Figure 3.13c), in agreement with the results reported in the literature[36]. As explained above for Mn-based samples, the introduction of Mo atoms with a higher oxidation state than Ni results in an excess of positive charge in the $Ni(OH)_2$ layers that is compensated through the intercalation of anions in the interlayers[29]. The Mo K FT-EXAFS only shows a peak at 1.3 Å related to Mn-O bonds. The absence of peaks with high intensity at long distances suggests that the Mo environment is strongly disordered[37]. Comparing the FT-EXAFS spectra of 8Mo-$Ni(OH)_2$

with that of the MoO_3 reference, it can be seen that they are very different, which could be a further confirmation of the fact that part of molybdenum is introduced into the $Ni(OH)_2$ structure, and the excess of Mo forms a separated MoO_3 phase.

The samples were also analyzed by X-ray photoelectron emission (XPS) to identify the oxidation state of the species and the composition at the surface. The O1s, Ni 2p and Mo 3d regions were acquired. Figure 3.14 reports the Ni 2p XPS region of the Mo-modified samples. As described above for the Mn-doped samples, the spectra were deconvoluted using seven peaks, all of them associated to $Ni(OH)_2$.[23] Also in this case, a good fit was obtained just using the $Ni(OH)_2$ component. The shift of the Ni 2p spectra of the Mo-based samples towards higher binding energies was negligible as expected, since the electronegativity of Ni (1.91) and Mo (2.16) are similar. The O 1s region (not shown) showed only one single peak at 531.6 eV, attributed to hydroxide species. [23]

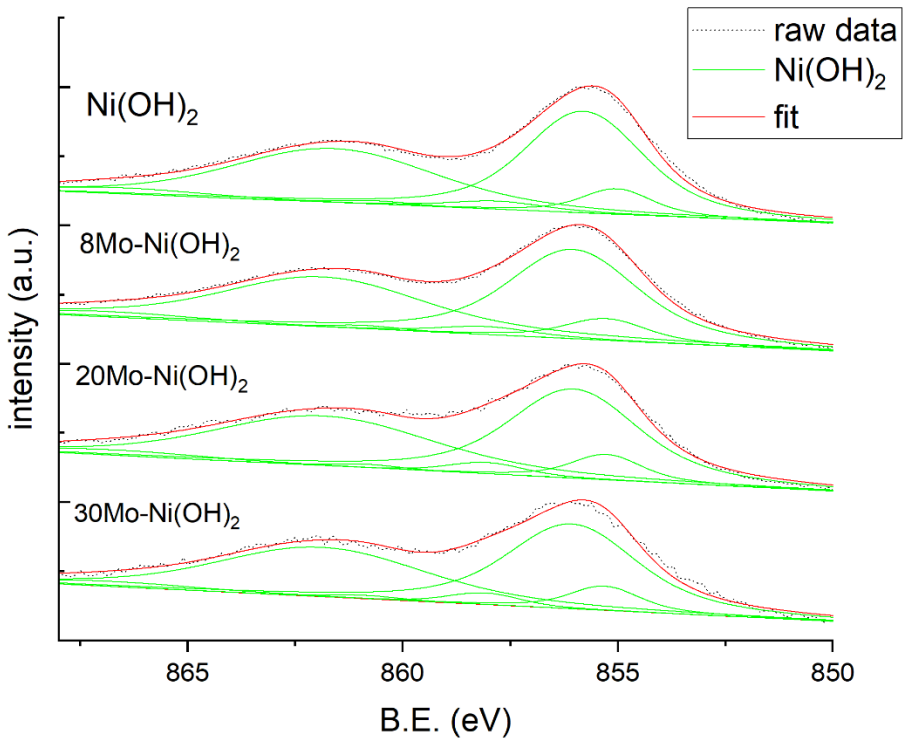

Figure 3.14 Ni 2p3/2 XPS region, and separation into chemically shifted components, of $Ni(OH)_2$ and the Mo-modified samples.

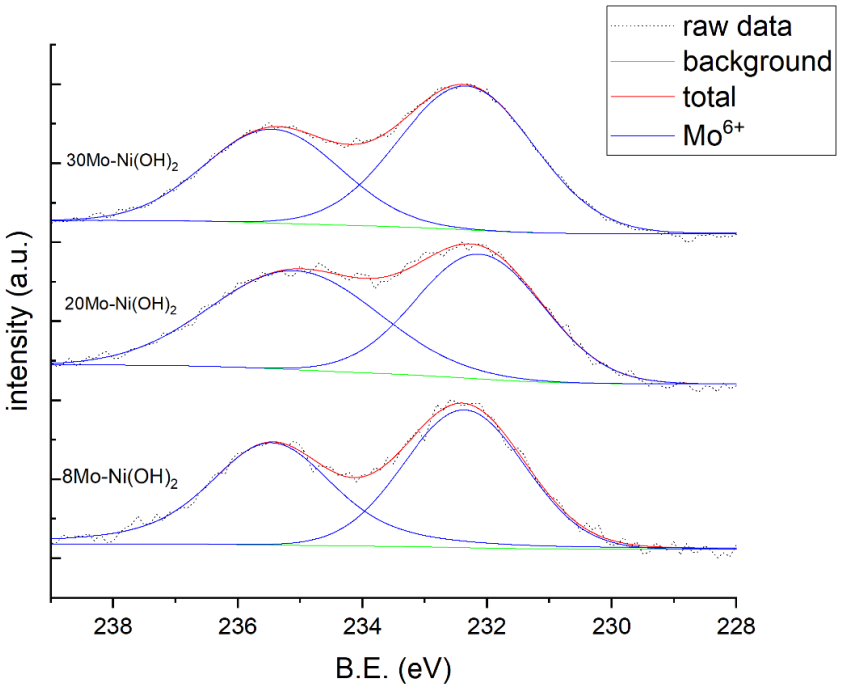

Figure 3.15 Mo 3d XPS region, and separation into chemically shifted components, of the Mo-modified samples.

Figure 3.15 reports the Mo 3d region. The data were deconvoluted using two peaks at 232.3 eV and 235.5 eV, associated to the Mo $3d_{5/2}$ and Mo $3d_{5/2}$ of Mo^{6+}, respectively.[38] The Mo^{6+} peaks can be attributed to the presence of MoO_3, in agreement with the XRD results (figure 3.12). In multiple works describing the doping with molybdenum, it has been reported through XPS that Mo^{6+} ions are the dopant species,[1,18,39–41] although it has also been reported the presence of Mo^{5+} in other works.[40,41] For a better determination of the oxidation state of the Mo species, XAS measurements were performed and confirmed the presence of Mo^{6+}

Table 3.8 atomic Mo:Ni ratio obtained from the XPS measurements

sample	Atomic Mo:Ni ratio (%)
8Mo-Ni(OH)$_2$	2.9
20Mo-Ni(OH)$_2$	8.4
30Mo-Ni(OH)$_2$	18.1

Finally the XPS measurements were used to determinate the surface composition of the modified samples (table 3.8). The Mo:Ni ratio in the surface determined by XPS is lower than the nominal one and that determined by EDX. This indicates a Ni segregation from the bulk to the surface.

3.4 Electrochemical characterization

The Mn- and Mo-modified samples, as well as $Ni(OH)_2$, were tested as UOR catalysts and the results are discussed in the following. All potential values reported in this thesis are referred to the reversible hydrogen electrode (RHE). The current was normalized and corrected considering the ohmic drop in the electrolyte solution.

3.4.1 Mn-doped hydroxides

First, the samples were tested in absence of urea to determine the electrochemical surface area (ECSA) and the Ni^{2+}/Ni^{3+} redox potential (see the details in Chapter 2). Figure 3.16 reports the CVs for all the samples. All the CVs present an oxidation peak between 1.4 V and 1.5 V, related to the oxidation of the Ni^{2+} ($Ni(OH)_2$) species to Ni^{3+} (NiOOH), and the corresponding reduction one at around 1.3 V[7].

The oxidation current observed at potentials higher than 1.6 V is associated with the oxygen evolution reaction (OER), which is a catalytic reaction. The Ni^{2+}/Ni^{3+} redox peaks overlap with the beginning of the OER, making difficult the accurate determination of the OER onset potential. To study the effect of the addition and amount of Mn on the OER activity of the $Ni(OH)_2$-based catalysts, the current was first normalized by the geometric area of the electrode (Figure 3.16a). As can be seen, only the 5Mn-$Ni(OH)_2$ sample exhibits slightly higher current densities than $Ni(OH)_2$, while the 3% and 8% Mn samples show lower currents than the ones registered for the non-doped sample. It has to be highlighted that the electrodes were prepared by drop casting of catalyst inks that were very difficult to obtain in an homogeneous way since each sample had a different tendency to disperse[42]. This is probably due to the fact that all the samples presented particles with a wide range of dimensions, and this made difficult to obtain a full dispersion in the ink and this heavily effected the deposition process. This resulted in a significant error in the amount of deposited material (also deduced from the area of the Ni^{2+}/Ni^{3+} redox peaks) and, therefore, the conclusions extracted from Figure 3.14a were not reliable. To solve this problem and be able to compare the performance of the different materials, currents were also normalized by the ECSA, which is directly related to the amount of Ni sites. In this way, it was possible to compare the specific activity of the Ni sites (Figure 3.14b). The values of the current densities are lower as expected, since the ECSA values are much higher than the geometric area of the electrode. In figure 3.14b, a clear tendency with the amount of Mn can be seen now. The activity, in terms of both current density and onset potential, increases with the amount of Mn and is higher than that of $Ni(OH)_2$. Only the sample with the 3 at.% of Mn shows a worse performance than the non-doped sample.

Table 3.9 position of the oxidation peaks and reduction peaks of the sample present in figure 3.14. it's reported the distance between the two peaks in mV

Sample	Oxidation peak (V)	Reduction peak (V)	Peak separation (mV)
$Ni(OH)_2$	1.46	1.30	160
3Mn-$Ni(OH)_2$	1.45	1.31	140
5Mn-$Ni(OH)_2$	1.45	1.32	130
8Mn-$Ni(OH)_2$	1.43	1.32	110

Table 3.9 reports the position of the Ni^{2+}/Ni^{3+} redox peaks and the peak separation. It is clear how the presence of manganese in the sample helps to shift the oxidation peak towards lower potentials respect to the non-modified sample, meaning that it is easier to produce Ni^{3+}, which is the active species for the urea

oxidation reaction, this is beneficial for both the catalysis of OER and UOR, it will be expanded in the next paragraph. The shift of the peak increases with the manganese content. The peak separation is an indicator of the electronic conductivity of the material, the lower the separation the higher the conductivity[43]. The peak separation decreases with the amount of manganese in the sample. It is difficult to accurately determine the onset potential from these CVs since in most of the cases it overlaps with the Ni redox couple. In literature the addition of manganese to the nickel hydroxide translates in increase in catalytic activity for the OER: increase of current density and lower overpotential to achieve a current density of 10mA/cm^2.[44] On the other hand, a very high quantity of manganese (Mn:Ni ratio of 1:1) results in a decrease of the activity. The peak positions are similar to the values reported in table 3.9. The presence of manganese also shifted the oxidation peaks towards lower potential and the higher the manganese content the higher the shift, except for the 1:1 sample[44].

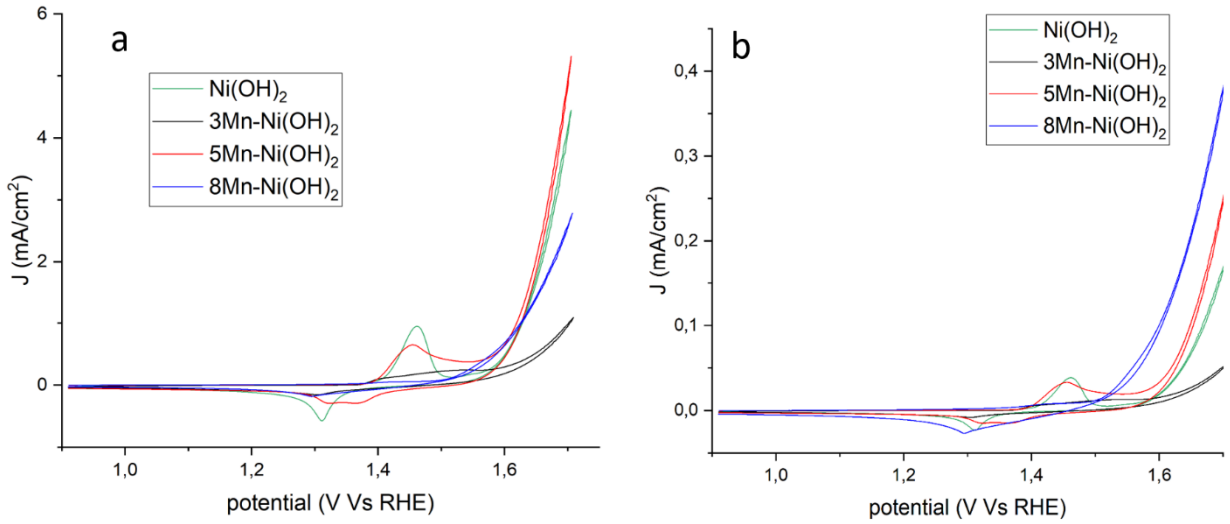

Figure 3.16 CVs in 1 M KOH of the $Ni(OH)_2$ and Mn-doped $Ni(OH)_2$ samples. The current was normalized by the geometric area (0,0707cm^2) of the electrode (at); and by the ECSA (b).

From the data obtained it was possible to draw the Tafel plots for the nickel hydroxide sample and the manganese-modified samples, figure 3.17. The values of Tafel slopes (reported in the graph) show that the presence of manganese in the samples hinders the kinetics of the reaction. The three Mn-containing samples show an increase in Tafel slope respect to the non-modified sample but there is not a particular trend since the highest value is associated with the 3Mn sample meanwhile the other two have a similar value. The value for the non-modified sample is close to values reported in literature being around 90 mV/dec[45]. However, the increase in slope with the presence of manganese is in agreement with what found in literature[46].

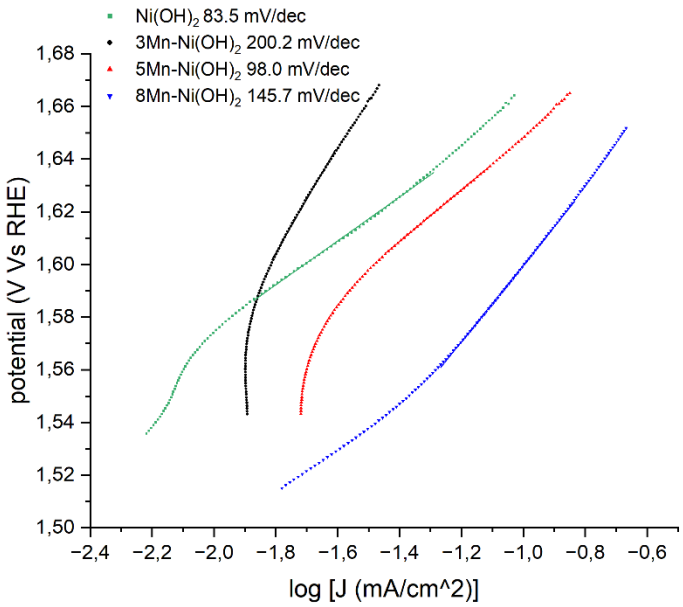

Figure 3.17 Tafel analysis of the LSVs in 1 M KOH of the $Ni(OH)_2$ and the manganese-modified samples.

Then, urea was added to the electrolyte, and linear sweep voltammetries (LSVs) were recorded. Figure 3.18 reports the LSVs of the Mn-modified and unmodified samples for UOR. The OER LSVs are also reported for comparison. In correspondence of the oxidation of the Ni^{2+} species to Ni^{3+}, the current starts to increase, which is attributed to the oxidation of urea catalyzed by the Ni^{3+} species, as described in Chapter 1. The presence of urea in solution makes possible to produce hydrogen at much lower cell potentials because the oxidation of urea starts at lower potentials than the oxygen evolution reaction, since the UOR is linked with the presence of Ni^{3+} species, as discussed before. All the samples reached higher currents with the presence of urea in the solution. The manganese-modified samples showed an increase in activity respect to the non-modified sample, and this is due to the fact that the manganese helped to shift the oxidation peak of nickel towards lower potentials (table 3.9) and, for this reason, the urea oxidation starts at lower potentials. The increase of activity is linked with the manganese content, the higher the content the higher the current reached and the lower the potential at which the urea oxidation starts. The onset potentials of the samples are reported in table 3.10. It is important to point out that these values are not very accurate since there are two processes that overlap: the oxidation from Ni^{2+} to Ni^{3+} and the urea oxidation. This makes difficult to obtain the accurate onset of the UOR. However, since the UOR is tightly linked to the oxidation of nickel, the values reported in table 3.10 are still a good indicator because if the nickel oxidation starts at lower potential consequently the UOR starts at lower potentials. The main difference is between the 8Mn-$Ni(OH)_2$ sample and the other two modified samples, since the 5Mn-$Ni(OH)_2$ and 3Mn-$Ni(OH)_2$ shows a similar behavior but for 5Mn-$Ni(OH)_2$ the oxidation starts slightly earlier (table 3.9) and it reaches slightly higher currents. The increase in activity of the Mn-modified samples respect to the $Ni(OH)_2$ sample is also reported in literature[35]. In [37] is reported that the presence of manganese in the sample shifts the onset potential of about 40 mV, for the samples of this work the shift increases with the amount of the manganese and in the case of the 8M-$Ni(OH)_2$ sample it reaches 40 mV.

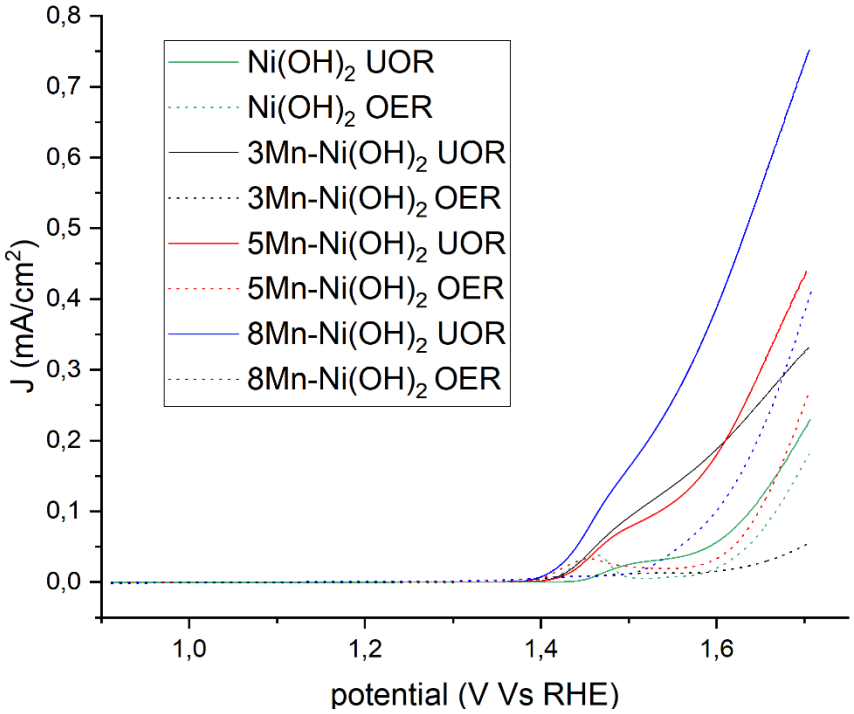

Figure 3.18 LSVs in 0.33 M urea + 1 M KOH (solid lines) of the $Ni(OH)_2$ and Mn-doped $Ni(OH)_2$ samples. The LSVs in absence of urea (OER) are reported as reference (dotted lines).

Table 3.10 the on-set potentials of the samples are reported in the central column and on the last column is reported the difference between the on-set value of the non-modified material and the on-set value of the modified material.

sample	Onset (V)	Shift (mV)
$Ni(OH)_2$	1.44	-
3Mn-$Ni(OH)_2$	1.42	20
5Mn-$Ni(OH)_2$	1.41	30
8Mn-$Ni(OH)_2$	1.40	40

To obtain information about the reaction kinetics, the Tafel analysis was performed (figure 3.19). The Tafel slopes are presented in table 3.11. A lower Tafel slope signifies a more favorable reaction kinetics, in this case the lower slope was obtained with the 3Mn-NiP sample (23.2 mV/dec), even though all the Mn-doped samples have similar values. It is important to highlight that these values are obtained from LSVs measurements and, in the region in which the Tafel slope is calculated, two process are overlapped, as described previously, so these are indicative values used to compare it with the OER values and the ones in literature. These values are comparable to the ones found in literature for Nickel hydroxide.[47,48] The significant increase of the values from UOR to OER demonstrates what already discussed in Chapter 2: substituting OER by UOR at the anode side can help to reduce the problem of the OER sluggish kinetics.

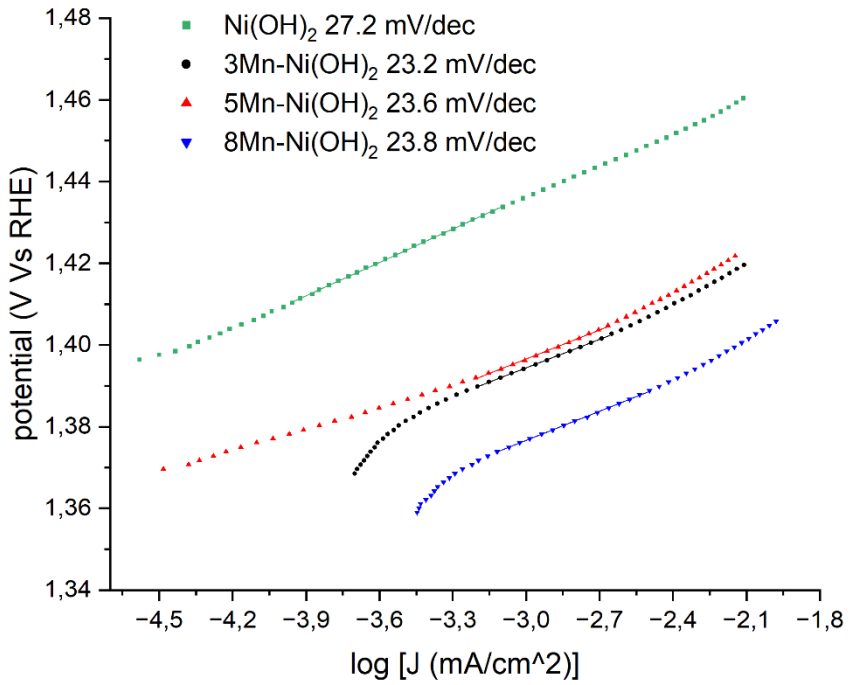

Figure 3.19 Tafel analysis of the LSVs in 0.33 M urea + 1 M KOH

Table 3.11 Tafel slope values determined from figure 3.19 for $Ni(OH)_2$ and the three Mn-doped samples.

sample	Tafel slope (mV/dec) (UOR)	Tafel slope (mV/dec) (OER)
$Ni(OH)_2$	26.0	83.5
3Mn-$Ni(OH)_2$	23.2	200.2
5Mn-$Ni(OH)_2$	23.6	98.0
8Mn-$Ni(OH)_2$	23.8	145.7

3.4.2 Mo-doped hydroxides

The same procedure described above was performed for the test of the Mo-based materials. Figure 3.20 reports the CVs in absence of urea for the nickel hydroxide and the three Mo-modified samples. The Ni^{2+}/Ni^{3+} redox couple is observed in the same potential window described for the Mn-based samples. The addition of the second metal can facilitate the oxidation of Ni^{2+} species to Ni^{3+} species and this could be beneficial for the UOR since urea is catalysed by the oxidized species. The effect of the molybdenum on the nickel oxidation peak is summarized in table 3.12. The oxidation peak is shifted towards lower potential by adding molybdenum to the sample. For the 20Mo-$Ni(OH)_2$ and 30Mo-$Ni(OH)_2$ samples, the effect is more or less the same, which could be due to the fact that the amount of molybdenum that really entered the structure is the same even if the total amount of molybdenum is different. As previously discussed, the peak separation is indicative on the conductivity of the sample, the values decreases with the increase of molybdenum content. In the case of the 30Mo-$Ni(OH)_2$ and 20Mo-$Ni(OH)_2$ sample is less than half the value of the non-modified sample.

Table 1.12 position of the oxidation peaks and reduction peaks of the sample present in figure 3.20. it's reported the distance between the two peaks in mV

sample	Oxidation peak (V)	Reduction peak (V)	Peak separation (mV)
$Ni(OH)_2$	1.46	1.30	160
8Mo-$Ni(OH)_2$	1.45	1.34	110
20Mo-$Ni(OH)_2$	1.41	1.33	80
30Mo-$Ni(OH)_2$	1.41	1.34	70

The currents observed at potentials higher than 1.6 V are related to the OER. Comparing the CVs normalized by the geometric area (Figure 3.17a), it seems that the addition of Mo has a negative effect on the activity. However, as explained above for the Mn-samples, the conclusions extracted from this plot are not reliable. For this reason, currents were also normalized by the ECSA (Figure 3.17b). in this case, all the samples behave in a very similar way concluding that the presence of Mo does not have a significant effect on the OER activity of these materials. Just comparing the behaviour of the Mo-based samples and taking into account their composition, it could be concluded that the presence of MoO_3 and $NiMoO_4$ increases the activity and not the Mo-doping, since the 8Mo-$Ni(OH)_2$ sample is the lest performant one. In literature, it was found that the presence of molybdenum affects the oxidation peak position shifting it towards lower potentials but it did not have any particular effect on the on-set potential or the current density[49]. In literature it was found that MoO_3 is a bad catalyst for OER and it has to be modified to be used for this application[50]. This means that the fact that the 20Mo-$Ni(OH)_2$ and 30Mo-$Ni(OH)_2$ samples have a better performance than the 8Mo-$Ni(OH)_2$ sample is not due to the presence of more MoO_3 but probably to the fact that more of the molybdenum inserted in the sample entered the structure and actively effected the properties of the material, as demonstrated by the higher shift of the oxidation peak in this samples respect to the 8Mo-$Ni(OH)_2$ sample. In literature it was found that the inactive phase MoO_2 was used to enhance the performance of nickel-based catalysts for the UOR[51]. This could mean that also the Mo_3 phase could help enhance the activity of the samples of this work

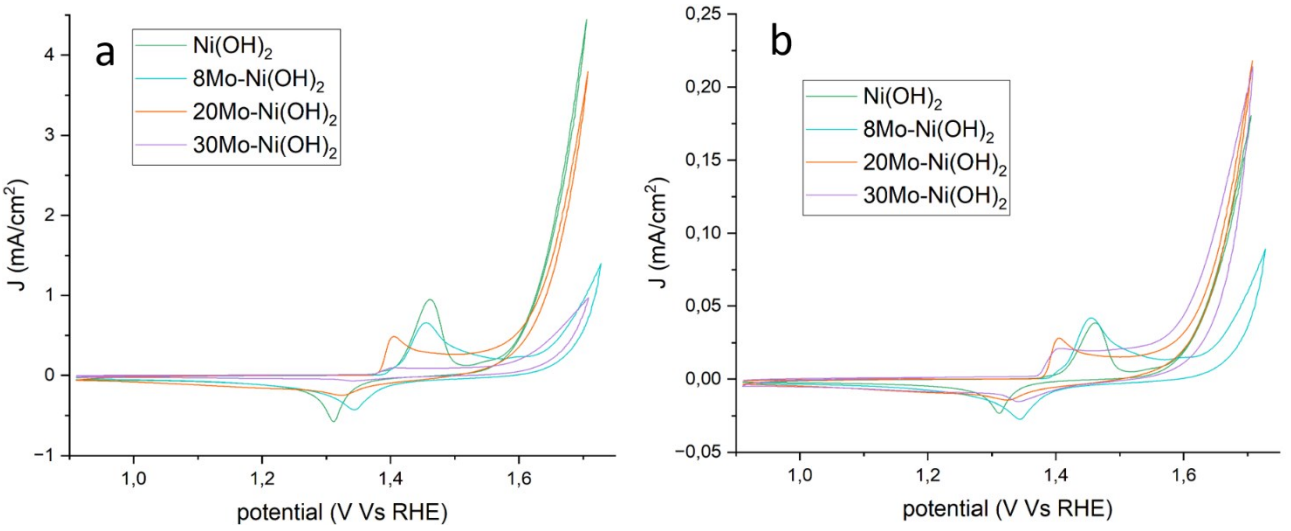

Figure 3.20 CVs in 1 M KOH of the $Ni(OH)_2$ and Mo-doped $Ni(OH)_2$ samples. The current was normalized by the geometric area (0,0707cm^2) of the electrode (left); and by the ECSA (right).

From the data obtained it was possible to draw the Tafel plots for the nickel hydroxide sample and the molybdenum-modified samples, figure 3.21. The Tafel slope values can be seen in figure 3.21. the presence of molybdenum seems to hinder the kinetics of the reaction since the slope values of all the modified sample are higher than the one of the non-modified sample, the higher the molybdenum amount the higher the slope value. The Tafel slope value for the non-modified sample is, as already stated, close to values found in literature. The Tafel slope values for the molybdenum-modified samples are also similar to what found in literature[49].

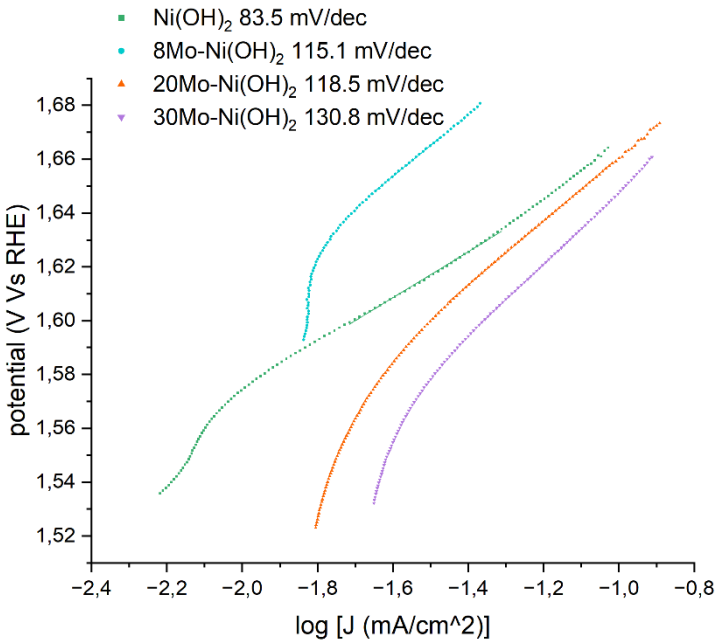

Figure 3.21 Tafel analysis of the LSVs in 1 M KOH of the $Ni(OH)_2$ and the molybdenum-modified samples

Then, urea was added to the electrolyte, and linear sweep voltammetries (LSVs) were recorded. Figure 3.22 reports the LSVs of the $Ni(OH)_2$ and the Mo-modified samples. Like for figure 3.18 also in this case the OER LSVs are reported with dotted lines meanwhile the UOR LSVs are reported with full lines of the same color of the respective OER LSV. It's possible to see that the current for the UOR LSVs starts to increase in correspondence of the nickel oxidation peak described by the dotted line. The presence of urea make it possible to reach much higher currents at lower potential and this translates in the opportunity to produce hydrogen at much lower potentials. All the samples reached higher currents in presence of urea respect to the case in which urea was absent. The urea oxidation is strictly correlated with the nickel oxidation from Ni^{2+} to Ni^{3+}. The Molybdenum-modified samples present a shift towards lower potential of the oxidation peak (table 3.12) and this translate in higher activity towards UOR because the oxidation of nickel starts at lower potentials. The 20Mo-$Ni(OH)_2$ and 30Mo-$Ni(OH)_2$ samples present a significative shift of the peak respect to the non-modified sample meanwhile the 8Mo-$Ni(OH)_2$ sample show a much smaller shift. The two sample with the higher shift show also the higher currents, in particular the 20Mo-$Ni(OH)_2$ sample that showed the highest current of all the samples, meanwhile the 8Mo-$Ni(OH)_2$ sample with the lowest shift showed also the smallest current of the molybdenum-modified samples. in table 3.13 are reported the on-set potentials of the samples, as discussed before it is important to remember that in the region in which the on-set is calculated two different process overlap. This values are still indicative of the activity of the material and it is possible to see how the 20Mo-$Ni(OH)_2$ and 30Mo-$Ni(OH)_2$ have the same on-set and consequently the same shift from the on-set of the non-modified sample meanwhile the 8Mo-$Ni(OH)_2$ sample present a smaller shift,

as expected since the nickel oxidation peak of this sample is at higher potential than the other two sample and for this reason urea oxidation starts at higher potential. In literature it was found that the presence of molybdenum increase the activity of the nickel based material[52].

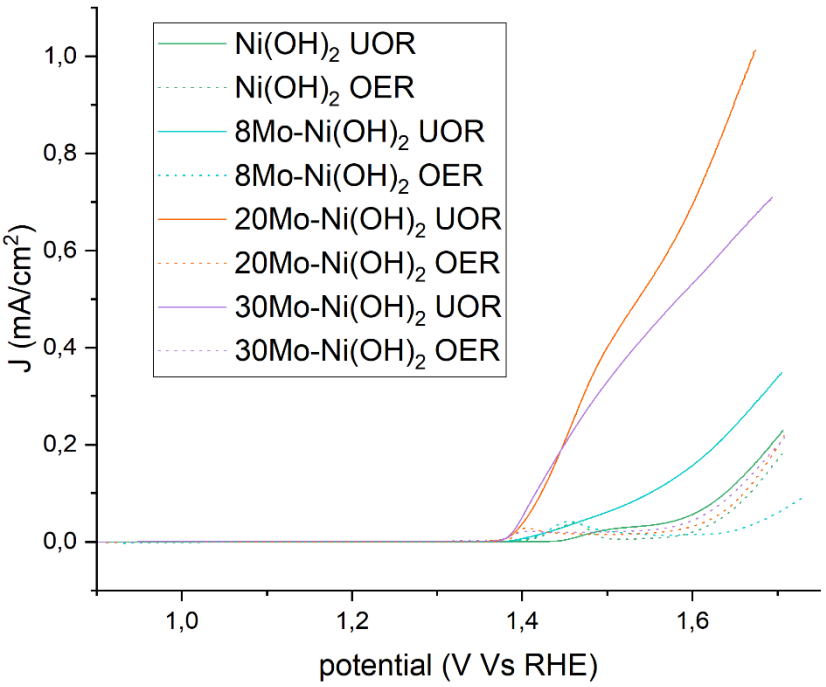

Figure 3.22 Graph reporting the LSVs from 0,9 to 1,7V Vs RHE of the $Ni(OH)_2$ and the Mo-doped samples. with the full lines are reported the LSV in UOR conditions meanwhile whit the dotted lines are reported the LSV of the same samples in OER conditions

Table 3.13 the on-set potentials of the samples are reported in the central column and on the last column is reported the difference between the on-set value of the non-modified material and the on-set value of the modified material.

sample	On-set (V)	Shift (mV)
$Ni(OH)_2$	1.44	-
8Mo-$Ni(OH)_2$	1.41	30
20Mo-$Ni(OH)_2$	1.38	60
30Mo-$Ni(OH)_2$	1.38	60

To obtain information about the reaction kinetics, the Tafel analysis was performed (figure 3.23). The Tafel slopes are presented in table 3.14. As already seen for the manganese doped materials, also in this case the slope values are much smaller in presence of urea compared to those in absence of urea. The date in table 3.14 are indicative and not accurate because in the region in which the Tafel analysis is done two different process overlap: the nickel oxidation and urea oxidation. All the molybdenum-modifeid samples present a lower slope than the non-modified sample with the 30Mo-$Ni(OH)_2$ sample having the lowest value. The 8Mo-$Ni(OH)_2$ and the 20Mo-$Ni(OH)_2$ samples present very similar slope values. The presence of the molybdenum seems to slightly favor the reaction kinetics. and Also in literature it was found that the presence of molybdenum decreases the Tafel slope values[52].

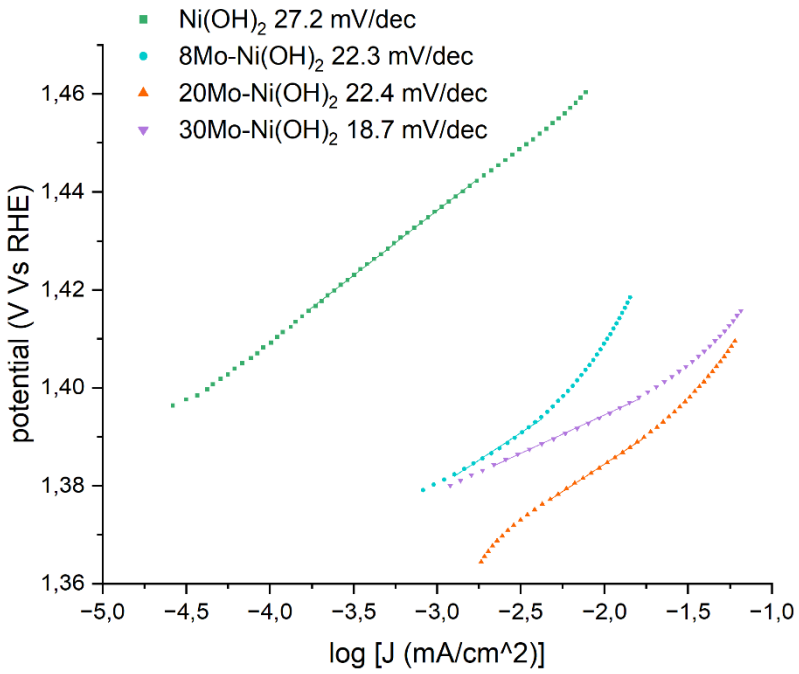

Figure 3.23 Tafel analysis of the LSVs in 0.33 M urea + 1 M KOH reported in Figure 3.18.

Table 3.14 Tafel slope values determined from figure 3.23 for $Ni(OH)_2$ and the three Mo-doped samples .

sample	Tafel slope (mV/dec) (UOR)	Tafel slope (mV/dec) (OER)
$Ni(OH)_2$	27.2	83.5
8Mo-$Ni(OH)_2$	22.3	115.1
20Mo-$Ni(OH)_2$	22.4	118.1
30Mo-$Ni(OH)_2$	18.7	130.8

3.4.3 Comparison between Mn- and Mo-modified samples

The objective of this section is to compare the effect of the two metals studied. With this aim, the best catalyst of the manganese and molybdenum series are compare to the pristine $Ni(OH)_2$.

Regarding the OER (absence of urea) the three CVs of the three samples discussed in this paragraph are reported in figure 3.24. The two metals introduced in the samples have different effects: the Manganese seems to increase the activity since higher current densities are reached meanwhile the molybdenum-modified sample show similar results to the pristine sample. The main effect of the foreign metals is to shift the nickel oxidation peak towards lower potentials this do not influence the OER activity but is highly beneficial for the urea oxidation reaction. As already mentioned the active species for the UOR is the Ni^{3+} species, shifting the nickel oxidation peak towards lower potentials means having active species at lower potentials. Both the modified samples show a Nickel oxidation peak at lower potentials respect to the non-modified sample but the 20Mo-$Ni(OH)_2$ presents the highest shift.

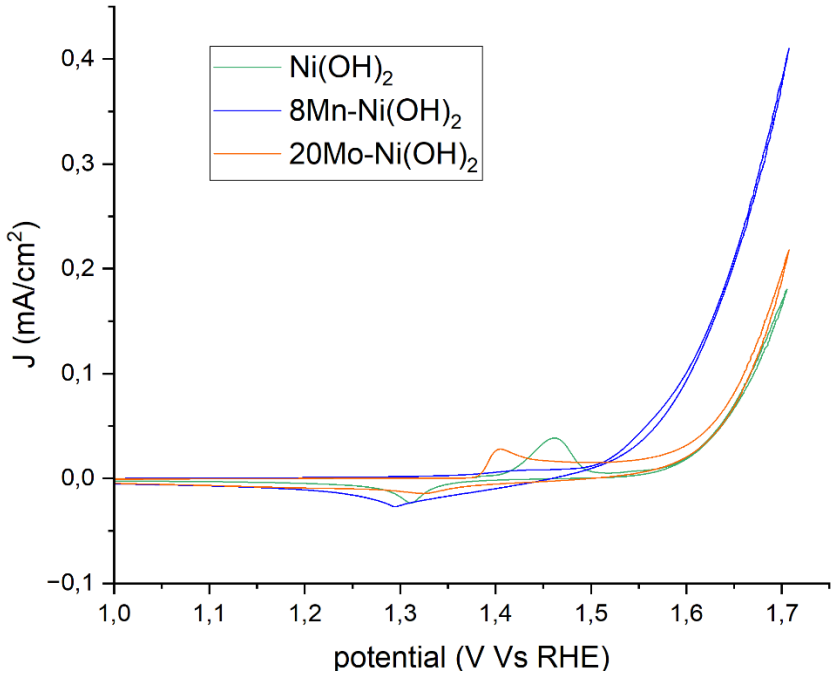

Figure 3.24 Cvs of the $Ni(OH)_2$, the 20Mo-$Ni(OH)_2$ and 8Mn-$Ni(OH)_2$ samples in the absence of urea.

Regarding the UOR (presence of urea), the LSVs of the three sample in presence of urea are reported in figure 3.25. Both the modified materials show higher activity than the non-modified sample since they reach higher current densities and they are also clearly shifted towards lower potentials. This is due to the fact that the nickel oxidation peak of the two modified samples is shifted towards lower potentials in respect to the non-modified sample. Between the two modified samples the most active one is clearly the 20Mo-$Ni(OH)_2$ sample since it reaches higher current densities and the curve is slightly shifted towards lower potentials as demonstrated by the on-set values present in table 3.10 and table 3.13: 1.40 V for the 8Mn-$Ni(OH)_2$ sample and 1.38 V for the 8Mn-$Ni(OH)_2$ sample.

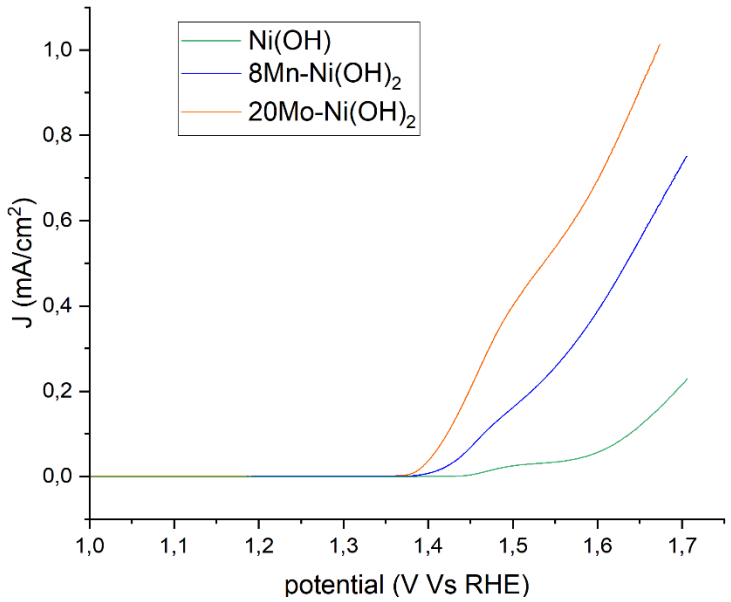

Figure 3.25 LSVs of the $Ni(OH)_2$, the 20Mo-$Ni(OH)_2$ and 8Mn-$Ni(OH)_2$ samples in presence of urea

3.5 Conclusions

Nickel hydroxide and their derivatives with manganese or molybdenum were synthesized with a novel and cost effective method in collaboration with Circular Materials s.r.l. They were subsequently characterized by SEM-EDX, ICP, XRD, XAS, and XPS to determine their morphological, structural and chemical properties, and tested as electrocatalysts for the urea oxidation reaction (UOR).

The morphological characterization carried out by SEM showed that the size and shape of the particles depended only on the synthesis method, and that the addition of a second metal did not have any effect on them. All the materials presented a wide particle size distribution, from hundreds of nm to hundreds of μm, and the particles did not have a defined shape. On the other hand, this synthesis method allowed the introduction of a second metal (Mn-$Ni(OH)_2$ or Mo-$Ni(OH)_2$) in the desired concentration, as confirmed by SEM-EDX and ICP.

The structural and chemical characterization revealed that, in the case of the Mn-doped $Ni(OH)_2$ samples, all the manganese was introduced into the β-hydroxide structure as dopant, since no separated phases of Mn were detected. Mn^{3+} ions substitute Ni^{2+} ions in the hydroxide structure resulting in an excess of positive charge, which originates the intercalation of anions in the interlayers. The presence of Mn^{3+} ions with a smaller ionic radius than the Ni^{2+} ones generates the contraction of the cell lattice, as observed both by XRD and XAS. At the surface of the particles, the manganese ions are oxidized to Mn^{4+}, probably MnO_2, due to the contact with the air. The case of the Mo-modified $Ni(OH)_2$ samples was more complex. Only a small part of the molybdenum entered the β-$Ni(OH)_2$ structure as dopant, while the rest of Mo tend to form MoO_3 and $NiMoO_4$ as separated phases. As expected, the amount of these separated phases increased with the amount of Mo used in the synthesis. The average oxidation state of the molybdenum ions was close to +6.

Finally, all the materials were tested as UOR electrocatalysts. First, measurements were conducted in absence of urea. In these conditions, the oxygen evolution reaction takes place on the catalysts, therefore, it was possible to study the activity of the metal-modified hydroxides, as well as the effect of the second metal, also in this reaction. In the case of the manganese-based catalysts, a clear increase in the OER activity was observed with the amount of Mn. However, only the catalyst with the highest Mn content showed a better performance than the un-doped material. Similarly, the addition of molybdenum did not have any effect on the OER catalytic activity. The performance of these catalysts was very similar to that of the un-doped hydroxide. In presence of urea, however, the results were very different. For the Mn-based hydroxides, the UOR activity increased with the amount of Mn and all the doped-catalysts performed much better than the un-doped one. The addition of molybdenum also increased the UOR activity, both in terms of current densities and onset potential, respect to the un-doped hydroxide. In this case, a significant increase of the catalytic activity was observed when the amount of Mo increased from 8 at.% to 20 at.%, which could be attributed to the presence of $NiMoO_4$ and or MoO_3 in the last one. In the literature, $NiMoO_4$ has been proved to be a promising UOR catalyst, while MoO_3 has been added to transition metal hydroxides to increase their activity. Therefore, a synergetic effect of $Ni(OH)_2$ and $NiMoO_4$ and/or MoO_3 could explain the good performance of this catalyst. On the other hand, when the amount of Mo increased up to 30 at.%, the catalytic activity decreased. This could be due to an excessive amount of MoO_3 in the material, which is not very active.

Bibliography

1. Jiang, L. *et al.* Mo propellant boosting the activity of Ni-P for efficient urea-assisted water electrolysis of hydrogen evolution. *Journal of Colloid and Interface Science* **622**, 192–201 (2022).
2. Li, J. *et al.* An efficient heterogeneous Ni/Ni $_2$ P catalyst for urea-assisted water electrolysis. *Chem. Commun.* **58**, 9552–9555 (2022).
3. Zhu, B., Liang, Z. & Zou, R. Designing Advanced Catalysts for Energy Conversion Based on Urea Oxidation Reaction. *Small* **16**, 1906133 (2020).
4. Wu, N. *et al.* Nickel/nickel oxide nanocrystal nitrogen-doped carbon composites as efficient electrocatalysts for urea oxidation. *Journal of Alloys and Compounds* **870**, 159408 (2021).
5. Sayed, E. T. *et al.* Synthesis and performance evaluation of various metal chalcogenides as active anodes for direct urea fuel cells. *Renewable and Sustainable Energy Reviews* **150**, 111470 (2021).
6. Zhong, M., Li, W., Wang, C. & Lu, X. Synthesis of hierarchical nickel sulfide nanotubes for highly efficient electrocatalytic urea oxidation. *Applied Surface Science* **575**, 151708 (2022).
7. Ma, Y., Ma, C., Wang, Y. & Wang, K. Advanced Nickel-Based Catalysts for Urea Oxidation Reaction: Challenges and Developments. *Catalysts* **12**, 337 (2022).
8. Singh, R. K., Rajavelu, K., Montag, M. & Schechter, A. Advances in Catalytic Electrooxidation of Urea: A Review. *Energy Tech* **9**, 2100017 (2021).
9. Maheskumar, V., Saravanakumar, K., Govindan, J. & Park, C. M. Rational design of double perovskite La2Ni0.5Co0.5MnO6 decorated polyaniline array on MoO3 nanobelts with strong heterointerface boosting oxygen evolution reaction and urea oxidation. *Applied Surface Science* **612**, 155737 (2023).
10. Li, Y. *et al.* Spin State Tuning of the Octahedral Sites in Ni–Co-Based Spinel toward Highly Efficient Urea Oxidation Reaction. *J. Phys. Chem. C* **125**, 9190–9199 (2021).
11. Zhao, X. *et al.* Hollow spherical LaNiO3 perovskite with superior multifunctional performances and durability for urea-assisted Zn-air batteries. *Applied Surface Science* **637**, 157898 (2023).
12. Xu, S. *et al.* Transition Metal-Based Catalysts for Urea Oxidation Reaction (UOR): Catalyst Design Strategies, Applications, and Future Perspectives. *Adv Funct Materials* **34**, 2313309 (2024).
13. Li, J., Wang, S., Chang, J. & Feng, L. A review of Ni based powder catalyst for urea oxidation in assisting water splitting reaction. *Advanced Powder Materials* **1**, 100030 (2022).
14. Xie, C. *et al.* Insight into the design of defect electrocatalysts: From electronic structure to adsorption energy. *Materials Today* **31**, 47–68 (2019).
15. Tatarchuk, S. W., Choueiri, R. M., Medvedeva, X. V., Chen, L. D. & Klinkova, A. Inductive effects in cobalt-doped nickel hydroxide electronic structure facilitating urea electrooxidation. *Chemosphere* **279**, 130550 (2021).
16. Wang, Q. *et al.* Mo-doped Ni $_2$ P hollow nanostructures: highly efficient and durable bifunctional electrocatalysts for alkaline water splitting. *J. Mater. Chem. A* **7**, 7636–7643 (2019).
17. Man, H.-W. *et al.* Transition metal-doped nickel phosphide nanoparticles as electro- and photocatalysts for hydrogen generation reactions. *Applied Catalysis B: Environmental* **242**, 186–193 (2019).
18. Zhang, H., Xi, B., Gu, Y., Chen, W. & Xiong, S. Interface engineering and heterometal doping Mo-NiS/Ni(OH)2 for overall water splitting. *Nano Res.* **14**, 3466–3473 (2021).
19. Dong, L., Chu, Y. & Sun, W. Controllable Synthesis of Nickel Hydroxide and Porous Nickel Oxide Nanostructures with Different Morphologies. *Chemistry A European J* **14**, 5064–5072 (2008).
20. Tang, Y. *et al.* Hydrothermal synthesis of a flower-like nano-nickel hydroxide for high performance supercapacitors. *Electrochimica Acta* **123**, 158–166 (2014).
21. McEwen, R. S. Crystallographic studies on nickel hydroxide and the higher nickel oxides. *J. Phys. Chem.* **75**, 1782–1789 (1971).
22. Song, Q., Tang, Z., Guo, H. & Chan, S. L. I. Structural characteristics of nickel hydroxide synthesized by a chemical precipitation route under different pH values. *Journal of Power Sources* **112**, 428–434 (2002).

23. Hall, D. S., Lockwood, D. J., Bock, C. & MacDougall, B. R. Nickel hydroxides and related materials: a review of their structures, synthesis and properties. *Proc. R. Soc. A.* **471**, 20140792 (2015).
24. Hall, D. S., Lockwood, D. J., Poirier, S., Bock, C. & MacDougall, B. R. Raman and Infrared Spectroscopy of α and β Phases of Thin Nickel Hydroxide Films Electrochemically Formed on Nickel. *J. Phys. Chem. A* **116**, 6771–6784 (2012).
25. Ramesh, T. N. & Vishnu Kamath, P. The effect of 'crystallinity' and structural disorder on the electrochemical performance of substituted nickel hydroxide electrodes. *J Solid State Electrochem* **13**, 763–771 (2009).
26. Tessier, C., Haumesser, P. H., Bernard, P. & Delmas, C. The Structure of Ni (OH) 2: From the Ideal Material to the Electrochemically Active One. *J. Electrochem. Soc.* **146**, 2059–2067 (1999).
27. Tang, T. *et al.* Electronic and Morphological Dual Modulation of Cobalt Carbonate Hydroxides by Mn Doping toward Highly Efficient and Stable Bifunctional Electrocatalysts for Overall Water Splitting. *J. Am. Chem. Soc.* **139**, 8320–8328 (2017).
28. Mahala, C., Devi Sharma, M. & Basu, M. Fe-Doped Nickel Hydroxide/Nickel Oxyhydroxide Function as an Efficient Catalyst for the Oxygen Evolution Reaction. *ChemElectroChem* **6**, 3488–3498 (2019).
29. Zhang, Z. *et al.* Stacking fault disorder induced by Mn doping in Ni(OH)2 for supercapacitor electrodes. *Chemical Engineering Journal* **412**, 128617 (2021).
30. Yin, T.-T. *et al.* Mn-Incorporation-Induced Phase Transition in Bottom-Up Synthesized Colloidal Sub-1-nm $Ni(OH)_2$ Nanosheets for Enhanced Oxygen Evolution Catalysis. *Nano Lett.* **23**, 3259–3266 (2023).
31. Biesinger, M. C. *et al.* Resolving surface chemical states in XPS analysis of first row transition metals, oxides and hydroxides: Cr, Mn, Fe, Co and Ni. *Applied Surface Science* **257**, 2717–2730 (2011).
32. Biesinger, M. C., Payne, B. P., Lau, L. W. M., Gerson, A. & Smart, R. St. C. X-ray photoelectron spectroscopic chemical state quantification of mixed nickel metal, oxide and hydroxide systems. *Surface & Interface Analysis* **41**, 324–332 (2009).
33. Chen, J. & Shen, Y. Effects of Manganese Doping into Nickel Hydroxides for the Electrochemical Conversion of KA Oil. *ACS Sustainable Chem. Eng.* **12**, 5907–5916 (2024).
34. Zhang, T., Huang, H., Han, J., Yan, F. & Sun, C. Manganese-Doped Hollow Layered Double (Ni, Co) Hydroxide Microcuboids as an Efficient Electrocatalyst for the Oxygen Evolution Reaction. *ChemElectroChem* **7**, 3852–3858 (2020).
35. Chen, F. *et al.* Electronic structure modulation of nickel hydroxide porous nanowire arrays via manganese doping for urea-assisted energy-efficient hydrogen generation. *Journal of Colloid and Interface Science* **626**, 445–452 (2022).
36. Wang, C. *et al.* Structural engineering and electronic state tuning optimization of molybdenum-doped cobalt hydroxide nanosheet self-assembled hierarchical microtubules for efficient electrocatalytic oxygen evolution. *Journal of Colloid and Interface Science* **628**, 398–406 (2022).
37. Gaidelene, J., Kalendarev, R., Kuzmin, A. & Purans, J. EXAFS study of mixed nickel molybdenum oxide thin films at the Ni and Mo K-edges. *Nuclear Instruments and Methods in Physics Research Section A: Accelerators, Spectrometers, Detectors and Associated Equipment* **531**, 321–326 (2004).
38. Baltrusaitis, J. *et al.* Generalized molybdenum oxide surface chemical state XPS determination via informed amorphous sample model. *Applied Surface Science* **326**, 151–161 (2015).
39. Wei, L. *et al.* High-valence Mo doping for highly promoted water oxidation of NiFe (oxy)hydroxide. *J. Mater. Chem. A* **10**, 23790–23798 (2022).
40. Houng, B., Liu, C. C. & Hung, M. T. Structural, electrical and optical properties of molybdenum-doped TiO2 thin films. *Ceramics International* **39**, 3669–3676 (2013).
41. Patil, R. B., Mantri, A., House, S. D., Yang, J. C. & McKone, J. R. Enhancing the Performance of Ni-Mo Alkaline Hydrogen Evolution Electrocatalysts with Carbon Supports. *ACS Appl. Energy Mater.* **2**, 2524–2533 (2019).
42. Kaliyaraj Selva Kumar, A., Zhang, Y., Li, D. & Compton, R. G. A mini-review: How reliable is the drop casting technique? *Electrochemistry Communications* **121**, 106867 (2020).
43. Elgrishi, N. *et al.* A Practical Beginner's Guide to Cyclic Voltammetry. *J. Chem. Educ.* **95**, 197–206 (2018).

44. Sumboja, A., Chen, J., Zong, Y., Lee, P. S. & Liu, Z. NiMn layered double hydroxides as efficient electrocatalysts for the oxygen evolution reaction and their application in rechargeable Zn–air batteries. *Nanoscale* **9**, 774–780 (2017).
45. Luan, C. *et al.* Structure Effects of 2D Materials on α-Nickel Hydroxide for Oxygen Evolution Reaction. *ACS Nano* **12**, 3875–3885 (2018).
46. Duraivel, M., Nagappan, S., Park, K. H. & Prabakar, K. Optimised Ni^{3+}/Ni^{2+} and Mn^{3+}/Mn^{2+} Ratios in Nickel Manganese Layered Double Hydroxide for Boosting Oxygen and Hydrogen Evolution Reactions. *ChemElectroChem* **9**, e202200822 (2022).
47. Xia, L. *et al. In Situ* Growth of Porous Ultrathin $Ni(OH)_2$ Nanostructures on Nickel Foam: An Efficient and Durable Catalysts for Urea Electrolysis. *ACS Appl. Energy Mater.* **3**, 2996–3004 (2020).
48. Yang, W. *et al.* Ultrathin nickel hydroxide nanosheets with a porous structure for efficient electrocatalytic urea oxidation. *J. Mater. Chem. A* **7**, 26364–26370 (2019).
49. Lu, Z. *et al.* Nickel–Molybdenum-Based Three-Dimensional Nanoarrays for Oxygen Evolution Reaction in Water Splitting. *Molecules* **29**, 3966 (2024).
50. De Castro, I. A. *et al.* Molybdenum Oxides – From Fundamentals to Functionality. *Advanced Materials* **29**, 1701619 (2017).
51. Huang, X., He, R., Wang, S., Yang, Y. & Feng, L. High-Valent Ni Species Induced by Inactive MoO_2 for Efficient Urea Oxidation Reaction. *Inorg. Chem.* **61**, 18318–18324 (2022).
52. Zhang, J.-Y. *et al.* Energy-saving hydrogen production coupling urea oxidation over a bifunctional nickel-molybdenum nanotube array. *Nano Energy* **60**, 894–902 (2019).

CHAPTER 4

Synthesis and characterization of nickel phosphide-based catalysts for the urea oxidation reaction and hydrogen evolution reaction

4.1 Introduction

Electrochemical water splitting technology for hydrogen production has attracted great attention in the global energy field. The large overpotential needed for the oxygen evolution reaction (OER) greatly limits the potential of the electrochemical water splitting technology for hydrogen production[1]. The urea oxidation reaction (UOR) has a much lower thermodynamic oxidation potential (0.37 V) than the OER (1.23 V), for this reason, it is a promising alternative to substitute the OER. Due to the $6e^-$ transfer process, a large overpotential is still required for the UOR and, for this reason, finding active UOR catalysts is of fundamental importance[2]. As anticipated at the beginning of chapter 3, the nickel-based materials are gaining a lot of traction as UOR catalysts due to their low cost, good activity and stability[3–5] . Inspired by urease, low cost Ni-based materials were found to be the most efficient UOR catalysts, which are promising to replace noble metal-based catalysts[6]. Ni-based materials are first oxidized into NiOOH, the active species, and then urea can be either indirectly chemical-oxidized or directly electro-oxidized. The oxidation rate of Ni^{2+} to Ni^{3+} is faster than that of urea oxidation[2]. The Ni^{3+} active sites bind the intermediates or the product, especially CO_2, too strongly, thus prohibiting the catalyzing process[7]. For this reason, the main target for the design of Ni-based catalysts is to facilitate the desorption of products from the active sites. Another important characteristic that the catalyst should have is high electrical conductivity which favors the electron transfer from the electrode to the surface active sites during the UOR process[8]. For these reasons, different Ni-based catalysts have been investigated such as, nickel alloys[9], nickel nitride[10], nickel phosphide[8,11], nickel hydroxide[7,12] and nickel oxide[13]. Nickel hydroxide has gained a lot of attention due to the fact that it is cheap, easy to synthetized and, thanks to the hydrothermal synthesis, it is easy to obtain different morphologies for this material[14]. However, nickel hydroxide has a very low electron conductivity and this limit its wide application. Compared with nickel hydroxide, nickel phosphide has a much higher electrical conductivity, which is beneficial for the UOR process in terms of increased electron transfer[11]. For these reasons, nickel phosphide seems a better alternative than nickel hydroxide, being cheap and easy to synthetized but more conductive. To further improve the electrocatalytic performance of this material, lots of strategies have been developed and employed, such as adjusting the morphology[15], compositing with substrates owning excellent electrical conductivity like carbon materials,[16] and modulating the electronic structure by doping heteroatoms[8]. Introducing a different metal element could effectively modulate some properties of the catalyst, such as morphology features and electronic distribution, optimizing the performance of the catalyst. Jin et al. synthetized a molybdenum-doped nickel phosphide as a water-splitting electrocatalyst[17]. The introduction of the Mo element could generate strong coupling effects and help to expose more active sites, remarkably enhancing the catalytic activity. Yang et al. realized a manganese-doped nickel phosphide catalyst for UOR[11]. The introduction of transition metal Mn can regulate the structure of the material, dramatically improving the electrocatalytic activity of the material. The introduction of manganese in the structure optimizes the electronic structure

and improves the adsorption for OH^-[18]. In this work, seven different nickel phosphide samples were synthetized (table 4.1) starting from the seven nickel hydroxide samples previously discussed. Three nickel phosphide samples are doped with Mn with three different concentrations, while other three samples are modified with Mo. The concentration of Mn and Mo are the same described in chapter 3. Finally, one sample is pure nickel phosphide without doping.

Table 4.1 List and nomenclature of the different NiP-based materials synthesized

Name	Dopant	At % M/N (M=Mo, Mn)
NiP	---	
3Mn-NiP	Mn	3
5Mn-NiP	Mn	5
8Mn-NiP	Mn	8
8Mo-NiP	Mo	8
20Mo-NiP	Mo	20
30Mo-NiP	Mo	30

4.2 Synthesis of nickel phosphides

The nickel phosphide-based materials were synthesized starting from the nickel hydroxide based-samples. The objective of this synthesis was to obtain seven samples with the same doping of the starting samples. For that, a tubular oven, where a phosphorus precursor was inserted together with the hydroxide sample, was used. The agent utilized for the phosphorization was sodium hypophosphite (NaH_2PO_2). The decomposition reaction starts around 100°C and ends at 250 °C[19].

$$2NaH_2PO_2 \xrightarrow{\Delta} PH_3 + Na_2HPO_4$$

The products of the reaction are sodium hydrogen phosphate (Na_2HPO_4) and phosphine (PH_3), the latter is the molecule that reacts with the hydroxide samples and phosphorizes them. Phosphine can be lethal if ingested (H-300) and in gas form is highly dangerous for the airways[19]. For these reasons, it was necessary to keep the reaction inside the tubular oven and under nitrogen flow. To neutralize the phosphine gas at the exit of the oven, a glass bubbler with mineral oil and another one with a sodium hypochlorite solution ($NaOCl$), which reacts with phosphine to form hypophosphorous acid (H_3PO_2) and sodium chloride($NaCl$), were placed.

$$PH_3 + 2NaOCl \rightarrow H_3PO_2 + NaCl$$

The quartz tube where the samples were put inside was washed after every synthesis to eliminate eventual impurities. The reaction was carried out in nitrogen flow to avoid the presence of oxygen in the oven that would lead to the formation of nickel oxide. For every synthesis, around 20 mg of nickel hydroxide sample were inserted into an alumina boat that was then placed at the center of the oven. Then, around 110 mg of precursor were inserted into an alumina boat that was placed at about 7 cm from the center of the oven. The heating ramp was of 3°C/minute, a slow ramp was chosen to not consume the precursor too quickly. Then the 300°C temperature was kept for two hours. During all these steps, the gas flow was kept at 70 SCCM. More details on the procedure used for the synthesis is present on chapter 2. Since nitrogen is the gas carrier for the phosphine, it was important to maintain a slow flow to let the phosphine react with the nickel

hydroxide. Since this reaction happens at the surface, it is important to let enough time for the phosphine to also penetrate inside the sample and react with the inner layers. In this case, it would be helpful to have very small particles to make the reaction easier. The ball milling treatment of the nickel hydroxide samples done to break the bigger particles in smaller ones revealed to be helpful also for this step of the thesis work.

4.3 Physio-chemical characterization

The synthetized hydroxides were characterize using X-ray diffraction, X-ray photoelectron spectroscopy and scanning electron microscopy. These techniques were described in chapter 2.

4.3.1 Mn-doped nickel phosphides

The morphology of the synthetized phosphides was investigated by scanning electron microscopy (SEM). The images reported in Figure 4.1. evidence the presence of particles with a wide range of dimensions and with no specific shape. The particles went from hundreds of nanometers to hundreds of micrometers. Most of the particles were around tens of micrometers but in every sample at least a big particle with dimensions over 100 micrometers was found. To evaluate the elemental composition of the particles, and to verify the absence of contaminants, EDX analysis was performed.

The nickel phosphide-based materials were obtained starting from the nickel hydroxide-based materials. For this reason the samples in figure 4.1 present similar dimensions to the nickel-based materials in figure 3.2. The thermal treatment did not have any effect on the dimension of the particles it only converted the nickel hydroxide in nickel phosphide. The phosphides present bigger particles encircled by smaller particles while the nickel hydroxide-based materials presented singular particles with a layered structure. The presence of a second metal did not have any effect on the morphology or the dimensions of the particles.

EDX measurements were done to determine the composition of the samples and the metals ratio. These measurements, together with XRD, were important to understand if the phosphorization occurred. The measurements were taken from different spots of the sample: at least three images were taken for each sample and from them at least three spots were measured by EDX.

Table 4.2 reports the atomic composition obtained by EDX measurements as well as the Mn:Ni ratio. No contaminations were found. In some cases, the EDX showed the presence of carbon, which is attributed to the fact that the samples were deposited on carbon tape and also that they were exposed to the atmosphere. The value obtained describe the total amount of manganese in the sample so even the manganese atoms that were not incorporated into the NiP structure are counted in this measurement. All the values of Mn:Ni ratio are close to those of the corresponding hydroxides. Another important thing is that the atomic concentration of Nickel is around two times the atomic concentration of the phosphorous, this is a sign that the Ni_2P phase could be present in the sample. This hypothesis will be further discussed in the next paragraph.

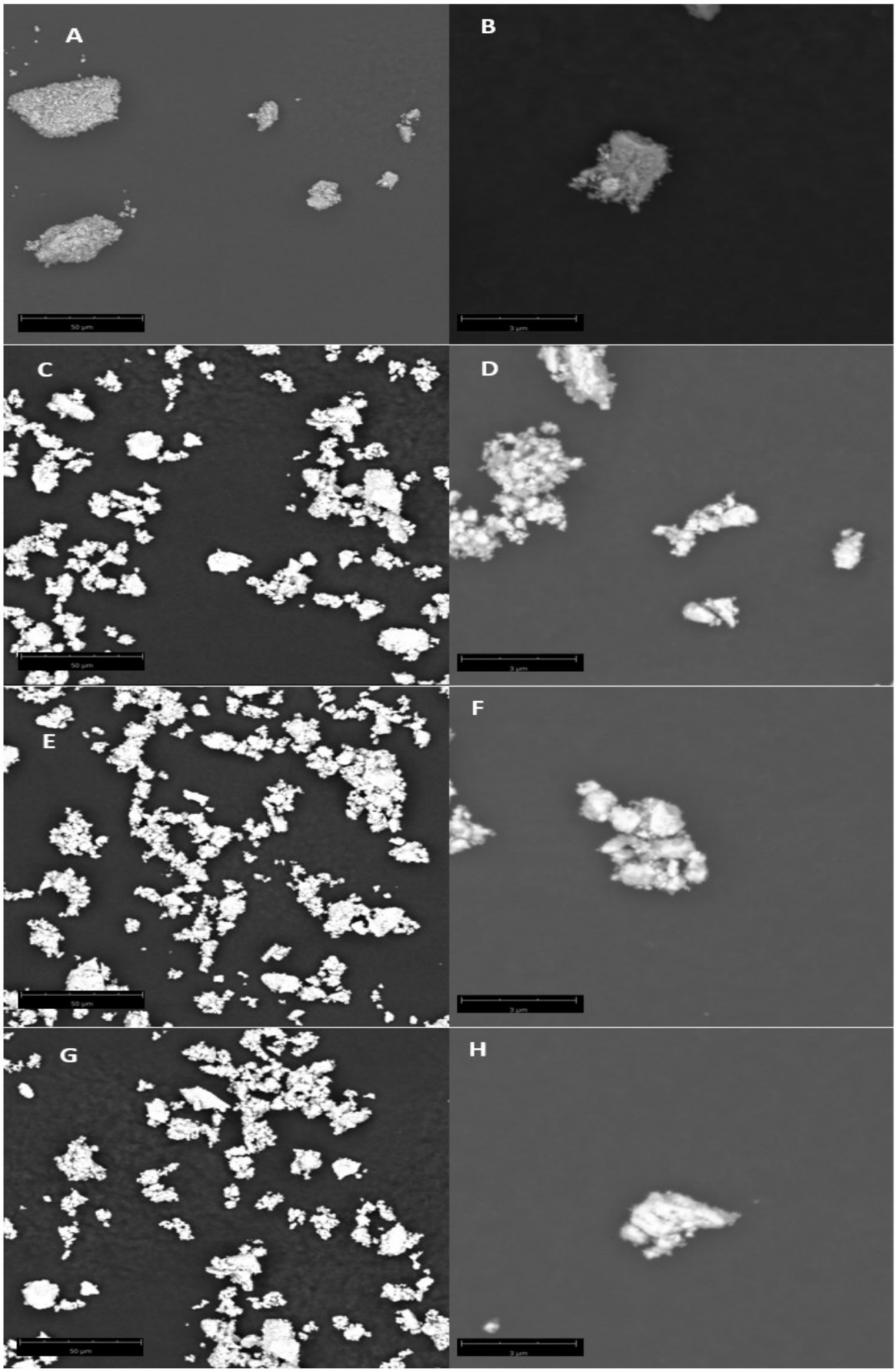

Figure 4.1 SEM images of NiP sample (A and B), 3Mn-NiP (C and D), 5Mn-NiP (E and F), and 8Mn-NiP (G and H). The scale bar of the left images is 50 µm, while the one of the right images is 3 µm.

Table 4.2 atomic concentration of Ni, O, P and Mn from EDX measurements. the Mn:Ni ratio is also reported.

Sample	Ni (at.%)	O (at.%)	Mn (at.%)	P (at%)	Atomic Mn:Ni ratio[a]
NiP	23.8	65.2	/	11	/
3Mn-NiP	18.8	72.4	0.5	8.3	2.6
5Mn-NiP	18.1	73.1	0.8	8.0	4.4
8Mn-NiP	15.8	75.7	1.2	7.3	7.6

The powders were analyzed by X-ray diffraction to determine the different phases present in the sample. Ni_2P is the most common phase obtained from the phosphorization of Nickel hydroxides[8,11] but, in some cases, traces of $Ni_{12}P_5$ can be found in the samples[20]. Ni_2P adopts the hexagonal Fe_2P structure[21], figure 4.3, while $Ni_{12}P_5$ has a body-centered tetragonal structure[22], represented in figure 4.4.

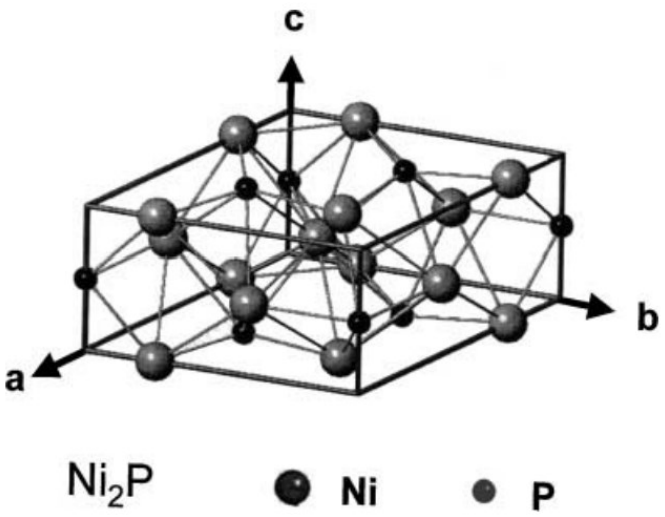

Figure 4.3 crystal structure of Ni_2P. reprinted from [19]

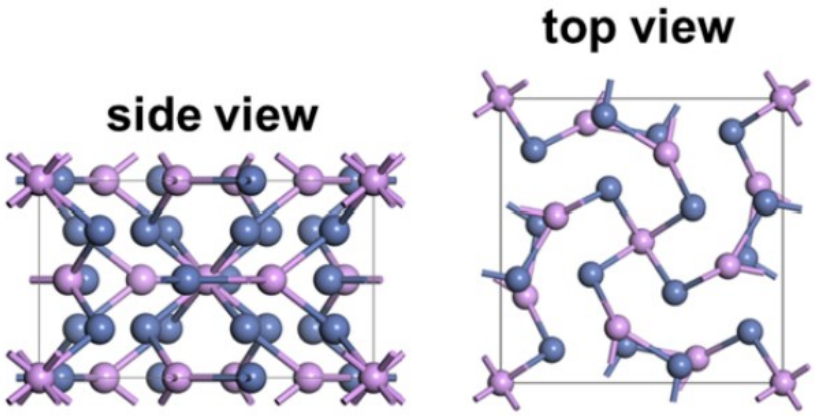

Figure 4.4 crystal structure of $Ni_{12}P_5$ where the pink atoms represent the phosphorus atoms and the blue ones the nickel atoms. Reprinted from [21]

The two phases behave differently as catalyst, it was found in literature that Ni_2P is a better catalyst for the hydrogen evolution reaction having extremely lower overpotential than $Ni_{12}P_5$. This is attributed to a higher concentration of P over Ni species at the surface, which plays an important role in increasing catalytic activity. The P atoms on the surface have a small negative charge to trap protons and remove hydrogen from the

surface[20]. On the other hand, $Ni_{12}P_5$ shows slightly lower overpotential for the oxygen evolution reaction[20]. The superior performance of $Ni_{12}P_5$ for OER is attributed to the formation of a thick amorphous shell of NiOOH/$Ni(OH)_2$ at the surface. Moreover, the higher activity is directly related to the higher amount of nickel on the surface of this amorphous layer in respect to the Ni_2P phase[20]. No information about which of the two phases is more active for the UOR was found. Since we do not know if a higher activity towards the OER translates into a higher activity towards UOR, the nickel phosphide phase that better suit the purpose of this work is the Ni_2P being more active for the HER. Table 4.3 reports the peaks position of the two nickel phosphide phases. For $Ni_{12}P_5$, only the most intense peaks are reported since many peaks have very low intensity and even the most intense peaks of this phase are barely visible in figure 4.5. It is obvious that the low intensity peaks of the reference will not be visible in the measurement and they would only make table 4.3 confusional.

Table 4.3 miller indices of the two different nickel phosphide phases. The values are obtained from High score plus database and for the $Ni_{12}P_5$ phase only the most intense peaks are reported since in the reference are listed an high number of peaks with very low intensity.

Ni_2P		$Ni_{12}P$	
Miller indices (hkl)	2θ (°)	Miller indices (hkl)	2θ (°)
(110)	30.5	(200)	23.3
(101)	31.8	(211)	25.2
(200)	35.4	(310)	32.7
(111)	40.7	(112)	38.4
(201)	44.6	(400)	41.8
(210)	47.4	(330)	44.4
(300)	52.2	(240)	46.9
(002)	54.1	(312)	49.0
(211)	54.9	(642)	90.8
(112)	66.4	(244)	93.2
(311)	72.7	(811)	94.5
(400)	74.8		
(401)	80.2		
(103)	88.8		

The XRD patterns of the four samples are depicted in figure 4.5. All the peaks of the Ni_2P phase that are reported in table 4.3 are found in figure 4.5 for every sample, meaning that this is the main phase present in the samples. Only some of the peaks for $Ni_{12}P_5$ are present, the other ones could be overlapped with the much more intense peaks of the Ni_2P phase. In addition, the peaks associated with nickel oxide are found in all the samples. In particular, three peaks around 43°, 63° and 76° that are associated with (200), (220) and (222) (PDF 36-8583) , respectively, are clearly observed. The presence of nickel oxide can be attributed to an incomplete phosphidization of the samples at the center due to the large dimension of some particles. Figure 4.6 reports the Ni_2P(111) peak, where a clear shift towards higher degrees with the amount of Mn is observed. This shift is related to the presence of Mn into the nickel phosphide that causes the structure contraction, since Mn has a smaller ionic radius than Ni.

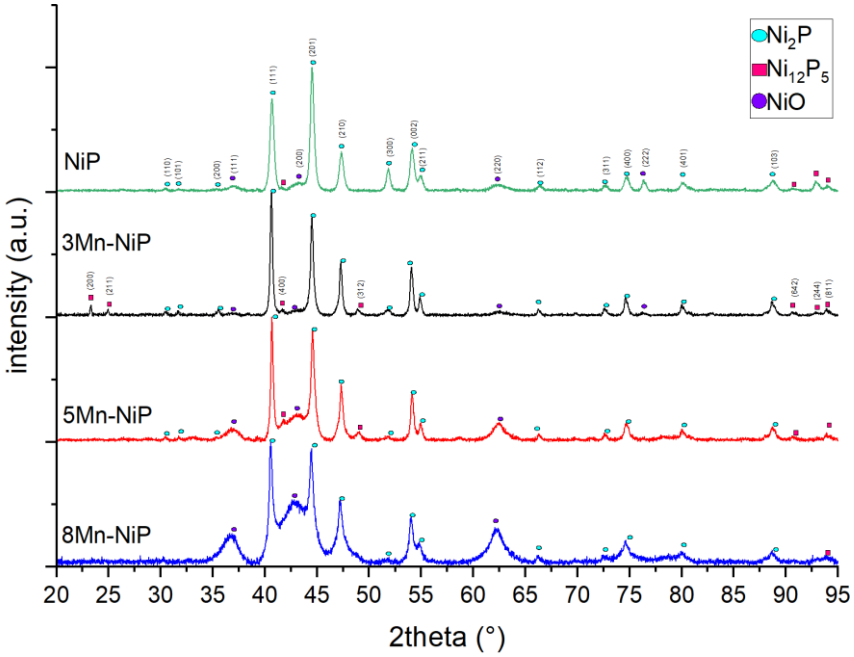

Figure 4.5 XRD patterns of the Mn-modified nickel phosphides samples.

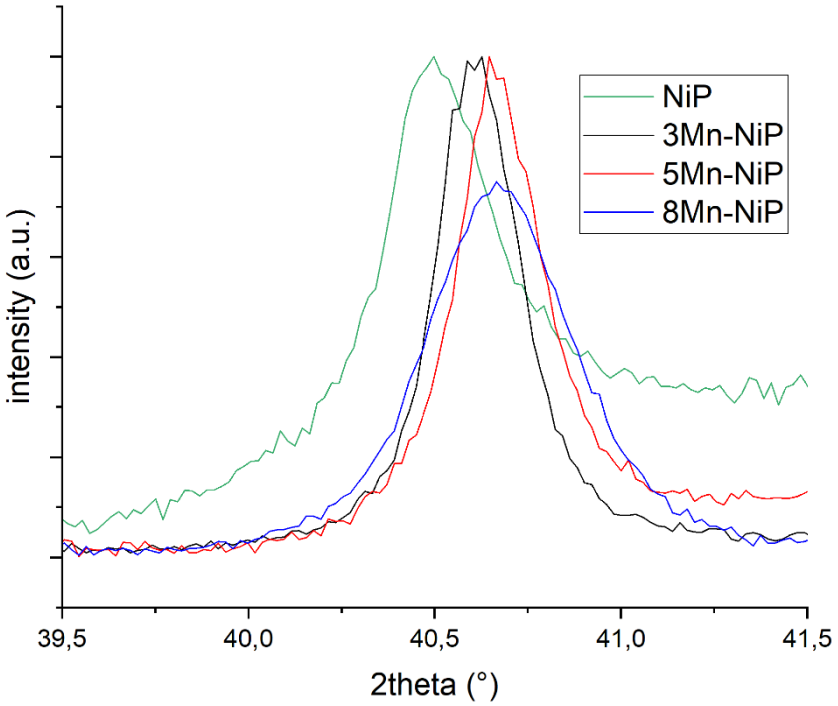

Figure 4.6 detail of the Ni2P(111) peak of the four samples present in figure 4.4.

The peaks width does not change significatively, except for the 8Mn-NiP sample. Table 4.4 reports the values of crystallite dimension that are directly linked to the peaks width. The crystallite size for the 3Mn-NiP and 5Mn-NiP is similar to that of NiP, while the size of 8Mn-NiP is smaller. The crystallite dimensions of these materials are bigger than the one recorded for the hydroxides samples. The high temperatures of the thermal treatment and the slow cooling afterwards helped with the formation of bigger crystallites, this effect is also reported in literature[15].

Table 4.4 Dimension of the crystallites calculated by using the Scherrer equation.

Sample	Crystallite dimension (nm)
NiP	10.1
3Mn-NiP	12.4
5Mn-NiP	12.2
8Mn-NiP	7.5

The samples were also analyzed by X-ray photoelectron emission (XPS) to identify the oxidation state of the species and the composition at the surface. In particular, the O 1s, Ni 2p, Mn 2p and P 2p regions were acquired.

Figure 4.7 shows the Ni $2p_{3/2}$ region for the four samples. As can be seen, the shape of the spectrum is different from the one shown in figure 3.8, where the nickel hydroxides were reported. This is due to the fact that in this case more components are present. Two components were included in the fit, taking into account the results from XRD, nickel phosphide and nickel oxide that should be present at the surface due to the contact with the atmosphere.[23] The component at 852.8 eV is related to nickel phosphides,[8] while NiO presents five peaks. The intensity of the peak at around 852.8 eV is low, confirming that NiO covers the particles surface. However, by confronting the curves of figure 4.7 and the ones of figure 3.8, it is clear the presence of a second component. These samples tend to oxidize easily and since the XPS is a surface technique it is obvious that the nickel phosphide component is much less intense than the oxide component since most of the surface is oxidized.

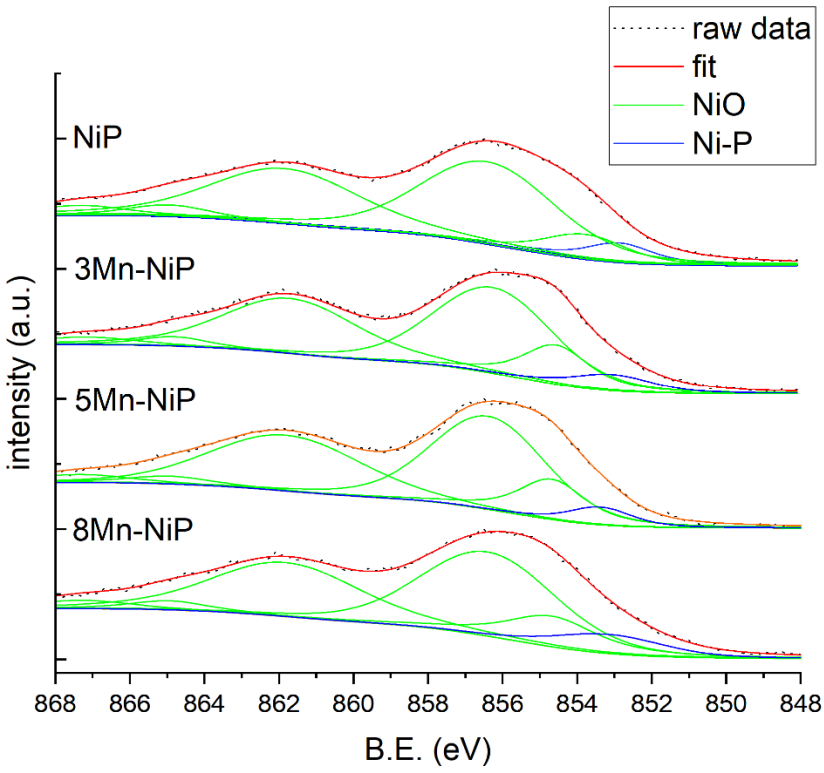

Figure 4.7 Normalized Ni $2p_{3/2}$ XPS region, and separation into chemically shifted components, of the NiP and Mn-modified samples.

Figure 4.8 reports the Mn 2p XPS region of the three manganese-modified samples. From these spectra, it is possible to confirm the presence of manganese since some peaks are visible. However, for the samples with the lowest manganese content, it was not possible to fit the data since they are quite noisy. It is important to remember that the Ni auger peak overlaps with the Mn 2p region, therefore, the error in the fitting could be significant. Results show that only Mn^{4+} is present at the surface, which is probably due to the oxidation of the manganese atoms in contact with the atmosphere. In other works describing manganese-doped nickel phosphides, it was found that the dopant species was Mn^{4+} and in some cases also Mn^{3+} [11,18,24]. XAS measurements would be necessary to determine the oxidation state of Mn in the bulk of the material.

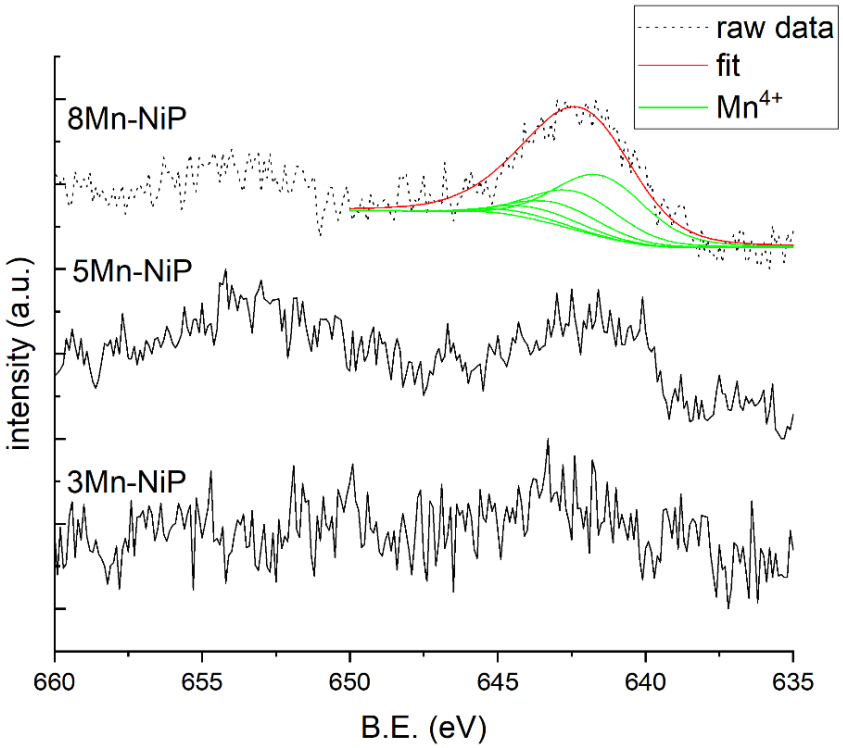

Figure 4.8 Mn 2p XPS region of the three Mn-modified samples. in green are represented the peaks associated with Mn^{4+}

Figure 4.9 reports the P 2p XPS region of the NiP and manganese-modified samples. Two components were used for the fit, one at around 133.7 eV associated with P-O species at the surface of Ni_2P due to the oxidization in air, and one at around 129.8 eV that can be attributed to pure Ni_2P[24]. For all the samples, except 3Mn-NiP, the Ni-P component is much less intense than the P-O one. In the literature, it has been reported that the Ni-P component is usually quite low in intensity, since it is covered by a NiO layer, and that the manganese doping do not affect its position[11,25].

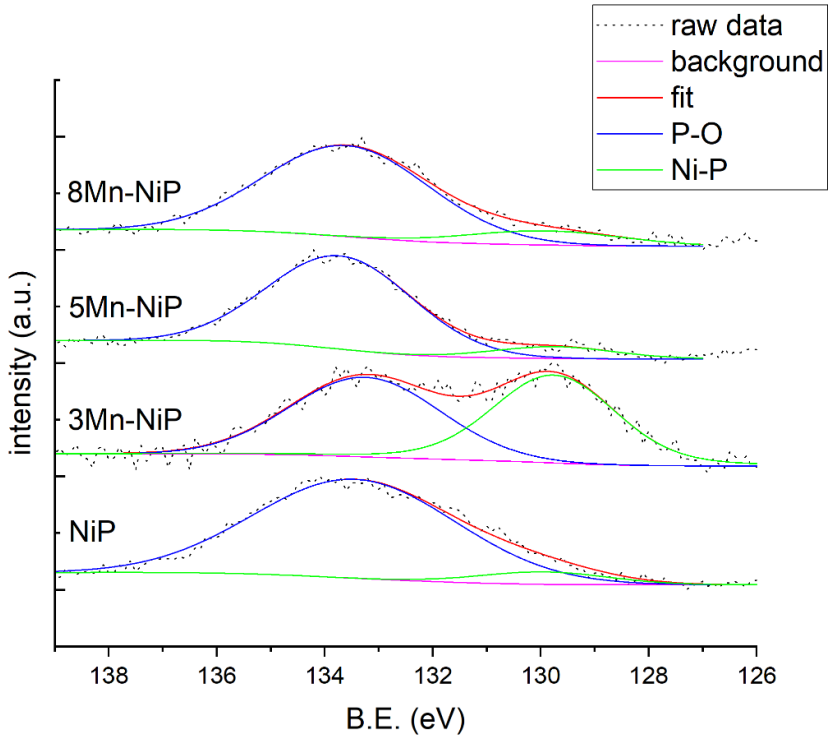

Figure 4.9 P 2p XPS region of the three Mn-modified sample and the NiP sample.

Finally the XPS measurements were used to determinate the surface composition of the modified samples. The values obtained are reported in table 4.5. As can be seen, they are very close to the nominal values, as expected since the same was for the hydroxides samples and the NiP samples were obtained through a thermal treatment of the hydroxides so theoretically there shouldn't be any nickel or manganese loss. The values obtained are very similar to the values obtained for the hydroxides samples (table 3.6). the slightly difference between the sample could be attributed to the fact that even if the total amount of nickel and manganese in the samples is the same the distribution on the surface an in the bulk could be different due to the thermal treatment. Another reason could be that the error in this calculation is quite high.

Table 4.5 Atomic Mn:Ni ratio obtained from XPS measurements

sample	Atomic Mn:Ni ratio (%)
3Mn-NiP	2.8
5Mn-NiP	4.7
8Mn-NiP	7.7

4.3.2 Mo-doped nickel phosphides

The morphology of the synthetized Mo-modified phosphides was also investigated by scanning electron microscopy (SEM). As it was observed for the Mn-doped phosphides, also for these materials the SEM images evidence the presence of particles with a wide range of dimensions and with no defined shape (Figure 4.10), which can again be attributed to the synthesis technique utilized to obtain these materials. The particles went from hundreds of nanometers to hundreds of micrometers. Most of the particles were around tens of micrometers but in every sample at least a big particle with dimensions over 100 micrometers was found. The thermal treatment did effect the particles morphology since the NiP-based samples presents bigger particles encircled by smaller particles, while the $Ni(OH)_2$-based samples presented singular particles with a layered structure. The presence of Mo did not influence the morphology of the sample. Comparing with the Mn-based materials, it can be concluded that the addition of a second metal does not affect the morphology of the particles when this synthesis technique is used. No differences are present between the samples modified with different metals, both in the case of the Mo- and Mn-modified hydroxides a wide range of dimensions is present.

To evaluate the elemental composition of the particles and to verify the absence of contaminants, EDX analysis was performed. It can be seen that, also in this case, the experimental values are very close to those of the corresponding hydroxides (table 4.6). The nickel atomic concentration is approximately twice that of phosphorous atomic concentration as found for the Mn-doped samples.

Table 4.6 atomic concentration of Ni, O, P and Mo obtained from EDX measurements. The metals ratio is also reported

Sample	Ni (at.%)	O (at.%)	Mo (at.%)	P (at%)	Atomic Mo:Ni ratio[a]
NiP	23.8	65.2	/	11	/
8Mo-NiP	19.7	70.2	1.4	8.7	7.1
20Mo-NiP	20.4	66.3	4.0	9.3	19.6
30Mo-NiP	13.4	76.6	3.8	6.2	28.4

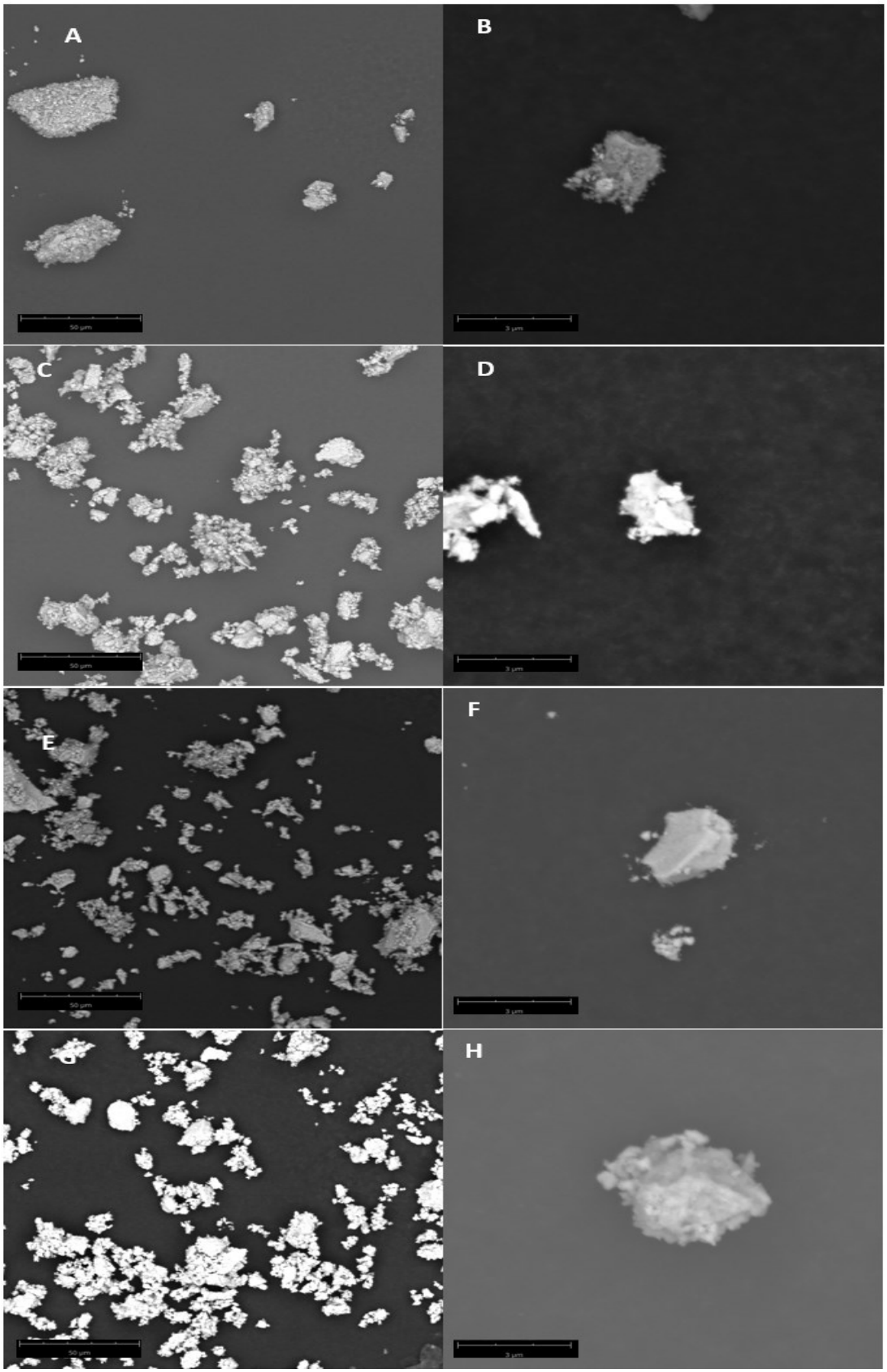

Figure 4.10 SEM images of NiP sample (A and B), 8Mo-NiP (C and D), 20Mo-NiP (E and F), and 30Mo-NiP (G and H). The scale bar of the left images is 50 µm, while the one of the right images is 3 µm.

The powders were analyzed by X-ray diffraction to determine the different phases present in the samples. Figure 4.11 reports the XRD patterns of the molybdenum-modified samples and the nickel phosphide. All the samples show the characteristic peaks of the Ni_2P phase. 30Mo-NiP also shows the (811) peak attributed to the $Ni_{12}P$ phase. However, it can be said that also in this case the main phase present is the Ni_2P one. In the case of the 20Mo-NiP and 30Mo-NiP, no nickel oxide peaks are observed. This is probably due to the fact that this sample presented bigger particles and for this reason it was more difficult for the phosphine to enter inside of them. Only 8Mo-NiP presents four clear peaks at 37.2° (111), 43.1° (200), 62.7° (220) and 76.7° (222) that can be attributed to nickel oxide. All the molybdenum-modified samples show the (101) peak at around 28°, characteristic of molybdenum oxide. This Mo phase was already present in the hydroxide-based samples and remains after the phosphurization treatment. However, the peak's intensity decreases from the 8Mo-NiP sample to the 30Mo-NiP sample, opposite to what observed in figure 3.12 for the corresponding hydroxides. No molybdenum phosphide peaks are present. No peak shift with the presence of Mo is observed in agreement with the results reported in the literature,[8] as highlighted by figure 4.12. This is probably due to the fact that Mo^{6+} and Ni^{2+} have very similar ionic radius, 0.65 Å and 0.69 Å, respectively. The peaks of the molybdenum-modified samples are slightly wider than the non-modified sample. This is confirmed by the results of table 4.7, where the crystallite dimensions for the NiP and the molybdenum-modified samples. No particular trend is observed but all the molybdenum-modified samples present a smaller crystallite size respect to the pure sample.

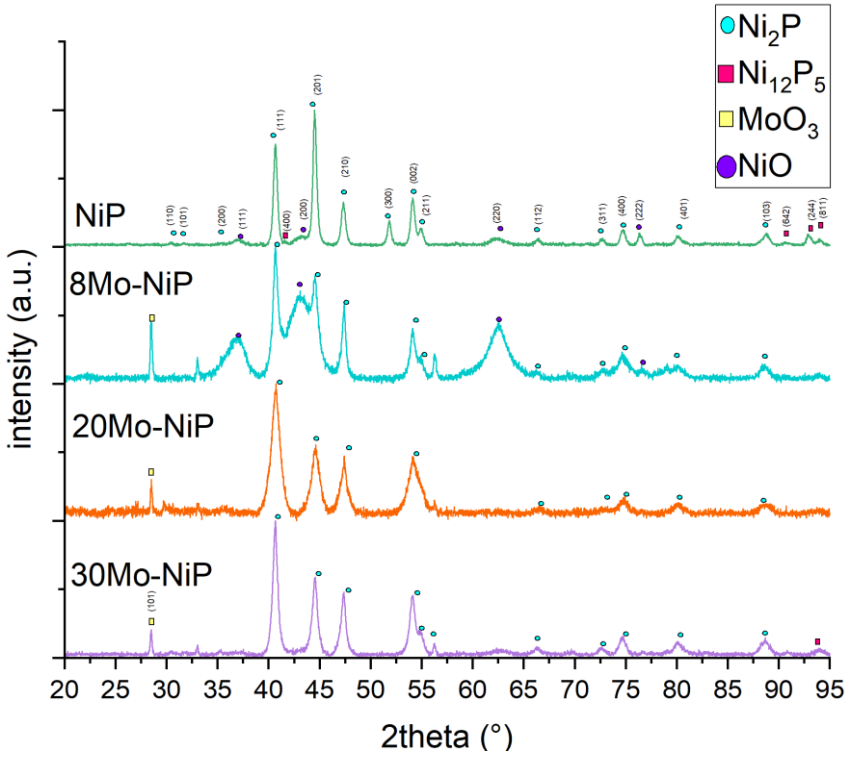

Figure 4.11 XRD patterns of the Mo-modified nickel phosphides. Different symbols are used to identify the peaks associated with different phases.

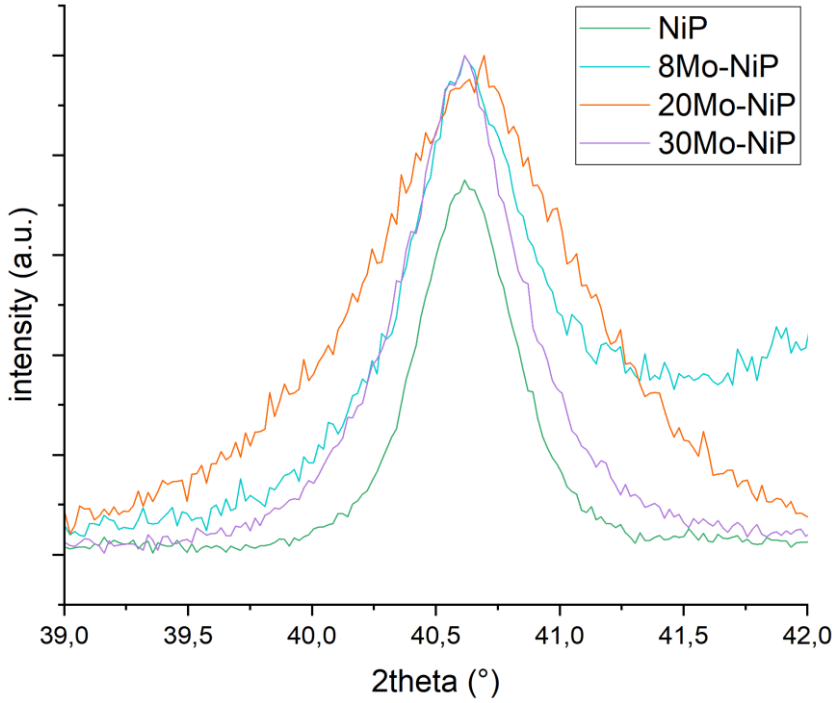

Figure 4.12 Detail of the $Ni_2P(111)$ peak of the four samples present in figure 4.9.

Table 4.7 Crystallite dimensions of the samples reported in figure 4.9

sample	Crystallite dimension (nm)
NiP	10.1
8Mo-NiP	7.4
20Mo-NiP	5.3
30Mo-NiP	8.5

The samples were also analyzed by X-ray photoelectron emission (XPS) to determine the oxidation state of the species and the composition at the surface. The O 1s, Ni 2p, P 2p and Mo 3d regions were acquired. The Ni $2p_{3/2}$ XPS region of the molybdenum-modified and the pure sample is reported in figure 4.13. The data were fitted using the nickel oxide and nickel phosphide components[23] at 854.7 eV and 852.8 eV, respectively[25]. As observed for the Mn-based phosphides, the intensity of the Ni-P component is lower than that of the NiO, indicating that a layer of NiO covers the surface of the nickel phosphide particles due to the contact with the atmosphere.

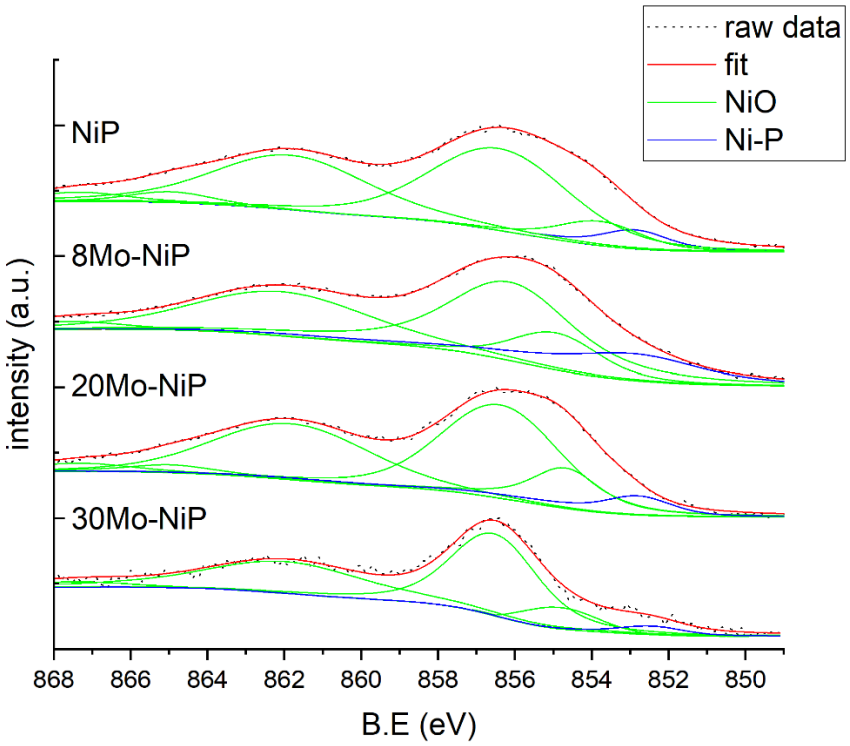

Figure 4.13 Ni $2p_{3/2}$ XPS region, and separation into chemically shifted components, of NiP and the Mo-modified samples.

Figure 4.14 shows the Mo 3d XPS region of the Mo-modified samples. The data were deconvoluted using two peaks at 231.9 eV and 235.3 eV, associated to the Mo $3d_{5/2}$ and Mo $3d_{5/2}$ of Mo^{6+}, respectively[26]. In the literature, for molybdenum-doped nickel phosphides, it has been reported that Mo^{6+} are the doping species,[11,17,26] although other works state that it is Mo^{5+}.[27]

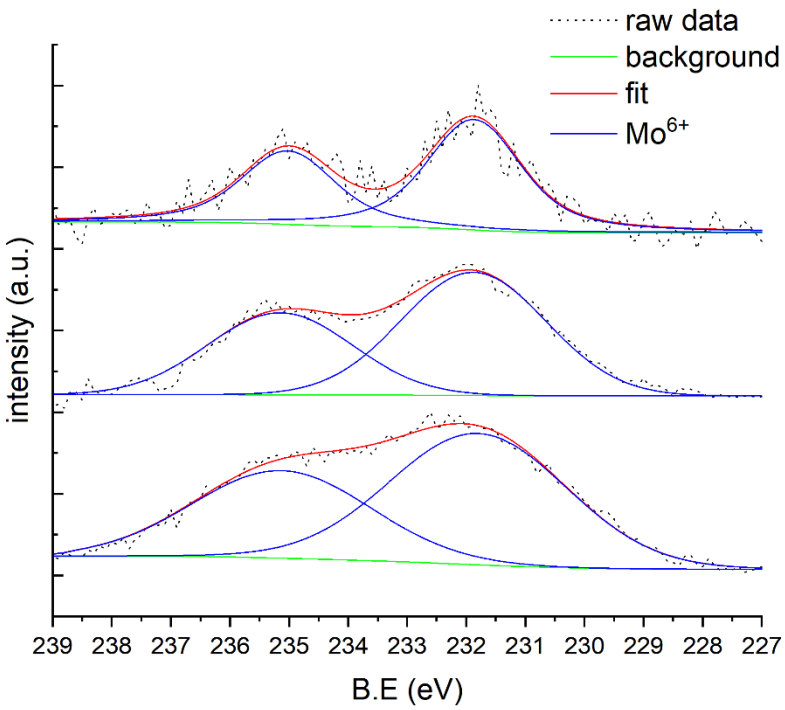

Figure 4.14 Mo 3d XPS region, and separation into chemically shifted components, of the Mo-modified samples.

The P 2p XPS region is reported in figure 4.15. As for the manganese-modified samples, two components at around 133.7 eV, associated with the presence of P-O species at the particles surface, and at around 129.8 eV, attributed to pure Ni_2P, are observed.[22] Also in this case, the intensity of the Ni-P component is much lower than that of the P-O one, suggesting that the P atoms at the surface are oxidized in contact with the atmosphere. it was been reported in literature that the Ni-P component is quite low in intensity, and that the presence of molybdenum do not affect the binding energy.[26,27]

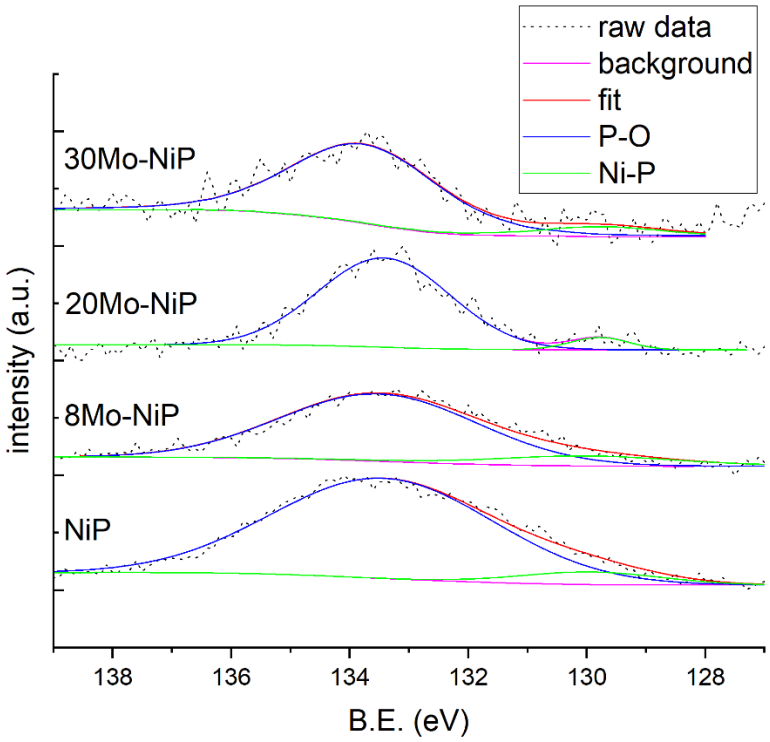

Figure 4.15 P 2p XPS region of the three Mo-modified sample and the NiP sample

Finally the XPS measurements were used to determinate the surface composition of the modified samples. The values obtained are reported in table 4.8. As can be seen, they are not close to the nominal values, as expected since the same was for the hydroxides samples and the NiP samples were obtained through a thermal treatment of the hydroxides so theoretically there shouldn't be any nickel or molybdenum loss. The values obtained are slightly higher than the values obtained for the hydroxides samples (table 3.8). The slightly difference between the sample could be attributed to the fact that the distribution on the surface an in the bulk could be different due to the thermal treatment. Another reason could be that the error in this calculation is quite high. The Mo:Ni ratio in the surface determined by XPS is lower than the nominal one and that determined by EDX. This indicates a Ni segregation from the bulk to the surface.

Table 4.8 Atomic Mn:Ni ratio obtained from XPS measurements

sample	Atomic Mo:Ni ratio (%)
8Mo-$Ni(OH)_2$	3.1
20Mo-$Ni(OH)_2$	8.7
30Mo-$Ni(OH)_2$	19.5

4.4 Urea oxidation reaction (UOR)

The Mn- and Mo-modified samples, as well as NiP, were tested as UOR catalysts and the results are discussed in the following. All potential values are referred to reversible hydrogen electrode (RHE), meanwhile the current values were normalized both for the geometric area and the electroactive area of the electrode and corrected for the ohmic drop of the electrolyte solution.

4.4.1 Mn-doped nickel phosphides

First, the samples were tested in absence of urea to determine the electrochemical surface area (ECSA) and the Ni^{2+}/Ni^{3+} redox potential (see the details in Chapter 2). Figure 4.16 reports the CVs for all the samples. All the CVs present an oxidation peak between 1.4 and 1.5V, related to the oxidation of the Ni^{2+} (Ni_2P or NiO) species to Ni^{3+} (NiOOH), and the corresponding reduction one at around 1.3 V.

The oxidation current observed at potentials higher than 1.6 V is associated with the oxygen evolution reaction (OER), which is a catalytic reaction. The Ni^{2+}/Ni^{3+} redox peaks overlap with the beginning of the OER, making difficult the accurate determination of the OER onset potential. To study the effect of the addition and amount of manganese on the OER activity of the nickel phosphides-based catalysts, the current was first normalized by the geometric area of the electrode (figure 4.16a). 3Mn-NiP and 8Mn-NiP exhibit higher current densities than the non-modified sample, while the 5Mn-NiP sample shows slightly lower current densities than the pure sample. As it was done for the nickel hydroxides samples, the data was normalized by the electro active area since the electrode was prepared by drop casting and resulting in a significant error in the amount of material deposited. Normalizing by the ECSA can help to solve this problem since the value is directly correlated to the amount of available Ni sites (Figure 4.16b). The activity in terms of current density seems to increase with the amount of manganese. The exception is the 5Mn-NiP sample that reaches lower currents respect to the non-modified sample. The on-set potential seems to decrease with the amount of manganese. The sample with the highest amount of Mn shows a significant better performance than the other samples.

Table 4.9 position of the oxidation peaks and reduction peaks of the sample present in figure 4.14. it's reported the distance between the two peaks in mV

sample	Oxidation peak (V)	Reduction peak (V)	Peak separation (mV)
NiP	1.45	1.31	140
3Mn-NiP	1.45	1.32	130
5Mn-NiP	1.44	1.32	120
8Mn-NiP	1.42	1.34	80

Table 4.9 reports the position of the Ni^{2+}/Ni^{3+} and Ni^{3+}/Ni^{2+} redox peaks and the peak separation. It is clear how the presence of manganese in the sample helps to shift the oxidation peak towards lower values respect to the non-modified sample, meaning that it is easier to produce Ni^{3+}, which is the active species for urea oxidation reaction. The shift of the peak increases with the manganese content. The peak separation is an indicator of the electronic conductivity of the material, the lower the separation the higher the conductivity[28] . The peak separation of the samples decreases with the amount of manganese introduced in the sample, indicating that the presence of Mn increases the electrical conductivity of the material and, therefore, favors

the electron transfer during the catalytic reactions. The increase of the OER activity with the introduction of manganese has already been described in the literature.[11,24]

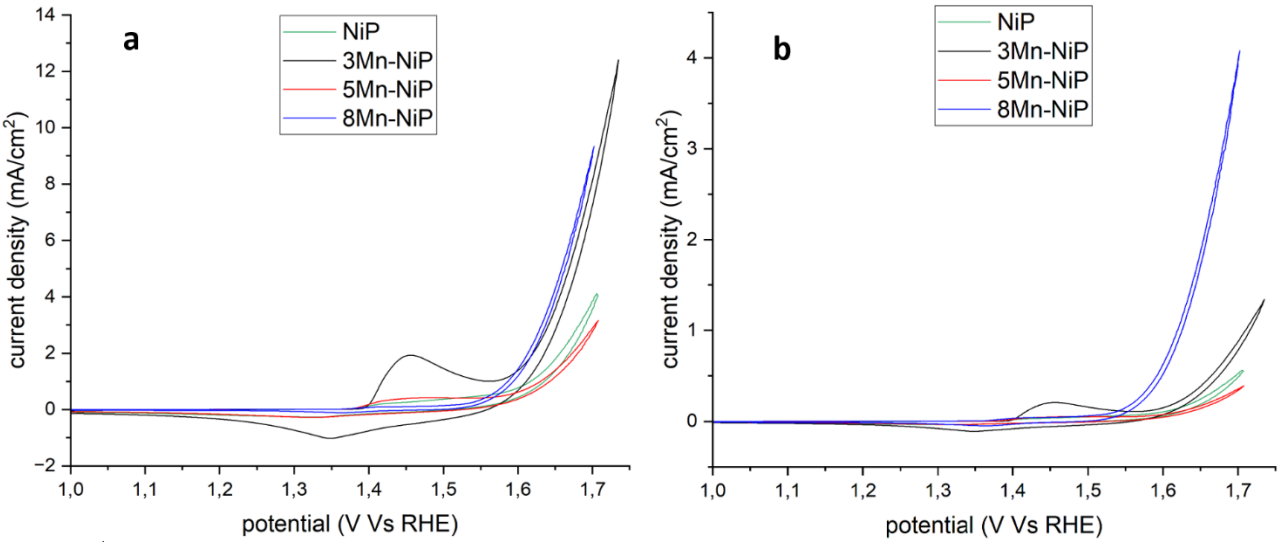

Figure 4.16 CVs in 1 M KOH of the NiP and Mn-doped NiP samples. The current was normalized by the geometric area (0,0707cm^2) of the electrode (at); and by the ECSA (b).

The Tafel analysis was performed to determine the reaction kinetics, figure 4.17. The values of Tafel slopes (reported in graph 4.17) do not present a visible trend. All the Mn-modified samples present a higher Tafel slope value than the non-modified sample except for the 8Mn-NiP sample. The sample that showed the best performance in figure 4.16b also presents the lower Tafel slope in figure 4.17. The values obtained are similar, albeit slightly lower, to what found in literature[25]. What was found is that the presence of manganese did have an effect on the Tafel values but no particular trend was observed with different amount of dopant like in this work[25].

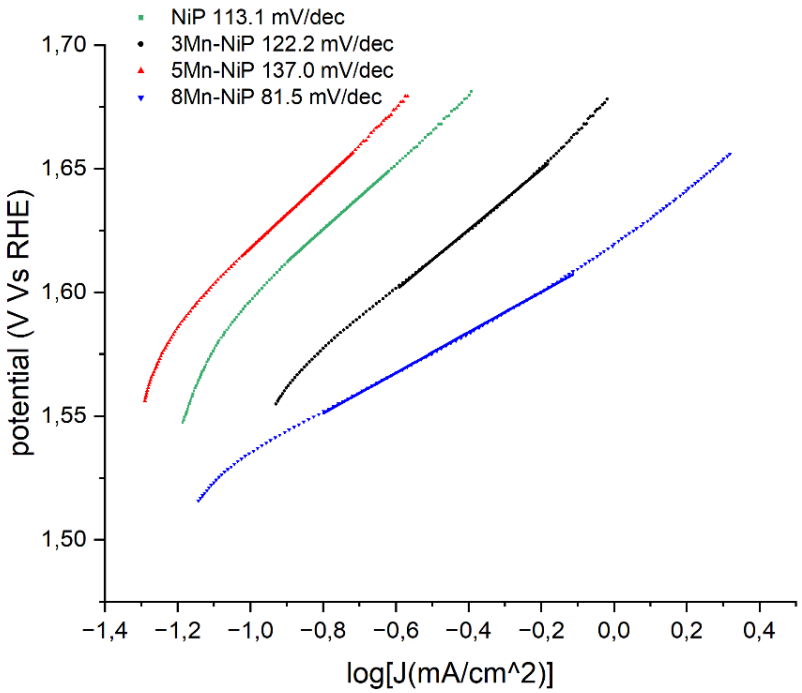

Figure 4.17 Tafel analysis of the LSVs in 1 M KOH of the NiP and the manganese-modified samples.

Then, urea was added to the electrolyte, and linear voltammetries (LSVs) were recorded. Figure 4.18 reports the LSVs of the Mn-modfied samples and the pure sample for UOR. The OER LSVs are also reported for comparison. As it was done in chapter 3 for the hydroxides sample, the dotted lines are used for the LSVs without urea meanwhile the full lines are used for the LSVs with urea. In correspondence of the oxidation of Ni^{2+} species to Ni^{3+}, the current starts to increase, suggesting that the oxidation of urea is catalyzed by the Ni^{3+} species, as described in Chapter 1. The presence of urea in solution makes possible to produce hydrogen at much lower potentials because the oxidation of urea starts at lower potentials than the oxygen evolution reaction, since the UOR is linked with the presence of Ni^{3+} species, as discussed before. All the samples reached higher current densities in presence of urea and at lower potentials since the increase in current happens at the same time of the oxidation of nickel. Table 4.7 reports the onset potential, it shifts to lower potentials with the increase in manganese and this translates into a higher activity for the UOR. Table 4.7 reports the on-set potentials of the samples, it is important to point out that these values are not very accurate since there are two process that overlap: the oxidation from Ni^{2+} to Ni^{3+} and the urea oxidation. This makes difficult to determine the real on-set of the UOR. However, since the UOR is tightly linked to the oxidation of nickel, the values in table 4.7 are still a good indicator because if the nickel oxidation starts at lower potential, consequently, the UOR starts at lower potentials. The 5Mn-NiP sample shows no significant differences respect to the non-modified sample, they present the same on-set and reach similar current density, while the 3Mn-NiP and 8Mn-NiP samples reach higher current densities and have, especially the 8Mn-NiP sample, much lower on-set potentials. Our results are in agreement with the literature where it was found that the introduction of manganese in the sample should increase the activity and shift the curve towards lower potential[25]. [25] reports that the shift due to the introduction of manganese is of 90 mV which is higher than the best result obtained in this work (table 4.10).

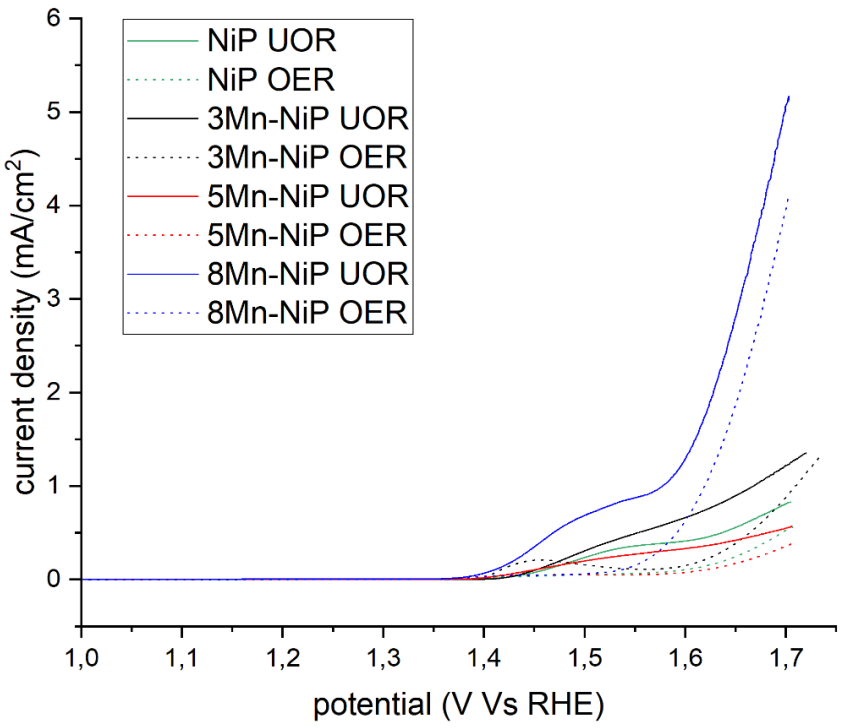

Figure 4.18 LSVs in 0.33 M urea + 1 M KOH (solid lines) of the NiP and Mn-modified NiP samples. The LSVs in absence of urea (OER) are reported as reference (dotted lines).

Table 4.10 the on-set potentials of the samples are reported in the central column and on the last column is reported the difference between the on-set value of the non-modified material and the on-set value of the modified material

sample	On-set (V)	Shift (mV)
NiP	1.43	-
3Mn-NiP	1.43	0
5Mn-NiP	1.41	20
8Mn-NiP	1.39	40

To obtain information about the reaction kinetics, the Tafel analysis was performed (figure 4.19). The Tafel slopes are presented in table 4.11. A lower Tafel slope signifies a more favorable reaction kinetics, in this case the lower slope was obtained with the 3Mn-NiP sample, while the highest value is associated with the non-modified sample. The presence of manganese seems to help the kinetics of the UOR. It is important to highlight that these values are obtained from LSVs measurements and that, in the region in which the Tafel slope is calculated, two processes are overlapped, as described previously. Therefore, these are indicative values used to compare it with the OER values and the ones in literature. These values are similar to what found in literature[25] All the Mn-modified samples present a lower slope value than the non-modified sample, like it was found in literature[25]. Table 4.8 reports the slope values in absence ad presence of urea for the NiP sample and the Mn-doped samples. In presence of urea the slopes are much lower than in absence of it, this means that the UOR has faster kinetics than the OER.

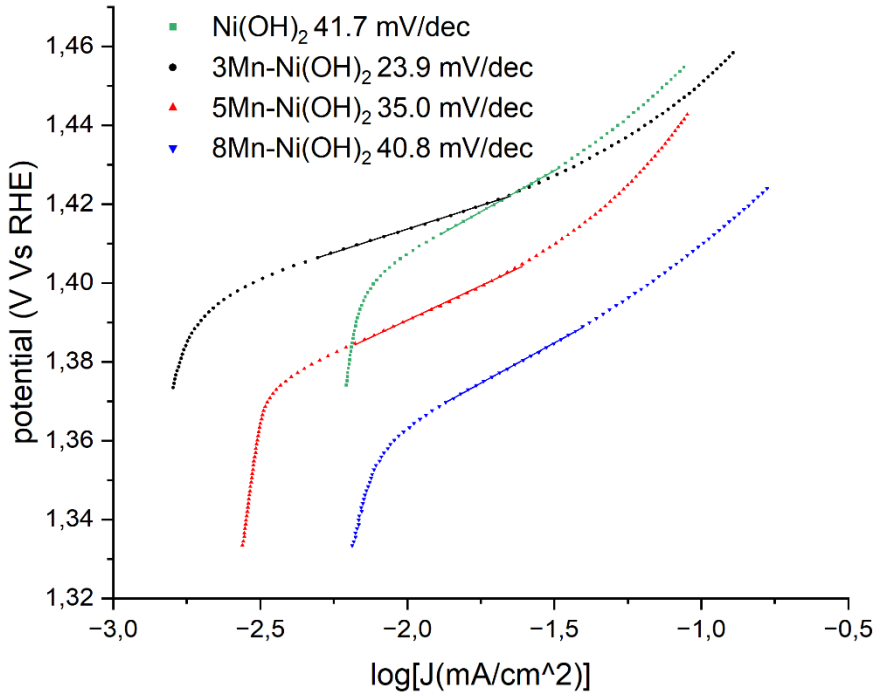

Figure 4.19 Tafe analysis of the LSVs un 0.33 M urea + 1 M KOH.

Table 4.11 Tafel slope values for NiP and the three Mn-doped samples

sample	Tafel slope (mV/dec) (UOR)	Tafel slope (mV/dec) (OER)
NiP	113.1	41.7
3Mn-NiP	122.2	23.9
5Mn-NiP	137.0	35.0

8Mn-NiP	81.5	40.8

4.4.2 Mo-doped nickel phosphides

The same procedure described above was performed for the test of the Mo-based materials. Figure 4.20 reports the CVs in absence of urea for the nickel phosphide and the three Mo-modified samples. The Ni^{2+}/Ni^{3+} redox couple is observed in the same potential window described for the Mn-based samples. The addition of the second metal can facilitate the oxidation of Ni^{2+} species to Ni^{3+} species and this could be beneficial for the UOR since urea is catalyzed by the oxidized species. The effect of molybdenum on the nickel oxidation peak is summarized in table 4.12. The oxidation peak is shifted towards lower potentials by adding molybdenum to the sample. The peak separation values are lower for the modified samples than for the pristine one indicating that the presence of the second metal increased the conductivity. The entity of the peak shift is not linked to the amount of molybdenum since the highest shift is observed for the 20Mo-NiP sample. The 30Mo-NiP sample presents a higher shift than the pristine sample and the 8Mo-NiP sample but still lower than the 20Mo-NiP sample.

Table 4.12 position of the oxidation peaks and reduction peaks of the sample present in figure 4.18. it's reported the distance between the two peaks in mV

sample	Oxidation peak (V)	Reduction peak (V)	Peak separation (mV)
NiP	1.45	1.31	140
8Mo-NiP	1.45	1.32	13
20Mo-NiP	1.44	1.36	80
30Mo-NiP	1.44	1.33	110

The currents observed at potentials higher than 1.6 V are related to the OER. Comparing the CVs normalized by the geometric area (Figure 4.20a), it seems that the addition of Mo has no significative effect on the activity since 20Mo-NiP and 30Mo-NiP reach current densities just slightly higher than the pristine sample. The 8Mo-NiP sample shows lower current densities than the NiP sample. However, as explained in chapter 3 for the Mn-$Ni(OH)_2$ samples, the conclusions extracted from this plot are not reliable. For this reason, currents were also normalized by the ECSA (Figure 4.20b). In this case, the 8Mo-NiP and 30Mo-NiP samples shows a very similar behaviour to the pristine sample, meanwhile the 20Mo-NiP sample reaches much higher current densities at much lower potentials than the non-modified sample. The fact that the 20Mo-NiP shows a much higher activity than the other three samples could be due to the fact that the XRD measurements of this sample show the smallest amount of nickel oxide (figure 4.11). In literature it was found that the presence of molybdenum should enhance the activity of Ni_2P[17,26]. The presence of molybdenum also shifted the oxidation peak towards lower potential like it was recorded in figure 4.20. It was also found that the activity for OER it is not strictly linked to the amount of the molybdenum in the samples[27]. [27] reports that the activity of the sample decreased by increasing the amount of molybdenum over the Mo:Ni ratio of 1:1.

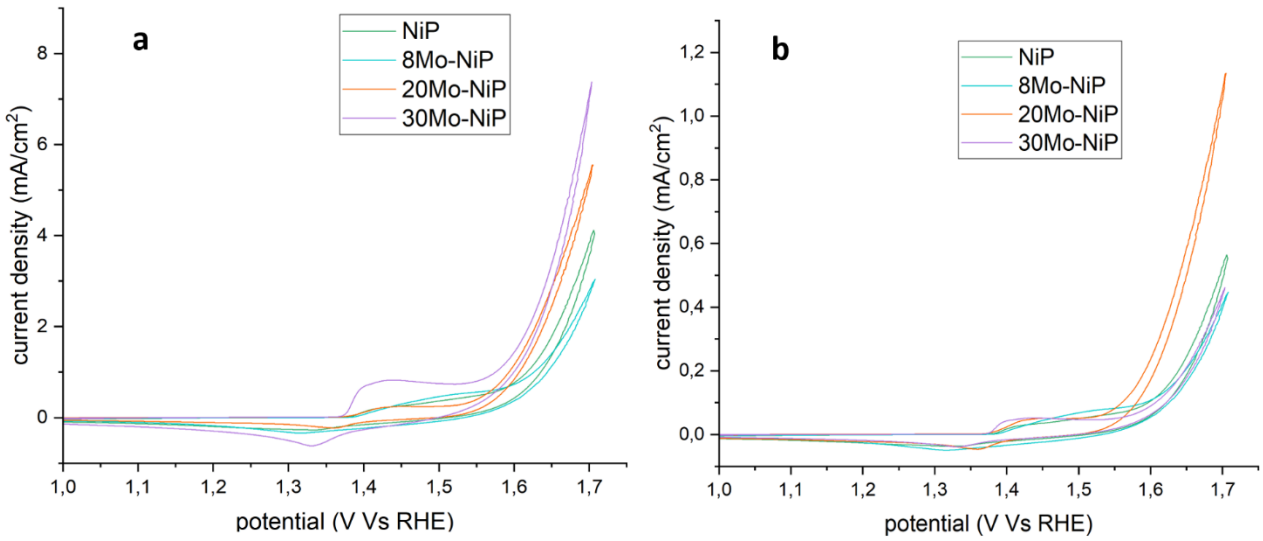

Figure 4.20 CVs in 1 M KOH of the NiP and Mo-doped $Ni(OH)_2$ samples. The current was normalized by the geometric area (0,0707cm^2) of the electrode (left); and by the ECSA (right).

From the data obtained it was possible to draw the Tafel plots. The Tafel slope values can be seen in figure 4.21. The 20Mo-NiP sample is the only sample with a lower slope value than the non-modified sample. The sample that showed the best performance in figure 4.20b is also the sample with the lowest slope value. No particular trend is observed with the different amount of molybdenum in the samples. The values of the Mo-modified samples are higher than those reported in literature[26]. This difference could be due to the presence of molybdenum oxide.

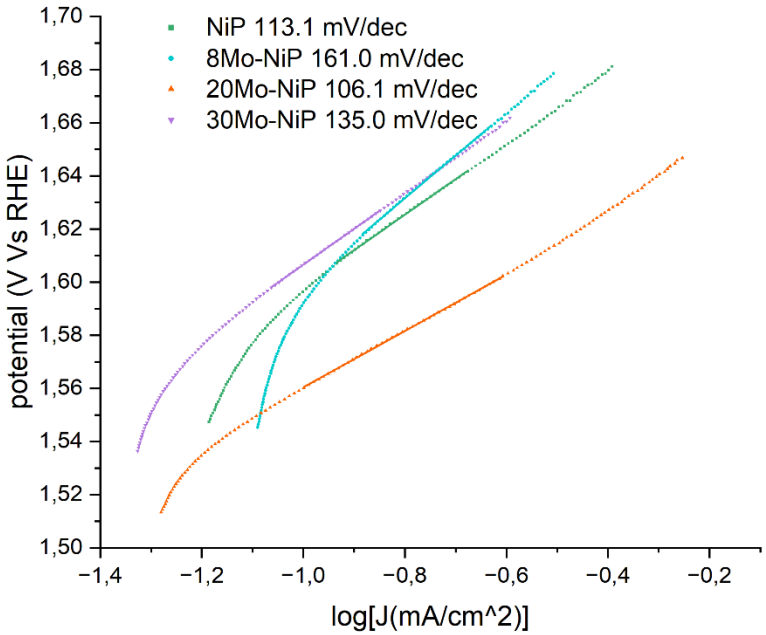

Figure 4.21 Tafel analysis of the LSVs in 1 M KOH of the $Ni(OH)_2$ and the molybdenum-modified samples

Then, urea was added to the electrolyte, and linear sweep voltammetries (LSVs) were recorded. Figure 4.22 reports the LSVs of the NiP and the Mo-modified samples. It is possible to see that the current density starts to increase in correspondence of the nickel oxidation peak described by the dotted line. The presence of urea results in much higher currents at lower potential. All the samples reached higher currents in presence of urea than in its absence. The urea oxidation is strictly correlated with the presence of Ni^{3+}. The 8Mo-NiP

sample shows lower current densities than the non-modified sample, as happened for OER. 30Mo-NiP shows current densities similar to the pristine sample, while 20Mo-NiP shows current densities much higher than NiP. Table 4.13 reports the on-set potentials of the samples, as discussed before it is important to remember that, in the region in which the on-set is calculated, two different process overlap. 8Mo-NiP presents the same on-set as the pristine material meaning that this sample is actually worse than the non-modified sample since it also reaches lower currents. 30Mo-NiP and 20Mo-NiP present an on-set potential that is 20mV and 40 mV lower than the non-modified sample, respectively. In literature it was found that the activity of the molybdenum-modified nickel phosphides should be higher than the non-modified sample[29]. Li *et al*. found that the UOR activity of nickel phosphide decreased for Mo:Ni ratios higher than 0.5:1.[29]

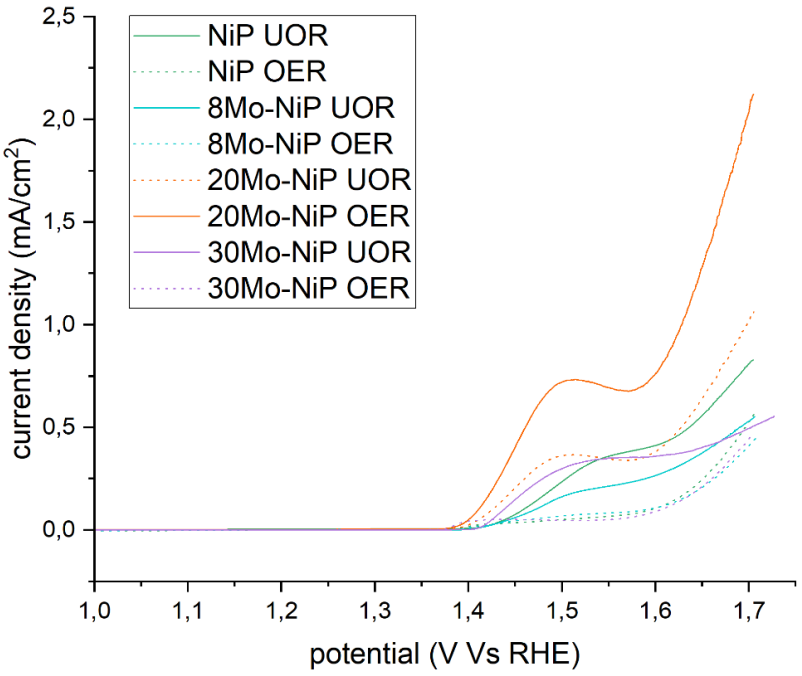

Figure 4.22 LSVs in 0.33 M urea + 1 M KOH (solid lines) of the NiP and Mo-modified NiP samples. The LSVs in absence of urea (OER) are reported as reference (dotted lines).

Table 4.13 the on-set potentials of the samples are reported in the central column and on the last column is reported the difference between the on-set value of the non-modified material and the on-set value of the modified material

sample	On-set (V)	Shift (mV)
NiP	1.43	-
8Mo-NiP	1.43	0
20Mo-NiP	1.39	40
30Mo-NiP	1.41	20

To obtain information about the reaction kinetics, the Tafel analysis was performed (figure 4.23). The Tafel slopes are presented in table 4.14. All the molybdenum-modified samples present a lower slope value than the pristine sample. No particular trend is noticed with the amount of molybdenum since the 8Mo-NiP sample and the 30Mo-NiP sample have a similar value, while 20Mo-NiP presents a significative higher value. The values obtained are in agreement with those reported in the literature[30]. In literature it was found that the presence of molybdenum lowers the Tafel slope values[30]. Comparing the Tafel slopes for the UOR and OER

processes (table 4.14), it can be seen that the slopes are much lower in presence of urea than in its absence, indicating that UOR has faster kinetics than OER.

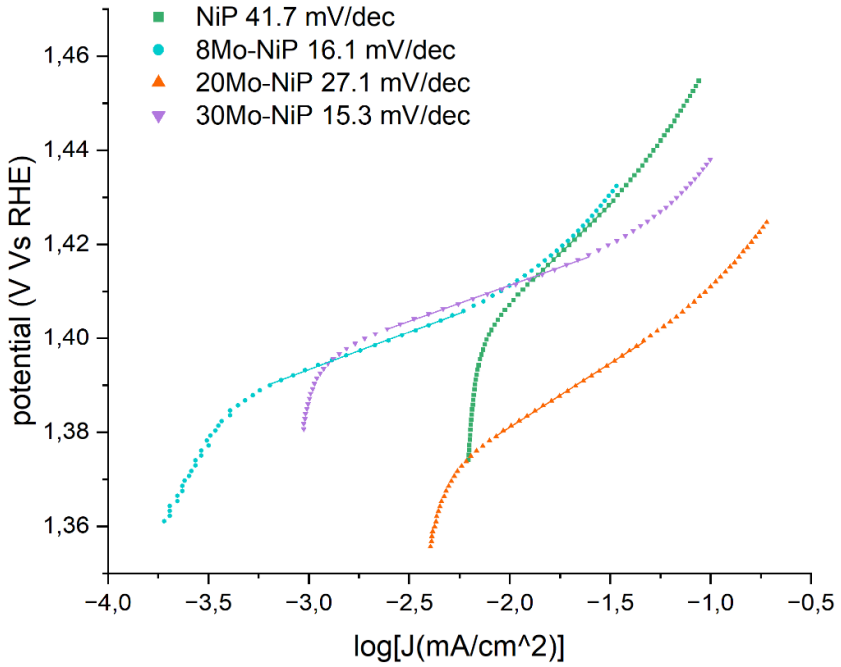

Figure 4.23 Tafel analysis of the LSVs in 0.33 M urea + 1 M KOH of the NiP and the molybdenum-modified samples.

Table 4.14 Tafel slope values determined for NiP and the three Mo-doped samples

sample	Tafel slope (mV/dec) (UOR)	Tafel slope (mV/dec) (OER)
NiP	41.7	113.0
8Mo-NiP	16.1	161.0
20Mo-NiP	27.1	106.1
30Mo-NiP	15.3	135.0

4.4.3 Comparison Between Mn- and Mo-modified samples

The objective of this section is to compare the effect of the two metals studied. With this aim, the best catalyst of the manganese and molybdenum series are compare to the pristine NiP.

Regarding the OER (absence of urea), the CVs of the three samples discussed in this paragraph are reported in figure 4.24. The two metals introduced in the samples increase the activity of the materials towards the OER. Manganese seems to have a stronger effect on the catalytic performance resulting in higher current densities and the shift of the OER curve towards lower potentials. The onset potential is 1.41 V and 1.44 V for 8Mn-NiP and 20Mo-NiP, respectively.

Regarding the UOR (presence of urea), the LSVs are reported in figure 4.25. Both the modified materials show higher activity than the non-modified sample, since they reach higher current densities and they are also clearly shifted towards lower potentials. This is due to the fact that the nickel oxidation peak of the two modified samples is shifted towards lower potentials in respect to the non-modified sample, as mentioned above. Even though the nickel oxidation peak of the 20Mo-NiP sample is attained at higher potentials than that of the 8Mn-NiP sample, the two materials show the same on-set for the UOR. The 8Mn-NiP sample shows much higher current densities than the Mo-modified sample, which could be attributed to the highest

oxidation peak shift of the Mn-modified sample. The highest shift value could translate in a higher current because more Ni^{3+} sites are available at the same potential respect to the Mo-modified sample.

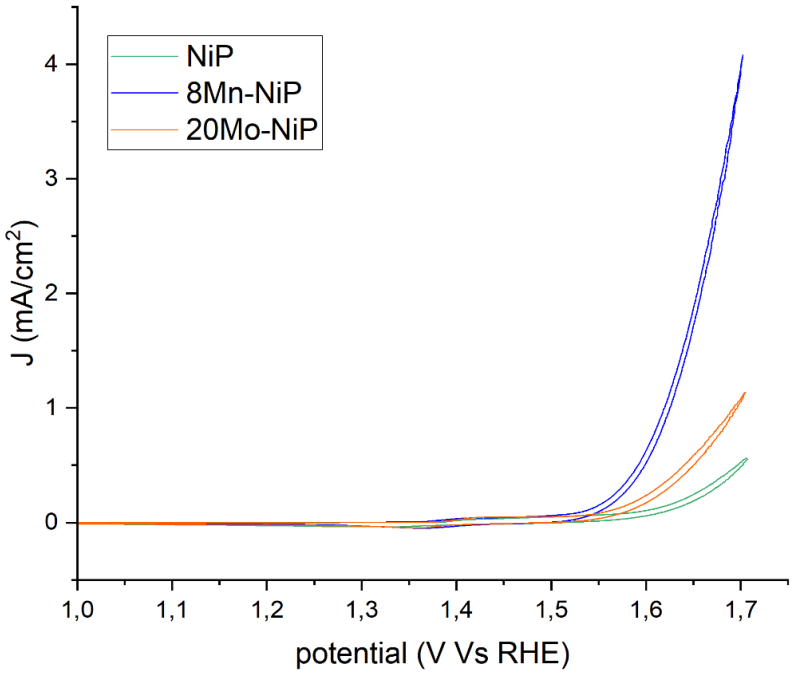

Figure 4.24 Cvs of the $Ni(OH)_2$, the 20Mo-$Ni(OH)_2$ and 8Mn-$Ni(OH)_2$ samples in the absence of urea

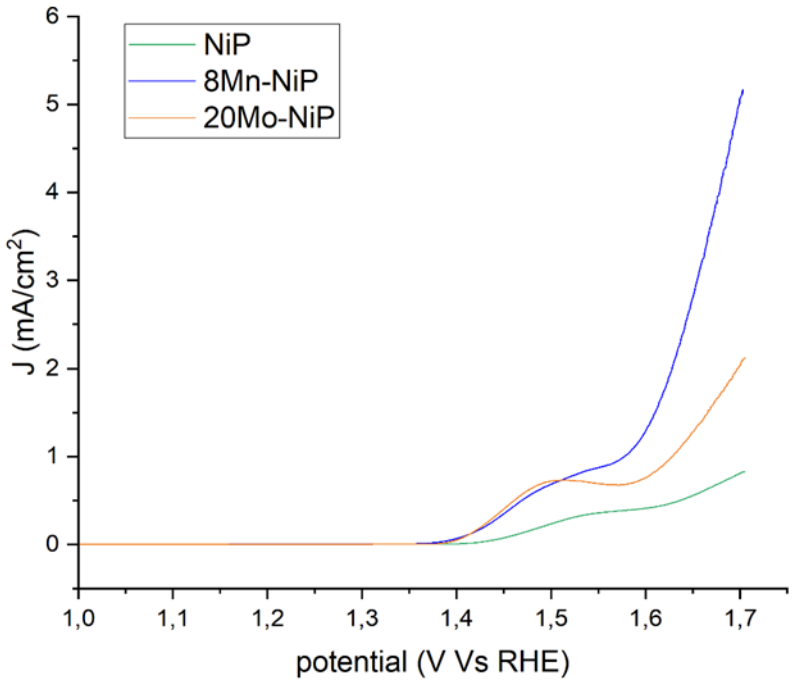

Figure 4.25 LSVs of the NiP, the 20Mo-NiP and 8Mn-NiP samples in presence of urea

4.5 Hydrogen evolution reaction (HER)

The Mn- and Mo-modified samples, as well as NiP, were tested as HER catalysts and the results are discussed in the following. All potential values are referred to reversible hydrogen electrode (RHE), meanwhile the

current values were normalized both for the electroactive area of the electrode and corrected for the ohmic drop of the electrolyte solution.

4.5.1 Mn-doped nickel phosphides

Figure 4.26 reports the LSVs of the NiP and Mn-NiP samples. As can be observed, 5Mn-NiP and 8Mn-NiP show a similar behavior to the pristine material, while 3Mn-NiP behaves better. Table 4.15 reports the on-set values of the four samples. The introduction of manganese shifts the on-set potential towards less negative potentials. This effect increases with the manganese content. In the literature, it was found that the introduction of manganese in the sample increased the activity towards the HER. However, if the manganese content exceeds the 7 at.%, the activity decreased.[24] Our results are in agreement with those reported by Zhang et al., even if 8Mn-NiP still behaves better than NiP. The on-set potentials in this thesis are much higher than those reported in the literature.[24,31] This not expected result could be attributed to a non-total phosphurization of the hydroxide samples, as suggested by the XRD results.

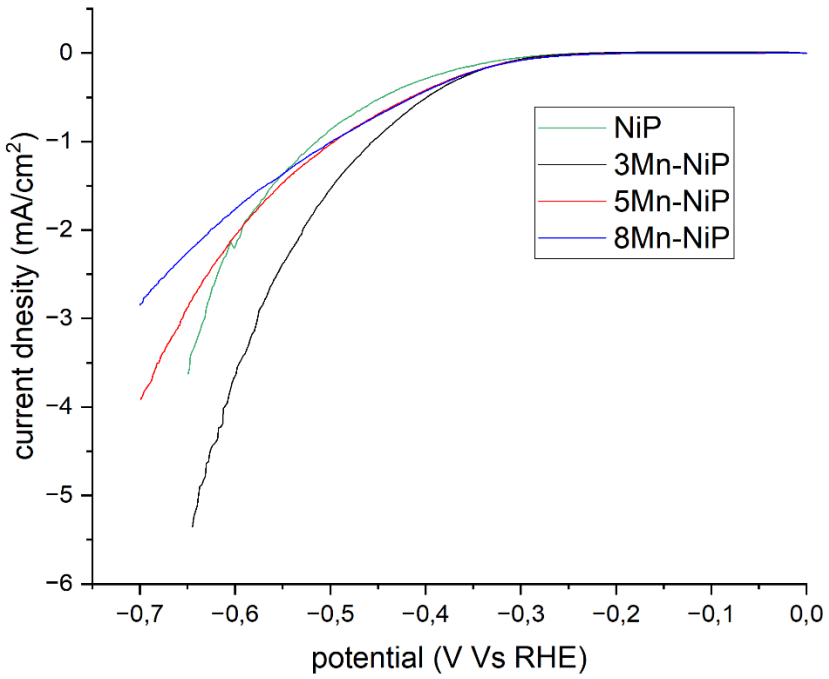

Figure 4.26 LSVs in 1M KOH of the NiP sample and the manganese-modified samples.

Table 4.15 On-set potentials obtained from the data in figure 4.22.

sample	On-set (V)
NiP	-0.43
3Mn-NiP	-0.40
5Mn-NiP	-0.37
8Mn-NiP	-0.34

To obtain information about the reaction kinetics, the Tafel analysis was performed and the results are reported in figure 4.27. Similar values are obtained for all the samples. only the 3Mn-NiP sample show a lower value than the pristine sample, while the 8Mn-NiP sample's slope value is basically the same as the pure

material one. No particular trend is observed with the different amount of manganese in the sample since the lowest slope value is associated to the sample with the lowest amount of manganese. The values obtained are similar to what found in literature[24]. In [23] manganese modified nickel phosphides and pure nickel phosphide were tested as OER and HER catalysts. It was found that the 3% (atomic) Mn-NiP sample showed the lowest Tafel slope of all the samples, the same was found in this work.

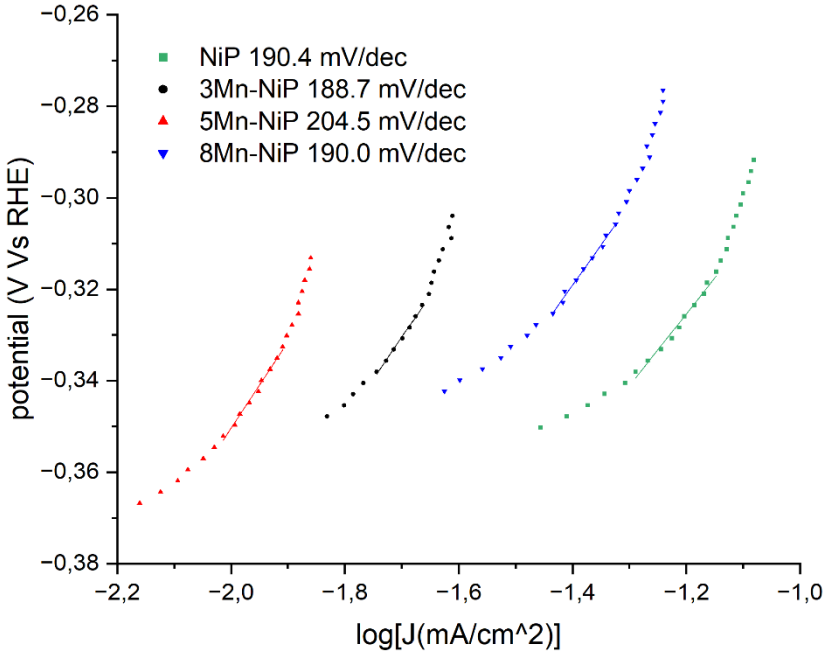

Figure 4.27 Tafel analysis of the LSVs in 1 M KOH of the NiP and the manganese-modified samples

4.5.2 Mo-doped nickel phosphides

Figure 4.28 are reports the LSVs of the NiP and Mo-modified samples. As can be seen, the presence of Mo has a negative effect on the performance of NiP. In fact, the three Mo-modified NiP samples show a lower catalytic activity than the pristine one, and the performance worsening increases with the amount of Mo. This result could be associated to the presence of both nickel and molybdenum oxides due to the partial phosphurization of the material during the synthesis process, as observed by XRD. In literature it was found that MoO_3 is a terrible catalyst for the HER[32]. Table 4.16 reports the on-set value for the four samples. No Mo-modified sample present a less negative on-set potential than the non-modified sample. The other two sample present higher on-set values than the pristine sample, especially the 30Mo-NiP sample that has an impressing high on-set value. In literature it was found that the presence of molybdenum should increase the activity of the material[33]. Considering the data in table 4.16, only the 20Mo-NiP sample shows a lower on-set respect to the pure material meanwhile the other two materials have much higher values. The on-set values are all much higher than what is found in literature this could be due to the presence of nickel oxide like it was hypnotized for the Mn-modified materials.

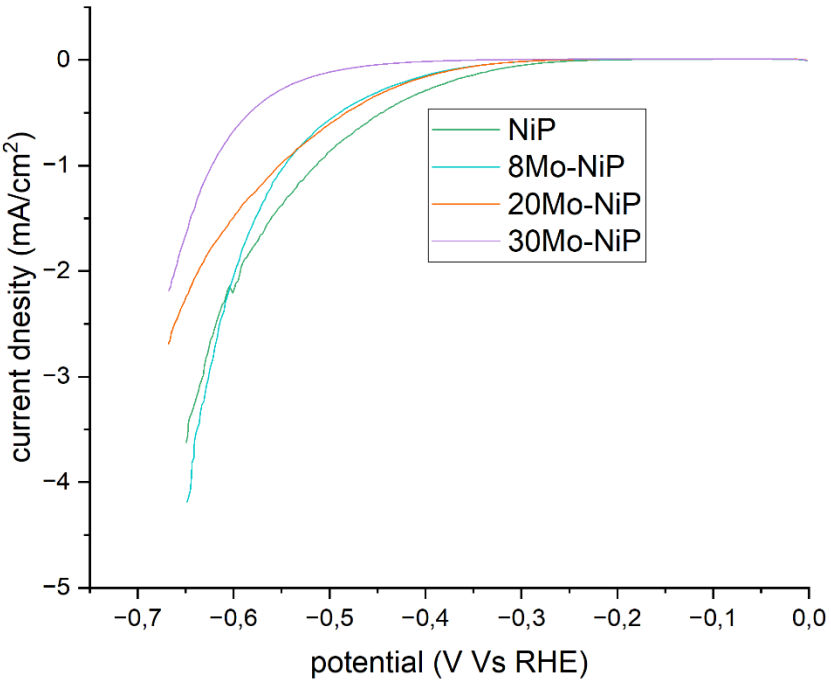

Figure 4.28 LSVs of the NiP sample and the manganese-modified samples.

Table 4.16 On-set values obtained from the data in figure 4.23.

sample	On-set (V)
NiP	-0.43
8Mo-NiP	-0.49
20Mo-NiP	-0.41
30Mo-NiP	-0.53

From the data obtained it was possible to draw the Tafel plots for the nickel phosphide sample and the molybdenum-modified samples. The Tafel slopes values are reported in figure 4.29. All the sample except for the 30Mo-NiP sample show lower Tafel slope values than the pristine material. It appears that the increase in molybdenum content lowers the Tafel slope values but the 30Mo-NiP sample has a much higher slope value than the other samples. This sample is also the one that showed the worse performance as an HER catalyst. The values obtained are similar to the ones found in literature [32]. In [31] is reported that the presence of molybdenum decreases the Tafel slope and this is also reported in this work except for the 30Mo-NiP sample.

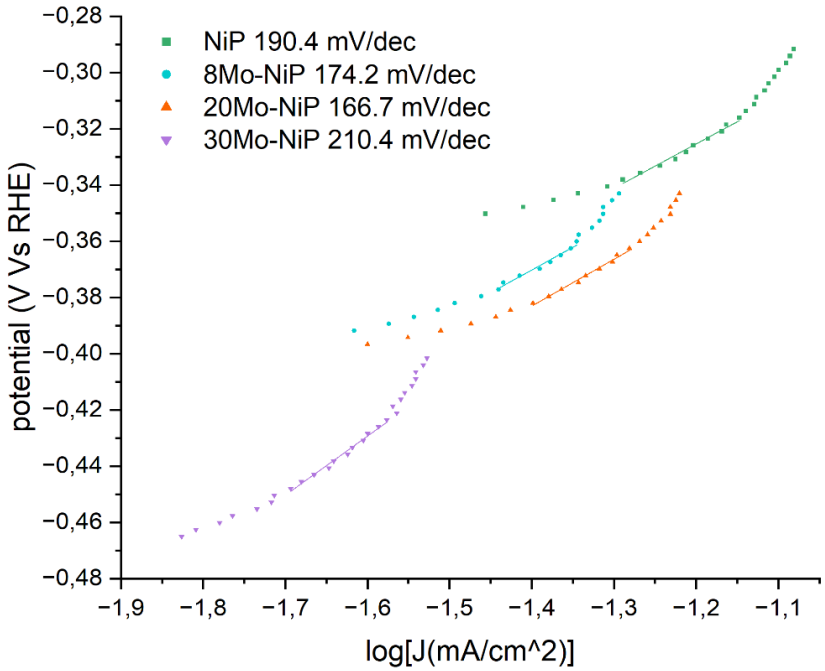

Figure 4.29 Tafel analysis of the LSVs in 1 M KOH of the NiP and the manganese-modified samples

4.5.3 comparison

The objective of this section is to compare the effect of the two metals studied. With this aim, the best catalyst of the manganese and molybdenum series are compared to the pristine NiP.

Figure 4.30 reports the LSVs of the pristine material and the two best catalysts: 20Mo-NiP and 8Mn-NiP. The two best catalysts for the HER are actually the same samples that were considered the best catalyst for the UOR. The effect of the foreign element is not that strong, the only difference is a slight shift of the on-set to lower potentials. The on-set of the 20Mo-NiP sample is not that lower than the pristine material while for the 8Mn-Nip sample there is a much more significative variation. The current densities are similar between the three samples. The 8Mn-NiP sample is more active than the 20Mo-NiP sample like it was for the UOR measurements.

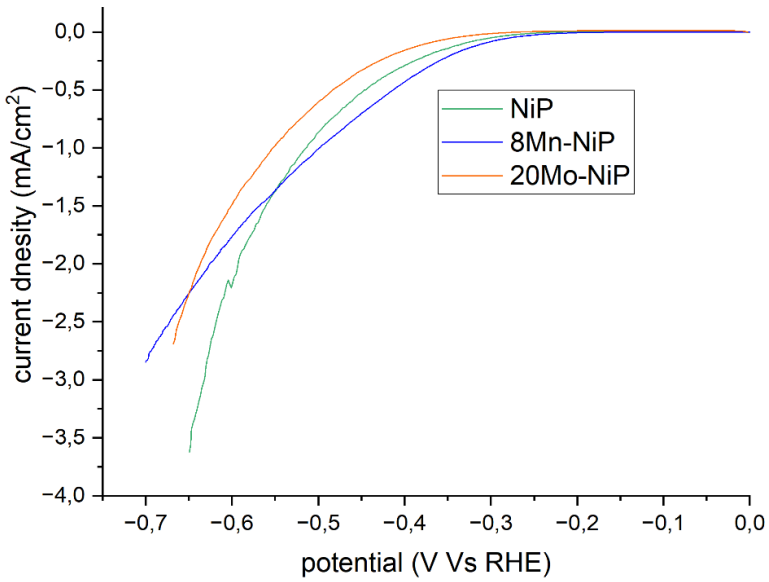

Figure 4.30 LSVs of the NiP sample and the 20Mo-NiP and the 8Mn-NiP samples.

4.6 Conclusions

Nickel phosphides and their derivates with manganese or molybdenum were synthetized from the corresponding nickel hydroxide-based samples (described in chapter 3) through a phosphurization treatment with sodium hypophosphite. They were characterized by SEM-EDX, XRD and XPS to determine their morphological, structural and chemical properties, and tested as electrocatalysts for the urea oxidation reaction (UOR) and hydrogen evolution reaction (HER).

The morphological characterization carried out by SEM showed that the size and shape oof the particles depended only on the synthesis method, since the phosphide were obtained starting from the nickel hydroxide-based samples. the presence of a second metal did not have any effect on the morphology or particle dimension of the samples. all the materials presented a wide particle size distribution, form hundreds of nm to hundreds of µm, and the particles did not have a defined shape. Bigger particles surrounded by smaller particles. The presence of the second metal was confirmed by EDX measurements. The M:Ni ratio (M = Mo or Mn) did not change after the phosphorization.

The nickel phosphide phase obtained during the phosphurization treatment was Ni_2P, as determined by XRD. In the case of the Mn-modified samples, the presence of $Ni_{12}P_5$ as minority phase was also detected. However, it was not observed in the Mo-modified materials. All the samples contained nickel oxide, to a greater or lesser extent, which is attributed to a non-complete phosphurization of the samples in the bulk due to the large particle size and the wide size distribution. In the Mn-based samples, no manganese phases were observed, suggesting that Mn atoms stayed as metal ions inside the phosphide structure. The introduction of Mn ions resulted in a contraction of the Ni_2P structure. In the Mo-based materials, on the contrary, molybdenum oxide was present. The Mn and Mo species present at the surface of the particles are Mn^{4+} and Mo^{6+}, respectively. In this case, it was not possible to perform the XAS measurements to determine the species in the bulk.

Finally, all the materials were tested as UOR and HER electrocatalysts. First, measurements were conducted in absence of urea. In these conditions, the oxygen evolution reaction takes place on the catalysts, therefore, it was possible to study the activity of the metal-modified phosphides, as well as the effect of the second metal. In the case of the Mn-doped samples, a clear increase in the OER activity was observed with the amount of Mn. However, only the catalyst with the highest amount of manganese (8Mn-NiP) showed a better performance than the pristine material. For the molybdenum-modified materials, only the 20Mo-NiP sample had a better performance than the non-modified sample. In presence of urea all the samples reached higher current densities at lower potential respect to the measurements in absence of urea. The Mn-doped samples presented an interesting trend since the activity increased from the 3Mn-NiP sample to the 8Mn-NiP, and both samples showed a better performance than the un-doped material. However, 5Mn-NiP showed a worse performance than the pure material. For the molybdenum-modified samples, as happened for the OER measurements, the only sample that showed a better performance than the un-modified sample was 20Mo-NiP. The other two Mo-containing samples showed a similar behavior to NiP. In the literature, it was found that an excessive amount of molybdenum could actually decrease the performance of the catalysts, which is in agreement with our results.

All the samples were also tested as HER electrocatalysts. In this case, the addition of a second metal had a negative effect on the HER activity in all cases, and the catalysts' performance was lower than that reported in the literature. This negative result could be explained due to the non-total phosphurization of the materials and, therefore, to the presence of nickel and molybdenum oxides, which are not active for this reaction.

Bibliography

1. Xu, S. *et al.* Transition Metal-Based Catalysts for Urea Oxidation Reaction (UOR): Catalyst Design Strategies, Applications, and Future Perspectives. *Adv Funct Materials* **34**, 2313309 (2024).
2. Li, J., Wang, S., Chang, J. & Feng, L. A review of Ni based powder catalyst for urea oxidation in assisting water splitting reaction. *Advanced Powder Materials* **1**, 100030 (2022).
3. Chen, J. & Shen, Y. Effects of Manganese Doping into Nickel Hydroxides for the Electrochemical Conversion of KA Oil. *ACS Sustainable Chem. Eng.* **12**, 5907–5916 (2024).
4. Lu, Z. *et al.* Nickel–Molybdenum-Based Three-Dimensional Nanoarrays for Oxygen Evolution Reaction in Water Splitting. *Molecules* **29**, 3966 (2024).
5. Zhong, M., Li, W., Wang, C. & Lu, X. Synthesis of hierarchical nickel sulfide nanotubes for highly efficient electrocatalytic urea oxidation. *Applied Surface Science* **575**, 151708 (2022).
6. Ma, Y., Ma, C., Wang, Y. & Wang, K. Advanced Nickel-Based Catalysts for Urea Oxidation Reaction: Challenges and Developments. *Catalysts* **12**, 337 (2022).
7. Dong, L., Chu, Y. & Sun, W. Controllable Synthesis of Nickel Hydroxide and Porous Nickel Oxide Nanostructures with Different Morphologies. *Chemistry A European J* **14**, 5064–5072 (2008).
8. Man, H.-W. *et al.* Transition metal-doped nickel phosphide nanoparticles as electro- and photocatalysts for hydrogen generation reactions. *Applied Catalysis B: Environmental* **242**, 186–193 (2019).
9. Schalenbach, M. *et al.* Nickel-molybdenum alloy catalysts for the hydrogen evolution reaction: Activity and stability revised. *Electrochimica Acta* **259**, 1154–1161 (2018).
10. Shalom, M. *et al.* Nickel nitride as an efficient electrocatalyst for water splitting. *J. Mater. Chem. A* **3**, 8171–8177 (2015).
11. Yang, H. *et al.* 3D Cross-Linked Structure of Manganese Nickel Phosphide Ultrathin Nanosheets: Electronic Structure Optimization for Efficient Bifunctional Electrocatalysts. *ACS Appl. Energy Mater.* **4**, 8563–8571 (2021).
12. Chen, F. *et al.* Electronic structure modulation of nickel hydroxide porous nanowire arrays via manganese doping for urea-assisted energy-efficient hydrogen generation. *Journal of Colloid and Interface Science* **626**, 445–452 (2022).
13. Chen, Y., Rui, K., Zhu, J., Dou, S. X. & Sun, W. Recent Progress on Nickel-Based Oxide/(Oxy)Hydroxide Electrocatalysts for the Oxygen Evolution Reaction. *Chemistry A European J* **25**, 703–713 (2019).
14. Tang, Y. *et al.* Hydrothermal synthesis of a flower-like nano-nickel hydroxide for high performance supercapacitors. *Electrochimica Acta* **123**, 158–166 (2014).
15. Ray, A., Sultana, S., Paramanik, L. & Parida, K. M. Recent advances in phase, size, and morphology-oriented nanostructured nickel phosphide for overall water splitting. *J. Mater. Chem. A* **8**, 19196–19245 (2020).
16. Wang, X., Li, W., Xiong, D., Petrovykh, D. Y. & Liu, L. Bifunctional Nickel Phosphide Nanocatalysts Supported on Carbon Fiber Paper for Highly Efficient and Stable Overall Water Splitting. *Adv Funct Materials* **26**, 4067–4077 (2016).
17. Yu, Y. *et al.* Progress in the development of heteroatom-doped nickel phosphates for electrocatalytic water splitting. *Journal of Colloid and Interface Science* **607**, 1091–1102 (2022).
18. Zhao, Z., Dong, Y., Ding, H., Li, X. & Chang, X. Manganese-facilitated dynamic active-site generation on Ni2P with self-termination of surface reconstruction for urea oxidation at high current density. *Water Research* **253**, 121266 (2024).
19. Liu, D. *et al.* Disproportionation of hypophosphite and phosphite. *Dalton Trans.* **46**, 6366–6378 (2017).
20. Menezes, P. W. *et al.* Uncovering the Nature of Active Species of Nickel Phosphide Catalysts in High-Performance Electrochemical Overall Water Splitting. *ACS Catal.* **7**, 103–109 (2017).
21. Oyama, S. Effect of Phosphorus Content in Nickel Phosphide Catalysts Studied by XAFS and Other Techniques. *Journal of Catalysis* **210**, 207–217 (2002).
22. Zhang, P. *et al.* Nonmetallic Active Sites on Nickel Phosphide in Oxygen Evolution Reaction. *Nanomaterials* **12**, 1130 (2022).
23. Biesinger, M. C., Payne, B. P., Lau, L. W. M., Gerson, A. & Smart, R. St. C. X-ray photoelectron spectroscopic chemical state quantification of mixed nickel metal, oxide and hydroxide systems. *Surface & Interface Analysis* **41**, 324–332 (2009).

24. Zhang, C., Li, D. & Xu, Y. Mn-doped NiP: Facile synthesis and enhanced electrocatalytic activity for hydrogen evolution. *Journal of Materials Research* **37**, 807–817 (2022).
25. Yang, H. *et al.* 3D Cross-Linked Structure of Manganese Nickel Phosphide Ultrathin Nanosheets: Electronic Structure Optimization for Efficient Bifunctional Electrocatalysts. *ACS Appl. Energy Mater.* **4**, 8563–8571 (2021).
26. Wang, Q. *et al.* Mo-doped Ni_2P hollow nanostructures: highly efficient and durable bifunctional electrocatalysts for alkaline water splitting. *J. Mater. Chem. A* **7**, 7636–7643 (2019).
27. Chen, S., Dai, J., Ren, F., Xu, H. & Du, Y. 3D hollow nanoflowers assembled by ultrathin molybdenum-nickel phosphide nanosheets as robust electrocatalysts for oxygen evolution reaction. *Journal of Colloid and Interface Science* **536**, 71–79 (2019).
28. Elgrishi, N. *et al.* A Practical Beginner's Guide to Cyclic Voltammetry. *J. Chem. Educ.* **95**, 197–206 (2018).
29. Li, X. *et al.* Urine Treatment in a Stacked Membraneless Direct Urea Fuel Cell with Honeycomb-like Nickel–Molybdenum Bimetal Phosphide as the Anodic Electrocatalyst. *ACS Sustainable Chem. Eng.* **12**, 3621–3631 (2024).
30. Jiang, L. *et al.* Mo propellant boosting the activity of Ni-P for efficient urea-assisted water electrolysis of hydrogen evolution. *Journal of Colloid and Interface Science* **622**, 192–201 (2022).
31. Duraivel, M., Nagappan, S., Park, K. H. & Prabakar, K. Optimised Ni^{3+} /Ni^{2+} and Mn^{3+} /Mn^{2+} Ratios in Nickel Manganese Layered Double Hydroxide for Boosting Oxygen and Hydrogen Evolution Reactions. *ChemElectroChem* **9**, e202200822 (2022).
32. Peng, Z. *et al.* Strong Interface Enhanced Hydrogen Evolution over Molybdenum-Based Catalysts. *ACS Appl. Energy Mater.* **3**, 5219–5228 (2020).
33. Sun, Y. *et al.* Mo doped Ni_2P nanowire arrays: an efficient electrocatalyst for the hydrogen evolution reaction with enhanced activity at all pH values. *Nanoscale* **9**, 16674–16679 (2017).

CHAPTER 5

Conclusions

In this work different nickel hydroxide-based and nickel phosphide-based materials were synthetized. These materials were characterized with techniques such as SEM/EDX, XRD, XAS and XPS. The nickel hydroxide-based materials were tested as electrocatalysts for the OER and UOR while the nickel phosphide-based materials were tested as electrocatalysts for the OER, UOR and HER.

Nickel hydroxide-based materials were synthesized in collaboration with Circular Materials s.r.l. Seven samples were obtained: one pure nickel hydroxide sample, three manganese-modified samples and three molybdenum-modified samples. The atomic ratio (M/Ni*100, M= Mo/Mn) for the manganese-modified samples was 3, 5 and 8, while for the molybdenum-modified ones it was 8, 20 and 30. These nickel hydroxide-based materials were used as catalysts for the urea oxidation reaction (UOR). Subsequently, nickel phosphide-based materials were obtained by a phosphurization treatment of the corresponding nickel hydroxide samples. The reaction took place in a tubular oven in which the hydroxides and the phosphorus precursor were inserted in. These phosphides were used as catalysts for both the UOR and the hydrogen evolution reaction (HER). The focus of this work was to determine the effect of the second metal (Mn or Mo) on the catalytic activity, and to verify if the nickel phosphide-based materials could be used as bi-functional catalysts for the UOR and HER.

The composition of the samples was determined by EDX and ICP (only for the manganese-modified samples) measurements. Both techniques confirmed that the second metal was present in the sample in the desired concentrations but it did not confirm that the metal ions entered into the sample's structure. The morphology of all samples was studied using a scanning electron microscope (SEM). No particular morphology was found for any of the nickel hydroxide-based samples and the presence of the second metal did not have any influence on the morphology or the dimensions of the particles. The particles had a wide range of dimensions, from 1-2 µm to 300-400 µm. After the phosphorization the particles dimensions did not change and a wide range of dimensions were obtained. The morphology did change and bigger particles encircled by smaller particles were seen. The composition was measured wit EDX, no contaminations were found. Every sample had a Ni:M ratio (M= Mn or Mo) very close to the target value and the phosphorization did not change the ratio, as excepted.

The structural and chemical characterization revealed that, in all the hydroxide-based samples, the β-hydroxide phase was the main phase and no α-hydroxide phase was present. In the case of the Mn-doped $Ni(OH)_2$ samples, all the manganese was introduced into the β-hydroxide structure as dopant, since no separated phases of Mn were detected. The introduction of the Mn inside the structure was also confirmed by the shift of the (100) peak towards higher angles with the increase in manganese content. Mn^{3+} ions substituted Ni^{2+} ions in the hydroxide structure, resulting in an excess of positive charge, which originated the intercalation of anions in the interlayers. For the molybdenum-modified hydroxides, only a small part of the metal entered the β-$Ni(OH)_2$ structure as dopant. Most of the molybdenum species were present as separated

phases such as MoO_3 and $NiMoO_4$. The amount of these phases increased with the amount of molybdenum used in the synthesis. From the XAS measurements, it was confirmed that the average oxidation state of molybdenum was close to +6. From the XPS measurements it was confirmed the presence of the second metal at the surface for all the modified samples. From the XPS measurements it was possible to also obtain the percentage composition of the various samples. The values obtained were very similar to the ones obtained from EDX measurements meaning that the composition was the same both in the bulk and in the first layers of the samples. Regarding the nickel phosphides-based materials, the main phase present was the Ni_2P one, even if nickel oxide was observed in all the samples. In some samples, a small amount of the $Ni_{12}O_5$ phase was detected. The presence of nickel oxide in the samples was due to the fact that the phosphine was not capable of penetrating inside the bigger particles during the reaction time. No Mn or Mo separated phases were found, apart from the MoO_3 already present in the hydroxides. Only for the manganese-modified NiP samples, a shift of the (111) peak was observed, indicating that the manganese ions entered the structure. Thanks to XPS measurements, it was possible to confirm the presence of the second metal on the surface and that the oxidation state of Mn and Mo on the surface was +4 and +6, respectively. The oxidation state of manganese and molybdenum were the same as that obtained for the corresponding nickel hydroxides samples. The composition percentage obtained from XPS measurements was similar to the nickel hydroxide-based samples values. It was not possible to perform XAS measurements to determine the species in the bulk.

All the materials were tested as UOR electrocatalysts. First, measurements were conducted in absence of urea. In these conditions, the oxygen evolution reaction takes place on the catalysts; therefore, it was possible to study the activity of the samples, as well as the effect of the second metal, also in this reaction. In the case of the manganese-based catalysts, an increase in the OER activity was observed with the amount of Mn. However, both for the nickel hydroxides and nickel phosphides samples, only the samples with the highest amount of manganese (8Mn) showed a better performance than the un-doped material. The presence of manganese induced a shift of the nickel oxidation peak towards lower potentials and a decrease in peak separation for both the hydroxides and phosphides sample. The 8Mn-$Ni(OH)_2$ and 8Mn-NiP samples showed the most shifted nickel oxidation peak (1.43 V and 1.42 V, respectively) and the lowest peak separation (110 mV and 80 mV, respectively) of the respective material group. This indicates that the nickel phosphide based sample is more conductive than the 8Mn-$Ni(OH)_2$ sample. In the case of the molybdenum modified-hydroxides samples, the second metal did not have any effect on the OER catalytic activity. For the molybdenum modified-phosphides samples, on the other hand, only the 20Mo-NiP sample showed a better performance than the non-modified sample. 30Mo-$Ni(OH)_2$ and 20Mo-NiP showed the most shifted nickel oxidation peak (1.41 V and 1.44 V, respectively) and the lowest peak separation (70 mV and 80 mV, respectively) of the respective material group. The 20Mo-$Ni(OH)_2$ sample showed similar behaviour with the nickel oxidation peak at 1.41 V and a peak separation of 80 mV. In the case of the samples containing manganese, the nickel phosphide-based materials showed better results than the nickel hydroxide-based samples. On the other hand, for the samples containing molybdenum, hydroxides were more active than phosphides.

In presence of urea, different results were obtained. All the samples registered higher currents and at lower potentials than the measurements done in absence of urea. For the manganese-modified samples, contrasting results were obtained. In the case of the nickel hydroxide-based materials, the UOR activity increased with the amount of Mn and all the modified catalysts performed much better than the un-modified one. The higher the manganese content, the lower the on-set. 8Mn-$Ni(OH)_2$ had an on-set potential of 1.40 V. The Mn-doped samples presented an interesting trend since the activity increased from the 3Mn-NiP

sample to the 8Mn-NiP, and both samples showed a better performance than the un-doped material. However, 5Mn-NiP showed a worse performance than the pure material. The 8Mn-NiP sample presented an on-set potential of 1.39 V. In the case of the molybdenum-modified samples, interesting results were obtained. For the nickel hydroxide-based materials, the addition of molybdenum increased the UOR activity, both in terms of current densities and onset potential, respect to the un-doped hydroxide. A significative increase of the catalytic activity was observed going from 8Mo-Ni$(OH)_2$ sample to the 20Mo-Ni$(OH)_2$ sample. This increase in activity was attributed to the presence of other phases such as $NiMoO_4$ and MoO_3, the former has been proved as a UOR catalysts, while the latter was added to materials to increase their activity in literature. The best performing material among this group was 20Mo-Ni$(OH)_2$ that reached the highest current densities and had the lowest on-set potential (1.38 V). 30Mo-Ni$(OH)_2$ showed a worse performance than 20Mo-Ni$(OH)_2$ even though the molybdenum content was higher. This could be due to an excessive amount of MoO_3 in the material, which is not very active. In the case of the nickel phosphide-based materials, the only sample that showed a significative increase in activity respect to the un-modified one was 20Mo-NiP. The other two samples showed a similar behaviour to NiP. This could be due to the different quantity of nickel oxide in the samples, as deduced from XRD. The presence of nickel oxide is due to the presence of big particles in the samples and the phosphine could not penetrate inside them in order to react. The low activity of the 30Mo-NiP sample could be explained by the presence of a high amount of nickel oxide inside the particles. Also in literature it was found that an excessive amount of molybdenum could actually decrease the performance of the catalysts. The best catalyst of the group was 20Mo-NiP, which reached the highest currents and had the lowest on-set potential (1.39 V).

Finally, the nickel phosphide-based materials were tested as HER electrocatalysts. The results obtained were far worse than expected since none of the modified samples showed significative increase in activity respect to the pure material. In general, the on-set potentials were more negative than what found in literature. There was not a significative difference between the manganese and molybdenum-modified samples. These negative results could be explained by the non-total phosphurization of the materials and, therefore, to the presence of nickel and molybdenum oxides, which are not active for this reaction.

5.1 Future perspectives

In the case of the manganese-modified nickel hydroxides, it was verified that their activity towards the UOR increased with the increase of manganese content. This leaves space for a future investigation on samples containing a higher manganese content to understand which is the optimal composition. The high content of Mo in the molybdenum-modified nickel hydroxides samples made the structural and chemical characterization complex. It was not possible to verify that the molybdenum entered the structure and different molybdenum phases were present. For these reasons, it would be interesting to test some samples with lower molybdenum content and compare them to the Mn-Ni$(OH)_2$ samples. Similar results were obtained for the phosphides, for this reason the future nickel hydroxide-based materials could be used to obtain phosphides. To improve the phosphides synthesis the reaction time should be increase to let phosphine reach the inside of the larger particles. In the case of the phosphides, it could be useful to characterize them with XAS to understand the oxidation state of the metals in the bulk. Finally RRDE measurements in presence of urea should be done to understand at which potential the oxygen evolution reaction starts.